Technische Universität München
TUM School of Natural Sciences

Metal and Metal Carbide Catalysts for Hydrogen Activation

Patrick Schlachta

Vollständiger Abdruck der TUM School of Natural Sciences der Technischen Universität München zur Erlangung eines

Doktors der Naturwissenschaften (Dr. rer. nat.)

genehmigten Dissertation.

Vorsitz: Prof. Dr. Sebastian Günther

Prüfende der Dissertation:

1. Prof. Dr. Klaus Köhler
2. Prof. Dr. Tom Nilges

Die Dissertation wurde am 15.10.2025 bei der Technischen Universität München eingereicht und durch die TUM School of Natural Sciences am 08.12.2025 angenommen.

Die vorliegende Arbeit entstand im Zeitraum vom Juli 2020 bis Oktober 2025 an der Fakultät für Chemie und am Zentralinstitut für Katalyseforschung (CRC) der Technischen Universität München.

Mein besonderer Dank gilt meinem akademischen Lehrer

Prof. Dr. Klaus Köhler

für die hervorragende Betreuung dieser Arbeit,
seine uneingeschränkte Unterstützung,
sein Vertrauen und die damit verbundenen Freiräume in der
Gestaltung und Bearbeitung der Aufgabenstellung,
sowie sein großes Interesse am Gelingen der Arbeit

Danksagung

Mein besonderer Dank gilt **Prof. Dr. Klaus Köhler**, welcher mich über die gesamte Promotionszeit mit großem Engagement betreut hat. Durch konstruktive Gespräche und stetige Unterstützung motivierte er mich kontinuierlich, neue Ideen zu entwickeln und mich fachlich und persönlich weiterzuentwickeln. Sein respektvoller Umgang und sein kooperativer Führungsstil haben entscheidend zum Gelingen dieser Arbeit beigetragen.

Ich bedanke mich herzlich bei **Dr. Patrick Bretzler** für seine Vorarbeit im Themenfeld Wolframcarbid sowie für seine hilfreiche Unterstützung bei fachlichen Fragen hierzu, insbesondere zu Beginn meiner Promotion.

Weiterhin möchte ich mich bei allen Kolleginnen und Kollegen des Arbeitskreises Prof. Köhler bedanken, die mich während meiner Promotion begleiteten. Diese sind: **Dr. Andrea Abram**, **Dr. Hannah Augenstein**, **Franz Bannert**, **Dr. Tobias Bruhm**, **Dr. Max Hiller**, **Dr. Lingdi Kong**, **Lea Kopietz**, **Dr. Oliver Thomys** und **Jinjin Tie**. Ich bin sehr dankbar für die stets angenehme Arbeitsatmosphäre innerhalb der Gruppe, in der ich mich jederzeit sehr wohl gefühlt habe.

Franz Bannert danke ich darüber hinaus für die hervorragende Kooperation zur Untersuchung von Metallcarbiden als Elektrodenmaterialien. **Dr. Max Hiller** bin ich sehr dankbar für seine große Hilfsbereitschaft bei wissenschaftlichen und insbesondere technischen Fragestellungen. Von seiner ausgeprägten Expertise im Umgang mit Swagelok-Systemen und bei der Modifikation katalytischer Testanlagen sowie von seinen tiefgehenden methodischen Kenntnissen in der instrumentellen Analytik habe ich sehr profitiert.

Außerdem gilt mein Dank **Simon Nickl** für seine engagierte und motivierte Arbeit im Rahmen seiner Masterarbeit, die einen wertvollen Beitrag zur Untersuchung der katalytischen Reduktion von N_2O mit H_2 geleistet hat. Auch meinen Forschungspraktikantinnen und -praktikanten **Rafael Holtmann**, **Julia Holzhammer**, **Sharon Istvánffy** und **Franziska Schönig** danke ich für ihre hilfreiche Unterstützung im Labor.

Ich bedanke mich bei **Tim Kratky** und **Prof. Dr. Sebastian Günther** für die Durchführung der XPS-Messungen sowie für die interessanten und aufschlussreichen fachlichen Diskussionen.

Prof. Dr. Friederike Jentoft und **Dr. Rolf Jentoft** danke ich herzlich für die wertvolle Möglichkeit, zwei Forschungsaufenthalte an der *UMass Amherst* absolvieren zu dürfen. Ich habe beide Aufenthalte sehr genossen und dabei viel gelernt, insbesondere durch die zahlreichen fachlichen Diskussionen und den intensiven Austausch im Rahmen einer mehrjährigen Zusammenarbeit. Auch der gesamten Forschungsgruppe von Prof. Jentoft gilt mein Dank für ihre Unterstützung und Freundlichkeit, durch die ich mich sehr willkommen gefühlt habe. Besonders dankbar bin ich **Dipti Bhave** für ihre tatkräftige Unterstützung, durch welche die Organisation meiner Forschungsaufenthalte erheblich erleichtert wurde.

Für die Durchführung der TEM-Messungen danke ich **Dr. Elena Willinger** und **Prof. Dr. Marc-Georg Willinger**. **Dr. Carsten Troll** und **Katia Rodewald** danke ich für die Genehmigung zur Durchführung von SEM-Messungen.

Ich danke auch allen Mitarbeiterinnen und Mitarbeitern der Zentralanalytik des Katalysezentrums, welche am Gelingen dieser Arbeit durch ihre freundliche Unterstützung bei verschiedenen analytischen Methoden beigetragen haben. Dabei danke ich **Dr. Eliza Gemel** und **Dr. Wilhelm Klein**, die durch ihr Management der Zentralanalytik einen reibungslosen Betrieb gewährleisteten. **Thomas Miller** danke ich für seine hilfreiche Unterstützung bei den XRD-Messungen sowie für die interessanten technischen Diskussionen. **Jürgen Kudermann** danke ich für seine umfangreiche Unterstützung und seine fachliche Expertise im Bereich Chromatographie, insbesondere bei Reparaturen und der Behebung technischer Probleme. **Petra Ankenbauer** und **Bircan Dilki** danke ich für die Durchführung der Elementaranalysen.

Für die Organisation, die gute Zusammenarbeit und die Unterstützung bei den insgesamt fünf von mir betreuten Kurspraktika danke ich **Dr. Oksana Storcheva** und **Richard Wetzel** ausdrücklich.

Zudem möchte ich mich bei **Renate Schuhbauer-Gerl** für die Unterstützung bei sämtlichen organisatorischen und administrativen Angelegenheiten bedanken. **Dr. Markus Drees** danke ich für die Unterstützung bei organisatorischen Angelegenheiten rund um den Promotionsprozess. Ich danke außerdem der **TUM Graduate School** für die finanzielle Förderung eines Forschungsaufenthaltes und für das sehr gute Kursprogramm zur überfachlichen Weiterbildung.

Besonderer Dank gilt meinen Geschwistern und meinen Eltern für ihre kontinuierliche Unterstützung, die mir in allen Phasen meiner Promotion sehr geholfen hat.

Zu guter Letzt geht mein Dank an meine Freundin **Widya** für ihren Rückhalt, für ihre unaufhörliche Unterstützung und für ihre motivierenden Worte.

Abstract

With climate change intensifying, the shift from fossil fuels to a hydrogen economy is becoming ever more important. This profound transition increases the demand for effective and low-cost catalyst materials for hydrogen activation, while also creating opportunities for novel processes such as the abatement of nitrous oxide using hydrogen. This dissertation therefore addresses two primary objectives: (i) the exploration of tungsten carbide catalysts as potential substitutes for platinum in hydrogenation reactions, and (ii) the investigation of the selective catalytic reduction (SCR) of N_2O with hydrogen. Tungsten carbide is viewed as a promising alternative to noble metals due to its electronic properties resembling those of platinum, while being available at only a fraction of the cost. However, the synthesis of tungsten carbide catalysts presents a major challenge, particularly due to the high temperatures required, its mechanistic complexity, and the difficulty of achieving high surface areas. Moreover, the effect of the different tungsten carbide phases (W_2C, WC) on the catalytic activity is not well understood so far, which is complicated by the difficulty in systematically synthesizing pure phases. Therefore, this dissertation investigates a less-studied, alternative tungsten carbide synthesis approach with separated reduction of tungsten oxide and carbon insertion. Phase pure W_2C and WC bulk catalysts were achieved using this method and tested in the catalytic hydrogenation of butyraldehyde as a model substrate. W_2C was found to exhibit higher catalytic performance compared to WC, which corresponds well with previously reported theoretical investigations. Furthermore, the synthesis of supported tungsten carbide catalysts by separated reduction and carburization was investigated. The results show that the catalyst dispersion plays a crucial role in dictating the phase composition of the products, which can be attributed to surface energy contributions influencing the thermodynamic stability of the phases.

Moreover, as the second part of the dissertation, the utilization of hydrogen was investigated for the selective catalytic reduction of the potent greenhouse gas N_2O, as a means to leverage the expanding hydrogen infrastructure associated with the emerging hydrogen economy. For this purpose, noble metal catalysts were tested for the selective catalytic reduction of N_2O by H_2. Conversion of N_2O occurred even at temperatures clearly below room temperature. Quasi *in situ* XPS measurements demonstrated that the catalytically active sites are metallic. Structure-activity relationships were explored for palladium catalysts and revealed, in particular, a strong influence of the catalyst support.

This dissertation advances the development of alternative catalytic materials for hydrogen activation by investigating tungsten carbide as a cost-effective alternative to noble metals. It provides improved insights into the solid-state reactions related to the synthesis of tungsten carbide catalysts and the effect of their structural characteristics on their catalytic behavior. Furthermore, this thesis explores the use of hydrogen for N_2O abatement, demonstrating highly effective conversion even at temperatures clearly below room temperature.

Kurzzusammenfassung

Die technische Transformation von fossilen Brennstoffen hin zu einer nachhaltigeren Wasserstoffwirtschaft ist wegen des fortgeschrittenen Klimawandels ein essenzieller Baustein zum Klimaschutz. Hierzu werden effiziente und kostengünstige Materialien für die katalytische Aktivierung von Wasserstoff benötigt. Die erhöhte Verfügbarkeit und der Ausbau der Wasserstoffinfrastruktur kann auch die Entwicklung bisher ungenutzter technischer Verfahren begünstigen, wie etwa die katalytische Reduktion des starken Treibhausgases N_2O (Lachgas) mit Wasserstoff zu Stickstoff und Wasser. Dementsprechend verfolgt diese Dissertation zwei Hauptziele: (i) die Untersuchung von Wolframcarbid-Katalysatoren als potenzieller Ersatz für Platin in Hydrierreaktionen und (ii) die Untersuchung der selektiven katalytischen Reduktion (SCR) von N_2O mit Wasserstoff.

Wolframcarbid gilt aufgrund seiner elektronischen Eigenschaften, die denen von Platin ähneln, als vielversprechende Alternative zu Edelmetallen, da es nur einen Bruchteil der Materialkosten verursacht. Allerdings ist die Synthese von Wolframcarbid-Katalysatoren mit großen Herausforderungen verbunden, insbesondere aufgrund der erforderlichen hohen Temperaturen und ihrer mechanistischen Komplexität sowie der Schwierigkeit, angemessen hohe Katalysatoroberflächen zu erzielen. Zudem ist der Einfluss der verschiedenen Modifikationen von Wolframcarbid (W_2C, WC) auf die katalytische Aktivität bislang unzureichend verstanden, da die systematische und kontrollierte Herstellung reiner Phasen problematisch ist. Diese Dissertation befasst sich deshalb mit einem bisher wenig untersuchten alternativen Ansatz zur Synthese von Wolframcarbid. Dieser sieht eine Trennung der Reaktionsschritte „Reduktion von Wolframoxid“ und „Kohlenstoffeinlagerung“ vor. Mithilfe dieser Methode wurden phasenreine Katalysatoren, bestehend aus W_2C und WC, erfolgreich synthetisiert. Unter Verwendung von Butyraldehyd als Modellsubstrat wurden diese für die katalytische Hydrierung getestet. Dabei zeigte sich eine höhere katalytische Aktivität von W_2C gegenüber WC, was gut mit vorangegangenen theoretischen Untersuchungen aus der Literatur übereinstimmt. Darüber hinaus wurde der Syntheseansatz auch für geträgerte Wolframcarbid-Katalysatoren angewendet. Es zeigte sich hierbei, dass die Katalysatordispersion einen entscheidenden Einfluss auf die Zusammensetzung der Festkörperphasen der hergestellten Materialien ausübt. Dies ist auf die unterschiedliche Oberflächenenergien der Phasen zurückzuführen, welche deren thermodynamische Stabilität beeinflussen. Durch das verbesserte Verständnis der in der Carbidsynthese ablaufenden Festkörperreaktionen und deren Einfluss auf Struktur und katalytische Eigenschaften trägt diese Dissertation zur Etablierung alternativer, kostengünstiger Katalysatoren für die Wasserstoffaktivierung bei.

Im zweiten Teil der Dissertation wurde die Verwendung von Wasserstoff für die selektive katalytische Reduktion von N_2O untersucht, um die wachsende Wasserstoffinfrastruktur gezielt zu nutzen. Hierzu kamen Edelmetallkatalysatoren zum Einsatz, bei denen ein Umsatz von N_2O bereits bei Temperaturen deutlich unterhalb der Raumtemperatur beobachtet wurde. *Quasi in situ* XPS Messungen belegten, dass die katalytisch aktiven Zentren in metallischer Oxidationsstufe vorlagen. Zudem konnten Struktur-Aktivitätsbeziehungen am Beispiel von Palladiumkatalysatoren ermittelt werden, wobei sich insbesondere ein starker Einfluss des Trägers zeigte. Die in dieser Dissertation gewonnenen Erkenntnisse verdeutlichen das Potenzial von Wasserstoff als Reduktionsmittel für N_2O, insbesondere aufgrund der niedrigen Reaktionstemperaturen.

Table of Contents

List of Abbreviations

a.u.	Arbitrary unit
AE	Aerosil®
BET	Brunauer-Emmett-Teller
bipy	Bipyridine
BJH	Barrett-Joyner-Halenda
Cp	Cyclopentadienyl
DFT	Density functional theory
dmad	Dimethylacetylenedicarboxylate
DOS	Density of states
e.g.	Exempli gratia/ for example
Eq.	Equation
et al.	Et alia
eV	Electronvolt
FID	Flame ionization detector
FT-IR	Fourier-transform infrared
FWHM	Full width at half maximum
g	Gram
GC	Gas chromatography
GHSV	Gas hourly space velocity
hcp	Hexagonal close-packed
HER	Hydrogen evolution reaction
ICSD	Inorganic crystal structure database
K	Kelvin
kg	Kilogram
kJ	Kilojoule
L	Liter
LOHC	Liquid organic hydrogen carrier systems
m/z	Mass to charge ratio
MJ	Megajoule
MS	Mass spectrometry
MTG	Methanol to gasoline
MTO	Methanol to olefins
n.a.	Not available
ND	Nanodiamond
nm	Nanometer

s	Second
SCR	Selective catalytic reduction
SEM	Scanning electron microscopy
TEM	Transmission electron microscopy
TPD	Temperature programmed desorption
TPR	Temperature programmed reduction
vs.	Versus
WHSV	Weight hourly space velocity
wt.-%	Weight percentage
XPS	X-ray photoelectron spectroscopy
XRD	X-ray diffraction

1

Introduction and Objectives

1.1 Catalytic hydrogen activation in the context of the hydrogen economy

Fossil fuels have been the foundation of the modern world, playing a key role in driving global economic growth and the success of modern civilization. However, this dependence comes at the expense of drastic environmental issues. Most notably, climate change is progressing in a manner that could lead to severe consequences for society and ecosystems.[1] In response, a profound transformation towards a more sustainable industry is necessary. The concept of the hydrogen economy is considered a substantial and integral part of this transition.[2] The idea is that hydrogen, produced using renewable energy, can serve as an alternative energy carrier for transportation, power generation, and the chemical industry, enabling these sectors to operate without emitting CO_2.[2],[3],[4]

Catalysis plays an important role in a large variety of processes that are closely linked to the hydrogen economy. This concerns the production of hydrogen, the transport or storage and release of hydrogen, and the utilization of hydrogen. For the green production of hydrogen, water electrolysis needs to be carried out on a large scale, with electrode materials serving as electrocatalysts to lower the overpotential.[5],[6] Technical solutions can be used for the transport and storage of hydrogen, such as hydrogen pipelines or tanks with compressed hydrogen gas, liquid hydrogen, or cryo-compressed hydrogen.[7],[8] However, all these approaches bring their own advantages and disadvantages.[9] Besides safety issues, one of the critical challenges is that hydrogen features a low volumetric energy density at standard conditions (0.01 MJ/L H_2 compared to 0.04 MJ/L for CH_4 and 32 MJ/L for gasoline), despite having a very high energy content per unit mass (120 MJ/kg H_2).[10],[11],[12] As an alternative, hydrogen can also be stored or transported in a chemical way. A promising approach in this regard is the binding of hydrogen to liquid organic hydrogen carrier systems (LOHC).[13] This involves the conversion of a liquid hydrogen-lean compound to a liquid hydrogen-rich compound.[14] The liquid nature of the compounds allows facile transport, as existing gasoline infrastructure could be used.[13] For the release of hydrogen, the hydrogen-rich compound gets dehydrogenated.[15] Both reactions, hydrogenation and dehydrogenation, require suitable catalysts.[16] In particular, the toluene-methylcyclohexane pair is a potential candidate as a LOHC, with three double bonds that can be reversibly hydrogenated.[17]

In the context of H_2 utilization, different catalytic reactions are highly relevant. Hydrogen can be used in fuel cells for the generation of electrical energy, typically over platinum-based catalysts.[18] Moreover, hydrogen can be used in the chemical industry for the production of value-added chemicals. Highly relevant to fertilizer production, ammonia synthesis *via* the Haber-Bosch process involves the catalytic reaction of nitrogen with hydrogen over typically iron-based catalysts.[19] Another important process is the catalytic synthesis of methanol, which serves as

a key platform chemical in the chemical industry that can be used as a precursor to a wide range of further products, including olefins (see MTO) and gasoline (see MTG).[20],[21],[22] Methanol synthesis can offer a sustainable route to chemical production with full carbon recycling when performed using CO_2 captured from exhaust gases or from air and reacted with renewable hydrogen.[20],[23]

Moreover, both ammonia and methanol can also be used in the context of hydrogen storage and transport, as hydrogen can be generated from both compounds.[24],[25] In the case of ammonia, hydrogen can be obtained through catalytic decomposition into N_2 and H_2, and by catalytic reforming into CO_2 and H_2 in the case of methanol.[26],[27]

The Fischer-Tropsch process is another catalytic reaction that can become relevant within the framework of the hydrogen economy, as it allows direct synthesis of long-chain hydrocarbons.[28] Similarly to methanol synthesis, direct air captured CO_2 can in principle be utilized in this process along with renewable hydrogen.[29] The application of Fischer-Tropsch-based processes is especially promising for the production of sustainable aviation fuels.[30]

As another route toward carbon neutrality, biomass upgrading is regarded as a promising strategy for the sustainable production of chemicals. This approach can be of great value for the use of renewable hydrogen, as hydrogenation reactions are very important in this context due to the high oxygen content of biomass-derived compounds.[31] Various types of feedstock and catalytic processes are viable, most notably the hydrogenation of monosaccharides (e.g. glucose), furanic compounds (e.g. furfural), carboxylic acids (e.g. succinic acid), fatty compounds (e.g. vegetable oils), and wood derivatives (e.g. lignin).[32] Besides their activity, the selectivity of catalysts is a crucial factor in these catalytic reactions.[33]

A large variety of other established industrial catalytic hydrogenation processes currently predominantly employ hydrogen derived from fossil fuels. Hence, there is a significant potential for reducing CO_2 emissions. Hydrogenation is considered one of the most important catalytic methods in synthetic organic chemistry, as it offers benefits such as broad applicability, high selectivity, and high conversion under mild liquid-phase conditions.[34] A prominent large-scale hydrogenation process is the hydrogenation of benzene to produce cyclohexane, which can subsequently be used for the production of nylon via ε-caprolactam.[35] Another example is the catalytic hydrogenation of nitrobenzene to produce aniline, an essential precursor widely employed in the production of dyes, pharmaceuticals, and polymers.[36],[37]

In view of the large number of processes involving hydrogenation reactions, the catalytic activation of hydrogen is expected to become substantially more significant with the emergence of the hydrogen economy. However, the activation of hydrogen is in fact challenging due to the high bond energy of 436 kJ/mol.[38] Effective catalysts for this purpose are therefore rather rare. Noble metals such as platinum or palladium exhibit favorable catalytic properties with very low energy barriers for hydrogen dissociation on their surfaces[39],[40], however, they are very expensive and scarce. In view of the enormous scale of renewable

hydrogen production and utilization as envisioned in the hydrogen economy, a strong reliance on noble metals is therefore unsustainable. This increases the urge to develop low-cost, abundant materials as effective alternatives for hydrogen activation. In that sense, tungsten carbide, as a transition metal carbide, might fulfill these criteria. Further insight into the opportunities and challenges of tungsten carbide as a catalyst material can be found in section 1.2.

Profound changes in the technical infrastructure can be assumed due to the transition towards a hydrogen economy, which requires re-thinking of established processes. As one example, the application of hydrogen as a reducing agent of nitrogen oxides (NO, NO_2, N_2O) may become a viable alternative in exhaust gas treatment processes. In order to advance this goal, the development and optimization of efficient catalysts and a profound understanding of the reaction mechanisms are required. Section 1.3 introduces the selective catalytic reduction of N_2O.

1.2 Tungsten carbide as alternative material for catalytic hydrogen activation[1]

As described also in 1.1, the scarcity and high cost of noble metals greatly increase the incentive to find comparable alternatives as catalysts for hydrogen activation. Tungsten carbide is often considered a prime candidate in this sense, as its electronic properties have been found to be similar to those of platinum. This effect was first reported by Levy and Boudart in the 1970s and was explained by a change in the electronic properties upon carbon insertion into the tungsten metal lattice.[41] Interactions between tungsten and carbon, such as electron transfer, play an important role and affect the density of states near the Fermi level.[42],[43],[44] In principle, these characteristics should translate into catalytic properties, and indeed, catalytic behavior similar to that of platinum has been observed for certain reactions and under specific conditions.[41],[45] With the price for tungsten carbide being 1000 times lower, the prospect of a cheap alternative to platinum attracted a lot of attention.[46],[47] Tungsten carbide proved to be active in different types of reactions, such as hydrocarbon isomerization,[48] ammonia decomposition,[49] Fischer-Tropsch synthesis,[50],[51] and conversion of methane to synthesis gas.[52] Moreover, tungsten carbide is particularly effective in hydrodesulfurization, hydrodenitrogenation, and hydrodeoxygenation reactions, reaching activities close to those of noble metals.[47] For this reason, the material has received a lot of attention in the context of biomass upgrading.[53],[54],[55],[56] For instance, Ji *et al.* showed that an extraordinarily high yield of 61 % ethylene glycol starting from cellulose was achieved over nickel-doped W_2C supported on

[1] Disclaimer: This section, 1.2, (as well as Chapter 2 and parts of Chapter 6) is based on a manuscript published in *The Journal of Physical Chemistry C.* See Section 1.5 for more information.

activated carbon.[57] Other typical biomass-derived feedstocks investigated in the literature included lignin,[58] fatty acids,[59] sugars,[60] and furan-based substrates.[61],[62] Tungsten carbide was often paired with nickel as a secondary active metal in these investigations. Besides catalytic activity, the favorable stability of tungsten carbide to N and S impurities compared to noble metals is frequently emphasized.

Another highly promising application field for tungsten carbide is electrocatalysis, which, so far, is also strongly dominated by noble metals as electrode materials. In fact, it was demonstrated that tungsten carbide can even outperform platinum as an electrocatalyst for the hydrogen evolution reaction (HER) in the intermediate temperature range (200 to 400 °C).[63],[64]

A thorough understanding of how the structural properties of tungsten carbide determine its catalytic activity is critical to optimizing the performance of tungsten carbide for catalytic purposes. However, the role of the different tungsten carbide modifications (W_2C, WC) in catalysis is rather unclear so far.[65] Also, the synthesis of tungsten carbides presents a substantial challenge, as high temperatures and low surfaces are typical.

1.3 Hydrogen activation in the context of exhaust gas treatment

With the transition toward a hydrogen economy, improvements in hydrogen infrastructure and availability are expected, opening opportunities for its implementation in new processes. An important application of heterogeneous catalysts is the removal of undesired compounds from exhaust gas.[66] Particularly relevant in this context is the abatement of nitrogen oxides, which are common byproducts in combustion processes.[67] Pollution of the air by NO and NO_2 can cause harmful acute and chronic effects on human health and can lead to environmental issues.[68],[69] Another relevant nitrogen oxide is N_2O (nitrous oxide, also called laughing gas), which is less critical from a health-related standpoint but exhibits high greenhouse gas potential and causes ozone degradation.[70],[71] Catalytic abatement of nitrogen oxides can be performed thermally due to their thermodynamic instability, or by selective catalytic reduction (SCR) processes.[72],[73],[74] For the mitigation of NO and NO_2 emissions, ammonia is a commonly used reducing agent, which is often obtained through urea decomposition locally.[75] However, the use of ammonia is also related to certain issues, such as emissions of unreacted ammonia, also referred to as ammonia slip, and corrosion problems.[76]

Hydrogen may therefore be a potential alternative reducing agent in SCR processes. Using hydrogen also allows a higher energy efficiency and likely cost advantage, as its production requires less steps than that of ammonia or urea. Moreover, hydrogen combustion engines could become increasingly more relevant in the context of the hydrogen economy.[77] These employ hydrogen as a fuel instead of hydrocarbons; however, they also produce NO_x emissions due to the high temperatures involved in the combustion process.[78],[79] The

application of hydrogen for SCR is evident in these cases, making use of the available infrastructure.[80]

While the selective catalytic reduction of NO with hydrogen has been extensively studied in the literature,[81] the corresponding reduction of N_2O has received much less attention and, therefore, is an important research interest. In addition, the reaction of N_2O with H_2 exhibits extraordinarily high exothermicity (ΔH of -323.3 kJ/mol at 298 K), making it a relevant model reaction for the investigation of heat transfer on catalysts.

1.4 Aim and motivation of the thesis

The transition towards a hydrogen-based economy increases the need for effective, low-cost catalyst materials to activate hydrogen and creates opportunities for developing new processes, such as utilizing hydrogen to abate nitrogen oxides.

Two primary aims are therefore addressed in the scope of this thesis:

1) **Exploration of tungsten carbide catalysts as potential substitutes for platinum in hydrogenation reactions**

2) **Investigation of the selective catalytic reduction (SCR) of N_2O (nitrous oxide) by hydrogen**

With electronic properties similar to platinum yet available at only a fraction of the cost, tungsten carbide offers promising potential as a low-cost alternative material for catalytic hydrogen activation. However, the synthesis of tungsten carbide with properties suitable for high catalytic performance is particularly challenging, especially due to typically high temperatures. Besides, the role of the main tungsten carbide modifications for catalytic activity is poorly understood so far, and synthesis methods allowing reliable phase control of the products are rare. Chapters 2 and 3 of this dissertation, therefore, explore a less-investigated two-step synthesis approach for the preparation of tungsten carbide catalysts and their behavior in catalytic hydrogenation reactions. Special emphasis is placed on the investigation of phase-related activity, but also on the influence of the catalyst morphology and surface characteristics. Chapter 2 investigates bulk tungsten carbide catalysts, while Chapter 3 extends the investigation to supported systems.

In Chapter 2, the synthesis of pure bulk tungsten carbide phases (W_2C and WC) via separated reduction and carburization synthesis is intended. The influence of key synthesis parameters on the product characteristics after reduction and carburization is investigated through various characterization methods. The catalytic activities of pure W_2C and WC bulk catalysts are compared in the hydrogenation of butyraldehyde.

In Chapter 3, the synthesis of SiO_2 supported tungsten carbide catalysts via separated reduction and carburization synthesis is investigated. The effect of the dispersion of the tungsten species (WO_3, W, W_xC) on the phase composition of the products is examined by different WO_3 based precursors. The performance of the catalysts in hydrogenation reactions is evaluated with emphasis on further insight of the influence of the tungsten carbide dispersion and phase composition (W_2C, WC) on the catalytic activity.

With the growing availability of hydrogen in the context of the hydrogen economy, the selective catalytic reduction of N_2O by hydrogen could present an effective strategy for the abatement of N_2O emissions. Besides the environmental significance of this reaction, it is highly interesting as a model reaction for fundamental insights into the role of heat dissipation at catalyst surfaces, due to its extraordinarily high exothermicity.

Chapter 4 explores this utilization of hydrogen for the selective catalytic reduction of N_2O. Improved understanding of general and fundamental aspects concerning the catalytic reaction is intended by employing quasi *in situ* X-ray Photoelectron Spectroscopy (XPS) measurements and measurements in a continuous fixed-bed reactor. In particular, establishing structure-activity relationships is intended. In addition, the role of heat dissipation in the highly exothermic H_2-SCR of N_2O is addressed. This chapter specifically focuses on the low temperature range, due to the unique characteristics of this behavior, with catalysis occurring even clearly below room temperature.

With its two main objectives, this thesis aims to contribute both to the advancement of catalytic materials for hydrogen activation and to the exploration of H_2 utilization in the context of N_2O abatement, as well as to improving the understanding of the role of heat transfer in highly exothermic reactions.

1.5 Disclaimer

Disclaimer: Section 1.2 (as well as Chapter 2 and parts of Chapter 6) is based on a manuscript published in *The Journal of Physical Chemistry C*, titled “Synthesis of Phase-Pure W_2C and WC by Separation of Reduction and Carburization and their Differing Performance as Hydrogenation Catalysts” with the following citation: [82]

Patrick Schlachta, Rolf E. Jentoft, Friederike C. Jentoft, Klaus Köhler, *The Journal of Physical Chemistry C*, **2025**, *129***,** 47, 20907-20921.
DOI: 10.1021/acs.jpcc.5c05153

The author of this dissertation (Patrick Schlachta) is also the first author of the manuscript. The contributions of Patrick Schlachta to the manuscript in the sense of the CRediT author statement definitions include conceptualization, investigation, methodology, validation, formal analysis, visualization and writing (original draft and editing). The content has been edited and restructured to some extent, to align with the format and context of this dissertation. All co-authors, that is Rolf E. Jentoft, Friederike C. Jentoft and Klaus Köhler have approved the use of the manuscript in this dissertation. The article is intended to be published as open access and is reused here for the purpose of this dissertation in accordance with the Creative Commons Attribution 4.0 International License (CC BY, see https://creativecommons.org/licenses/by/4.0/), which allows unrestricted reuse of the work in any medium or format, as long as the original work is properly credited.

2

Bulk tungsten carbide as hydrogenation catalysts

2.1 Introduction[2]

2.1.1 Tungsten carbide and its polymorphs

Like most other transition metals, tungsten can incorporate carbon into its lattice.[83] This results in the formation of tungsten carbide, which can be considered an interstitial solution.[84],[85],[86] Despite sharing certain characteristics, the physical and chemical properties of tungsten carbide are distinct from tungsten metal. Features such as its high melting point, exceptional hardness, and tensile strength, tungsten carbide are typical for a ceramic material.[87] However, unlike typical oxidic ceramics, it exhibits pronounced metallic characteristics in terms of its electrical conductivity, magnetic susceptibility, Hall coefficient, and heat capacity.[87] These properties are common among all refractory metal carbides and make this unique class of materials highly attractive for a wide range of applications.[88] Tungsten carbide, in particular, is frequently implemented in wear-resistant components and cutting and drilling tools.[89],[90] In this context, tungsten carbide is usually combined with binder metals such as cobalt in order to form a composite material after sintering, which is referred to as cemented carbide.[91] Sintering and densification of tungsten carbide powder are complicated due to its high melting point; therefore, a binder material is typically required during processing.[92],[93] This principle enabled the production of the first industrial hardmetal grade cemented carbide in the 1920s, marketed under the name “Widia”, a name formed from the German words “wie” and “Diamant”, meaning “like diamond”.[94]

Tungsten carbide can exist primarily in two different stoichiometries, tungsten monocarbide WC and tungsten semicarbide W_2C.[95] Hexagonal WC, also referred to as δ-WC, is the thermodynamically most stable phase below 1250 °C when neglecting surface energy contributions.[96] Its crystal structure (hP2, $P\bar{6}m2$) consists of a simple, not close-packed hexagonal lattice of W-atoms with carbon atoms filling the octahedral vacancies. W_2C can exist in a variety of polymorphs, which are referred to as α,β,γ and ε-W_2C or β, β’, β’’ and ε.[97],[98] All of these share the same hcp-lattice of W-atoms with different locations of carbon atoms and are therefore practically indiscriminate by X-ray diffraction.[99] Besides W_2C and hexagonal WC, there exists a WC_{1-x} phase, also known as β-WC, which is stable at very high temperatures (above 2516 °C).[96] It can be considered a cubic polymorph of WC with a NaCl structure (Fm $\bar{3}$m).[100] However, due to several drawbacks such as its rather difficult synthesis and low stability at lower temperatures, this phase received very little attention for catalytic applications.[101]

[2] Disclaimer: This chapter (Chapter 2) is based on a manuscript published in *The Journal of Physical Chemistry C*. See Section 2.7 for more information.

2.1.2 Tungsten carbide synthesis - General

The first synthesis of tungsten carbide dates back to the 1890s and was achieved by Henri Moissan using a self-built electric arc furnace.[102] This discovery was presumably driven by the goal of developing less costly hard material alternatives to diamond dies for the manufacturing of tungsten wires used in electric lighting.[94] The general synthesis concept is still the foundation for the standard production process for tungsten carbide used in metallurgical applications today, which involves a solid-solid reaction of tungsten metal powder and carbon at 1400 °C to 1800 °C.[103] This process is also referred to as *direct carburization of tungsten powder*.[104] Tungsten powder is mixed with carbon black in a stoichiometric ratio and heated for a certain time, resulting in a solid state reaction of both (Scheme 1). The exact process conditions depend in particular on the tungsten and carbon precursors. The reactivity of tungsten powder decreases with larger particle sizes, which requires the use of higher temperatures, up to 2100 °C.[105] Similarly, higher surface areas of the carbon powder improve the contact with the tungsten particles and therefore increase the reactivity.[105] The synthesis is typically carried out under a hydrogen atmosphere, which promotes the generation of volatile hydrocarbons. In this case, gas-solid reactions play a role besides pure solid-solid reactions, allowing a more homogeneous carbon coverage of the tungsten surface and therefore providing a higher carbon supply. The carburization of metallic tungsten follows in principle a two-step sequence, with the formation of W_2C as an intermediate before further reaction to WC (Scheme 2).[106] However, a mixture of both phases is commonly obtained by this synthesis. The phase composition can be influenced by various synthesis conditions such as the atmosphere, carbon content, and type of furnace.[104] The formation of tungsten carbide proceeds through the diffusion of carbon atoms into the tungsten lattice. Kinetic investigations observed a rather fast initial formation of W_2C and significantly slower further transformation of W_2C into WC.[107]

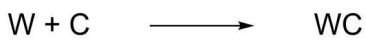

Scheme 1: Reaction equation for the direct carburization of metallic tungsten.

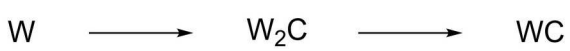

Scheme 2: Reaction sequence for the direct carburization of metallic tungsten.

2.1.3 Synthesis of tungsten carbide with high surface areas

Gas-solid synthesis

Despite its great significance for the production of tungsten carbide for metallurgical purposes, the direct carburization of metallic tungsten is associated with severe drawbacks. The process demands very high temperatures and results in products with low surface areas and often a large amount of excess carbon covering the surface, making this synthesis route particularly undesirable for catalytic applications.[108] These weaknesses, among others, led to the exploration of alternative synthesis routes. As such, gas-solid synthesis emerged as an effective tool for the preparation of tungsten carbide materials with properties suitable for catalysis.[109] This synthesis approach is characterized by a temperature-programmed process, in which a solid tungsten precursor is heated in the presence of a gaseous carbon source.[110] Following Newkirk *et al*., Boudart *et al.* pioneered in the development of this method.[111],[112] This was an important milestone in the synthesis of tungsten carbide catalysts and also other transition metal carbide catalysts, in particular molybdenum carbide.[113],[114] Different variations of the synthesis conditions are possible, especially concerning the type of tungsten precursor, the carbon source, and the temperature. Typically, WO_3 is used as a tungsten precursor; however, other materials implemented were for instance $WO_{2.72}$,[115] WO_2,[116] tungstic acid,[117] and tungsten salts like ammonium paratungstate.[118] Methane is usually applied as a carbon source, but other gases can also be used, such as CO,[115],C_2H_4, or C_2H_6.[119],[120] In combination with the carbon-containing gas, hydrogen is commonly included in the carburization gas atmosphere in order to avoid excessive formation of carbon deposits on the tungsten carbide surface. During tungsten carbide formation using methane, CH_4 adsorbs onto the metallic W surface and dissociates into adsorbed carbon or CH_x species and hydrogen.[121] This can, however, lead to a build-up of carbon on the surface if the migration of carbon into the latter is significantly slower than the decomposition of CH_4.[110] Hydrogen mitigates this by reacting with adsorbed carbon species, but an excessive hydrogen content can lead to insufficient carbon availability for complete tungsten carbide formation.[122]

The mechanism leading to tungsten carbide by gas-solid synthesis starting from WO_3 is highly complex, as different reaction steps take place simultaneously.[110],[119] Also, a large variety of parameters can have an effect on the synthesis, such as the temperature, the pressure, and the carburization gas composition. The reaction proceeds in several reduction and carbon insertion steps, typical via the intermediate species $W_{20}O_{58}$ and WO_2.[119] The initially formed carbide species is W_2C, which can further react to WC depending on the synthesis conditions.[119] Tungsten metal was also reported as an intermediate species.[110]

Using alternative gases to methane was shown to lower the synthesis temperature due to their higher reactivity. Decker *et al.* reported that the temperatures required for reduction and

carburization of tungsten oxide were 150 K lower when using C_2H_6 or C_2H_4 instead of CH_4.[123] Featuring weaker C-H bonds, these compounds are more easily decomposed and they participate significantly more in the reduction of WO_3 compared to CH_4. Specific surface areas close to 25 m^2/g were achieved using ethane as the carbon source compared to only 10 m^2/g using methane.[123] However, the higher reactivity of ethane and ethene also led to more pronounced deposits of excess carbon on the tungsten carbide surface compared to using methane. The hydrocarbon/hydrogen ratio played an important role in the mechanism.

Tungsten carbide gas-solid synthesis can also be performed with W_2N as an intermediate material. In a very similar way to the synthesis of tungsten carbide, the synthesis of tungsten nitride is typically performed using gas-solid synthesis by temperature programmed reaction of WO_3 with NH_3 (Scheme 3).[124],[125]

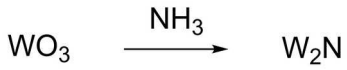

Scheme 3: Transformation of WO_3 to W_2N.

Tungsten nitride can then be used for further conversion to tungsten carbide. Volpe and Boudart applied this principle for the preparation of the metastable fcc phase WC_{1-x} (see section 2.1.1).[126] Interestingly, the solid-state transformation of W_2N to WC_{1-x} was observed to proceed via a topotactic reaction, characterized by complete preservation of the tungsten lattice. The process involves a simple exchange of nitrogen atoms by carbon atoms (Scheme 4) with the tungsten atoms remaining practically immobile throughout the reaction, as no change of the crystallite sizes were found.[126]

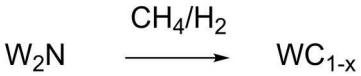

Scheme 4: Transformation of W_2N to WC_{1-x}.

Thanks to structural retention of the parent W_2N material, this synthesis also proved effective for achieving high specific surface areas (up to 55 m^2/g) when high-surface-area tungsten nitride was used as a precursor.[126] Therefore, the synthesis of high surface area tungsten nitride attracted particular interest with the goal of further conversion to tungsten carbide.[127] However, it has to be noted that despite promising results, the synthesis of tungsten carbide from tungsten nitride also comes with certain limitations. Complete structural retention during transformation to tungsten carbide is often not achieved, and the pores of mesoporous tungsten carbide tend to be easily blocked by excess carbon, significantly reducing the theoretically available surface area.[125]

Thermal decomposition of tungsten-containing precursors

As a notably less investigated alternative to gas-solid synthesis, tungsten carbide can also be obtained through the thermal decomposition of tungsten-containing precursors. This type of synthesis can be performed in the gas phase when using volatile tungsten compounds or in the solid state.[128] Typically, tungsten complexes with organic ligands are used, which are heated in an inert atmosphere. Wanner *et al*. decomposed $W(bipy)Cl_4$ together with an excess of bipyridine at 700 °C under argon flow, followed by an activation treatment at 700 °C or 800 °C in order to remove free carbon.[129] Mixtures of W_2C and WC were obtained with specific surface areas up to 250 m^2/g, however, these large surface areas were associated rather with excess carbon, essentially acting as a support.[129] This appears to be a general issue with this synthesis method, as Giraudon *et al*. also reported the presence of excess carbon after decomposition of $Cp_2W_2(CO)_4(dmad)$ under hydrogen flow.[130]

Electrochemical synthesis

Another less common approach for the preparation of tungsten carbide with rather high specific surface areas can be its electrochemical synthesis. Different conditions are possible, but in general, an electrolytic bath is used, consisting of a tungstate salt like Na_2WO_4, metaphosphate, and a halide salt mixture like NaCl-KCl.[131],[132] CO_2 is applied as a carbon source, which requires the use of elevated pressure to improve its solubility in the molten salt.[131] The involved reaction mechanism leading to the formation of tungsten carbide is rather complex, but the overall reaction can, in principle, be expressed by the following reaction equation (Scheme 5):

$$2\,[WO_4]^{2-} + [PO_3]^{-} + 3\,CO_2 + 10\,e^{-} \longrightarrow WC + [WO_4]^{2-} + [PO_4]^{3-} + 2\,CO_3^{2-} + 3\,O^{2-}$$

Scheme 5: Overall reaction equation for the electrochemical tungsten carbide synthesis using CO_2 as a carbon source.[131]

Novoselova *et al*. obtained WC and W_2C-WC mixtures via electrochemical synthesis at 700-750 °C with surface areas in the range of 10 m^2/g to 25 m^2/g.[131] However, the materials were covered by a carbon film, which was assumed to be produced during dismounting of the setup through CO disproportionation upon temperature decrease.[131] In another study, Novoselova *et al*. prepared tungsten carbide materials with up to 140 m^2/g.[133] Variations of the synthesis conditions, such as the pressure, current density, and the electrolytic bath composition, were found to have strong effects on the phase composition and morphology of the products.[133] Nonetheless, a significant amount of free carbon was again present in all materials.[133]

Tungsten carbide synthesis from tungsten hexachloride

Tungsten carbide with a relatively high surface area can also be synthesized by reaction of tungsten hexachloride with a reducing agent. Ma and Du exploited the reaction of tungsten hexachloride with metallic magnesium and sodium carbonate in an autoclave at 600 °C for the synthesis of WC with a BET surface area of around 15 m^2/g.[134] This approach is, according to the authors, based on the high exothermicity of the reduction of WCl_6 by magnesium (-1363 kJ/mol) to tungsten metal, leading to a strong increase in the local temperature (estimation of 1000 °C). [134] Ma and Du proposed that sodium carbonate serves as a carbon source through its decomposition into sodium oxide and carbon dioxide, which further reacts with magnesium to form nascent carbon.[134] The formation of tungsten carbide was assumed to proceed via the reaction of metallic tungsten with carbon.[134]

André *et al.* prepared tungsten carbide nanoparticles with particle sizes below 50 nm using a solid-state metathesis reaction between WCl_6 and potassium dispersed in carbon (KC_4 or KC_8). [135] The reaction can be initiated at low temperatures (below 75 °C) and subsequently proceeds through a self-propagating combustion process.[135] Similar to the reaction of WCl_6 with magnesium, the reaction of WCl_6 with KC_4 or KC_8 is extremely exothermic, resulting in high combustion temperatures of possibly more than 1000 °C.[135] It was proposed that the mechanism involves first the formation of metallic tungsten nanoparticles, which are then carburized to tungsten carbide in a solid-state reaction with carbon (Scheme 6). However, the phase purity of the products were rather low with some extent of metallic tungsten, as well as a large amount of excess carbon present.[135]

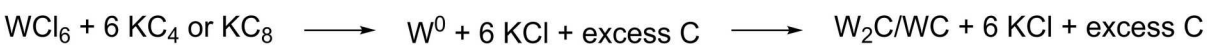

Scheme 6: Reaction sequence for the synthesis of tungsten carbide nanoparticles by a solid-state metathesis reaction between WCl_6 and potassium dispersed in carbon according to André *et al.*[135]

2.1.4 Motivation and aim

A thorough understanding of how the structural properties of tungsten carbide determine its catalytic activity is critical to optimizing the performance of tungsten carbide for catalytic purposes. In this context, the relationship between the tungsten carbide phases W_2C and WC and their inherent catalytic behavior is highly relevant yet remains rather unclear. Resolving this question is complicated by the fact that the practiced synthesis methods often produce a mixture of WC and W_2C. The synthesis methods reported in the catalysis literature are optimized to generate carbides with high surface area. A common method is the temperature-programmed reaction.[110],[119],[120] Briefly, a precursor, usually WO_3, is heated in an atmosphere of H_2 and a carbon source (see 2.1.3 for more details). In such a synthesis, which starts with a carbon-free tungsten precursor, W_2C can be regarded as an intermediate in the formation of WC. Control over the tungsten carbide phase during synthesis has scarcely been investigated. Optimization of synthesis parameters, however, is a possible approach in this regard, as demonstrated by Delannoy *et al.* and also Sullivan and Bhan, who succeeded in the synthesis of phase-pure bulk W_2C and WC catalysts through the use of different synthesis temperatures, with 800 °C for WC and 630 °C for W_2C.[136],[137] Another viable approach for the targeted synthesis of W_2C is the limitation of carbon availability. This can be achieved by supporting a tungsten precursor on solid carbon sources such as activated carbon,[138],[139] carbon spheres[140], melamine[141],[142], carbon nanotubes,[143],[144] or carbon nanofibers.[145],[146],[147] The generally rather low reactivity of the solid carbon supports limits the migration of carbon atoms from the support to tungsten.[143]

Another strategy to favor the preparation of W_2C was found to be the use of non-reducible metal oxide supports. In various investigations, carburization of WO_3 supported on silica resulted selectively in W_2C as product species.[148],[149],[150] Moreover, Juneau *et al*. showed that encapsulating tungsten in silica can be an effective way to preserve the particle size of tungsten carbide.[151] By the removal of silica templates after carburization, mesoporous bulk W_2C could be achieved by Lu *et al*.[152]

Bretzler *et al.* systematically analyzed the influence of synthesis parameters on the structural properties of tungsten carbide supported on silica and unsupported tungsten carbide.[65] These relationships were further extended by linking them to the catalytic performance by testing the synthesized catalysts in hydrogenation reactions. It was found that performing carburization under isothermal conditions significantly improves control over the phase composition of the products. Additionally, as observed in other studies, using silica as a support for the tungsten precursor proved beneficial for achieving W_2C as the predominant product phase.

The typically employed gas-solid synthesis of tungsten carbide involves reduction and carburization performed together in one step. This results in a high degree of complexity, as the reduction of tungsten oxide and carbon insertion can proceed simultaneously. In this

dissertation, it is intended to provide greater clarity on the processes involved in gas-solid tungsten carbide synthesis by employing a different approach. In this method, the synthesis is performed in a sequential way, with reduction and carburization as separate steps. Tungsten oxide is first reduced to its metallic form, and only after that, carburization is carried out. This alternative method of gas-solid synthesis of tungsten carbide has been studied to a very limited extent. Gao and Kear investigated this alternative synthesis route and reported that the reduction temperature of tungsten oxide has a decisive effect on the product characteristics.[153] Reduction below 600 °C yielded the metastable beta tungsten modification, whereas reduction at higher temperatures resulted in the stable alpha tungsten modification. The higher reactivity of beta tungsten allows carbide synthesis at much lower temperatures than by carburization of alpha tungsten. This effect makes this synthesis approach also highly interesting, considering catalytic applications. However, rather few studies have been carried out to implement stepwise gas-solid synthesis of tungsten carbide catalysts, specifically as electro-catalysts.[154],[155] The focus of the present investigation is the synthesis of the bulk pure phases, understanding and optimizing the synthesis conditions, and assigning the intrinsic catalytic performance of W_2C and WC for a hydrogenation reaction.

Time-resolved analyses of the solid-state reactions concerning reduction and carburization shall be achieved by *in situ* X-ray diffraction (XRD). The influence of key synthesis parameters on the product characteristics after reduction and carburization is investigated by XRD, Scanning electron microscopy (SEM), N_2 physisorption (BET), and also CO chemisorption in the case of the carbide catalysts. The performance of the catalysts is evaluated in the hydrogenation of butyraldehyde to 1-butanol.

2.2 Reduction of tungsten oxide to tungsten metal

The investigated alternative approach for tungsten carbide synthesis involves two distinct steps. First, tungsten oxide is reduced to its metallic form, which is then carburized to form tungsten carbide. The reduction of a WO_3 bulk precursor was studied at 550 °C, 700 °C, and 800 °C (Scheme 7).

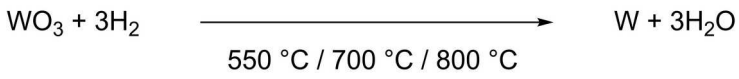

Scheme 7: General reaction equation of WO_3 reduction.

Pure WO_3 was used as the precursor for the synthesis of tungsten carbide. This material was characterized by large, cubic particles with a rather smooth surface and without visible cracks or holes, as can be seen by scanning electron microscopy (SEM) images (Figure 1). This observation is in accordance with the low specific surface area determined by BET, which was measured to be about 9 m^2/g (Table 1). The reflections in the X-ray powder diffractogram of the precursor (Figure 2) can be assigned to those of monoclinic WO_3, which is the thermodynamically stable modification at room temperature.[156] As determined from the XRD patterns using the Scherrer equation, the crystalline domain size of the WO_3 was about 37 nm (Table 1). A second WO_3 powder with even lower surface area (1 m^2/g) was reduced in the tube furnace to demonstrate the effect of low precursor oxide surface area.

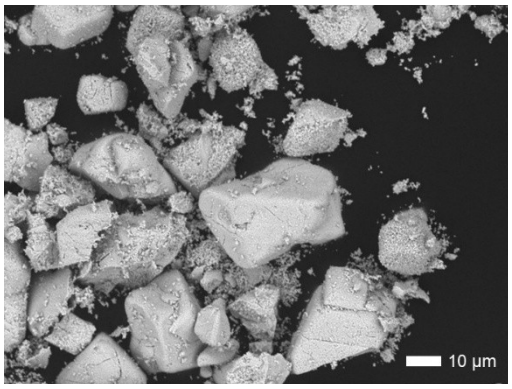

Figure 1: SEM image of the WO_3 precursor (9m^2/g)(1000x magnification).

Table 1: Overview of the tungsten oxide based precursor characteristics.

Precursor	BET specific surface area [m^2/g]	BJH pore volume [mL/g]	Crystallite size [nm][a]
WO_3 bulk	9	0.030	37.0± 0.8

[a] as determined from the FWHM of selected XRD reflexes (23.6 °; 24.2°) using the Scherrer equation

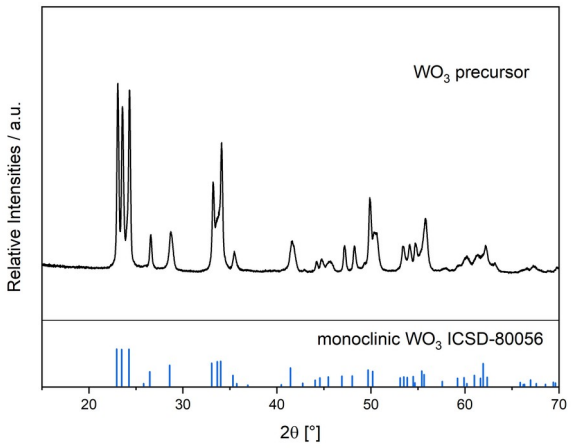

Figure 2: XRD pattern of the WO_3 precursor (9 m^2/g).

2.2.1 Phase evolution during reduction of WO_3

The isothermal reduction of WO_3 at 550 °C and 700 °C was investigated by *in situ* XRD. The evolution of the XRD pattern of the sample during reduction at 550 °C is shown in Figure 3. During heating up to 550 °C under inert gas, the crystallinity of the WO_3 precursor increased as indicated by sharper reflections. In addition, the monoclinic crystal structure is expected to be transformed into an orthorhombic one according to the literature.[157] This transition is difficult to confirm as both phases possess very similar XRD patterns. After the temperature of the sample holder stabilized at 550 °C, the reduction was initiated by introducing hydrogen. The first transformation taking place was the formation of a tungsten bronze $H_{0.23}WO_3$, which was also observed in *in situ* XRD investigations by Keilholz *et al.*[158] After 20 min under H_2 flow, the tungsten bronze phase was completely converted to $W_{20}O_{58}$, which also partially reacted further to β-W. This reaction continued and was complete at 50 min under H_2 flow.

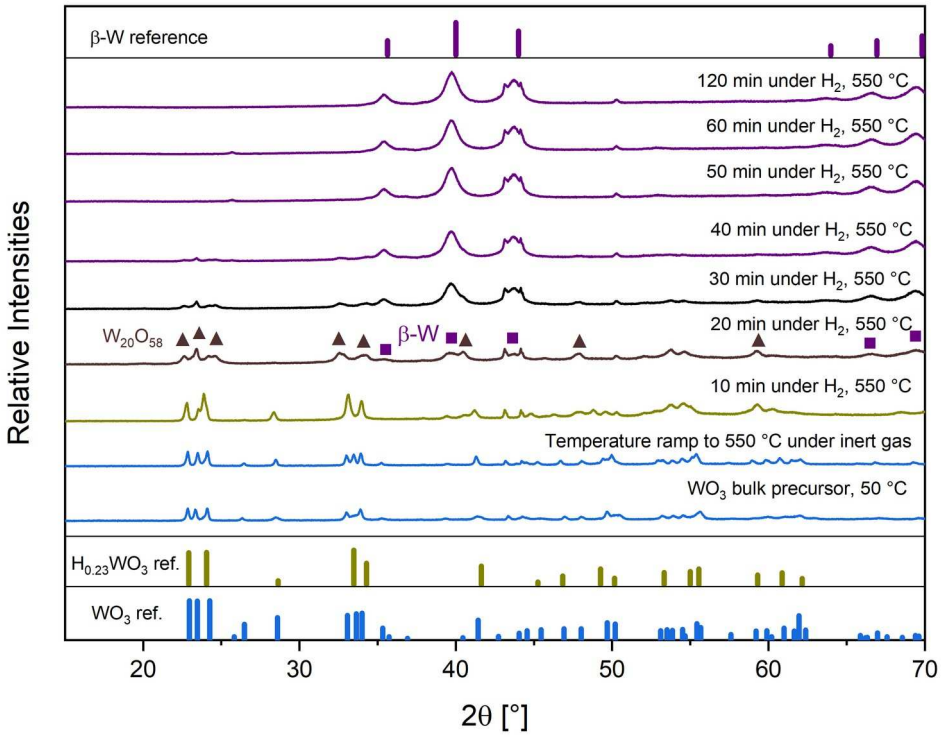

Figure 3: Evolution of the XRD patterns recorded in situ during isothermal reduction of WO_3 at 550 °C by molecular hydrogen (45 mg WO_3, 100 mL/min H_2 flow after heat up under inert gas). The minor reflexes at 43.1°, 44.2° and 50.4° stem from the sample holder of the in situ XRD cell. The reference patterns were sourced from the following database entries: WO_3: ICSD-80056. $H_{0.23}WO_3$: ICSD-8217. $W_{20}O_{58}$: ICSD-27705. Beta tungsten: ICSD-150496. Additional selected markers were added to aid visual assignment.

Evolution of the XRD pattern of the sample during reduction at 700 °C is shown in Figure 4. Interestingly, during heating to 700 °C under an inert gas flow, most of the WO_3 phase was already transformed into $W_{20}O_{58}$. This result shows that oxygen loss and partial reduction of WO_3 can take place at elevated temperatures even in the absence of a reducing agent. Upon switching to H_2, the $W_{20}O_{58}$ phase reacted further to WO_2 and to α-W. However, the content of WO_2 was very low, likely due to rapid further conversion. Indeed, the reduction to metallic tungsten was largely complete after only 10 min under H_2 flow.

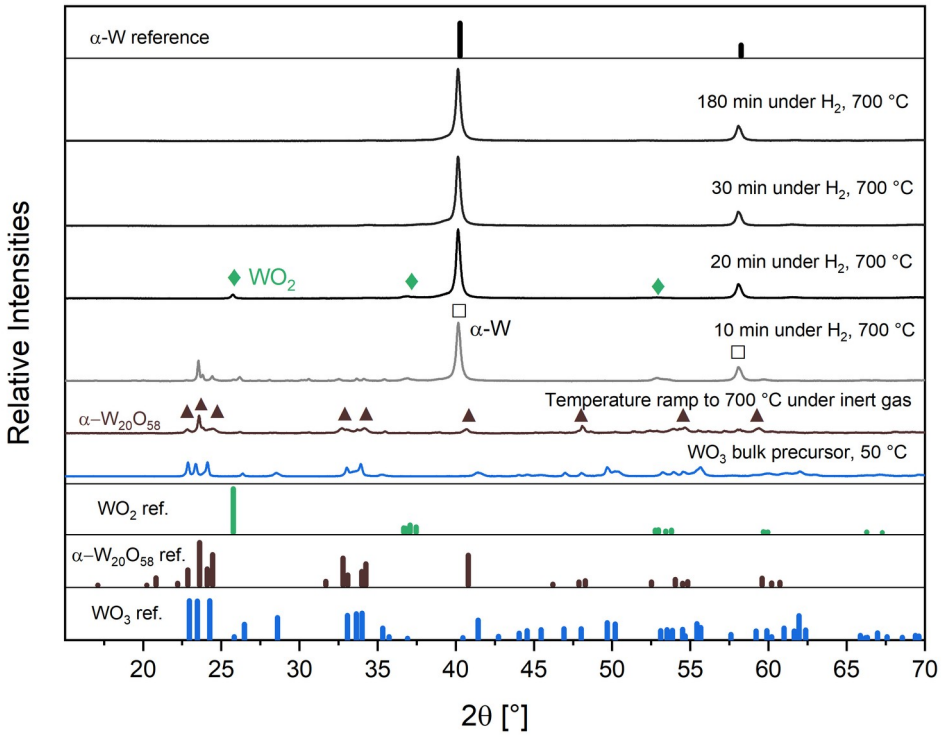

Figure 4: Evolution of the XRD patterns in the course of in situ isothermal hydrogen reduction of WO_3 bulk at 700 °C (45 mg WO_3, 100 mL/min H_2 flow after heating up under inert gas). The reference patterns were sourced from the following database entries: WO_3: ICSD-80056. $W_{20}O_{58}$: ICSD-27705. WO_2: ICSD-80829. Alpha tungsten: ICSD-44393. Additional selected markers were added to aid visual assignment.

To summarize the observations of the *in situ* XRD investigations, the reduction to metallic tungsten proceeds in several reduction steps through intermediate tungsten oxide species. The reduction pathways to alpha tungsten and beta tungsten are different from each other. No intermediate WO_2 was detected in the reduction path to beta tungsten (Scheme 8):

$$WO_3 \longrightarrow H_{0.23}WO_3 \longrightarrow W_{20}O_{58} \longrightarrow \beta\text{-W}$$

Scheme 8: Reaction sequence from WO_3 reduction to beta-W

Reduction to alpha tungsten proceeds with formation of the intermediate WO_2 (Scheme 9):

$$WO_3 \longrightarrow W_{20}O_{58} \longrightarrow WO_2 \longrightarrow \alpha\text{-W}$$

Scheme 9: Reaction sequence from WO_3 reduction to alpha-W.

These differences in the reaction pathways are similar to the observations of Wilken *et al.*, who also reported the presence of WO_2 in the reduction of WO_3 to alpha tungsten and its absence in the reduction of WO_3 to beta tungsten.[159]

Reduction of slightly larger amounts of oxide in a tubular furnace resulted in the same phases as detected at the end of the reduction process in the *in situ* XRD experiments. Reduction at

550 °C resulted in beta tungsten as the only product phase, while reduction at 700 °C and 800 °C led to pure alpha tungsten (Figure 5). The observations are also in line with those by Gao and Kear, who reported the formation of beta tungsten when reducing pure WO_3 powder at 550 °C and the formation of alpha tungsten at 700 °C or higher.[153] Notably, when starting with a tungsten oxide of lower surface area (1 m^2/g vs. 9 m^2/g for the oxide used in all other experiments), the reduction at 550 °C resulted in a metal powder that was mostly alpha tungsten (Figure 5). This finding indicates that the resulting phase composition is influenced by the oxide specific surface area, and that higher specific surface area favors production of the metastable beta tungsten phase.

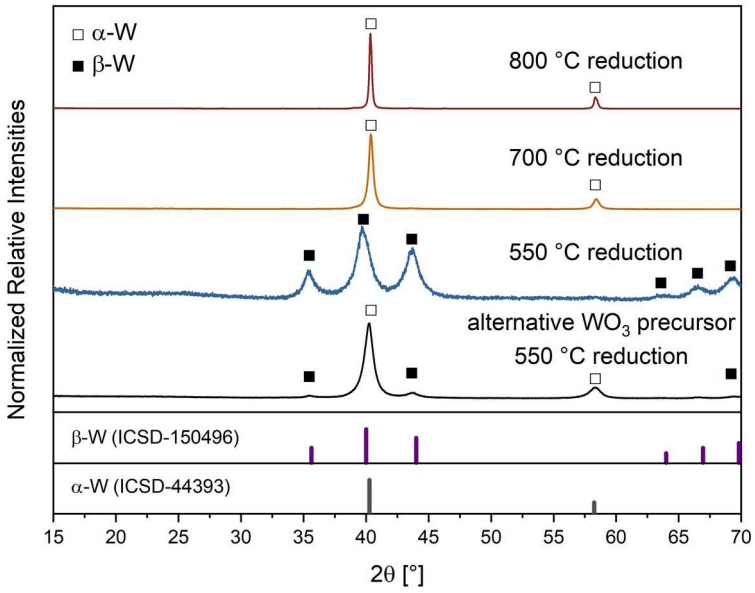

Figure 5: XRD patterns of the products from isothermal hydrogen reduction of WO_3 bulk at different temperatures in a horizontal high-temperature furnace with stick-patterns and markers for alpha tungsten (reference pattern: ICSD-44393) and beta tungsten (reference pattern: ICSD-150496). In addition, the reduction product at 550 °C of an alternative WO_3 precursor with lower surface area (1 m^2/g) is included.

2.2.2 Properties of reduction products and their dependence on the synthesis parameters

The crystallite sizes observed after reduction in the synthesis furnace were strongly dependent on the reduction temperature (Table 2, Figure 6). For both precursors, there is a clear increase in crystallite sizes for the product metallic tungsten with increased reduction temperature. The change of crystallite size during reduction of WO_3 could be enhanced by chemical vapor transport of volatile $WO_2(OH)_2$ that can be formed by reaction of WO_3 or WO_2 with water (Scheme 10):[160],[161]

$$WO_3 + H_2O \rightleftharpoons WO_2(OH)_2$$
$$WO_2 + 2\,H_2O \rightleftharpoons WO_2(OH)_2 + H_2$$

Scheme 10: Reaction equations of the formation of volatile $WO_2(OH)_2$.

$WO_2(OH)_2$ can be transported in the gas phase and deposited as tungsten (Scheme 11).

$$WO_2(OH)_2 + 3H_2 \rightleftharpoons W + 4H_2O$$

Scheme 11: Reaction equation of the decomposition of $WO_2(OH)_2$.

This reaction can lead to agglomeration of tungsten and crystallite growth.[162] Further, sintering can contribute to particle growth. It is likely that most of the changes in crystallite size occur during the reduction and during heating to the reduction temperature. With a melting point of 1472 °C, WO_3 is expected to be susceptible to sintering above its Tammann temperature of 600 °C.[163] In contrast, once metallic tungsten has been formed, sintering is assumed to be less relevant, because of tungsten's very high melting point of 3422 °C and correspondingly high Tammann temperature of 1141 °C. The *in situ* XRD investigations confirm this hypothesis. No increase in crystallite size was observed after complete reduction to tungsten metal, regardless of the product phase or temperature.

Table 2: Overview of the phase compositions and crystallite sizes depending on the reduction temperature.

Reduction temperature	**Phase composition**	**Crystallite size[a] [nm]**	**BET surface area [m^2/g]**	**BJH Pore volume [mL/g]**
550 °C	100wt.-% β-W	7.5 ± 1	19	0.049
700 °C	100wt.-% α-W	20.1± 2	13	0.047
800 °C	100wt.-% α-W	38.7± 3	4	0.017

[a] as determined from the FWHM of the XRD reflections using the Scherrer equation. The reflections at 40.3 ° and 58.3 ° were used for α-W and the reflections at 35.4 °, 39.7 ° and 43.6 ° were used for β-W.

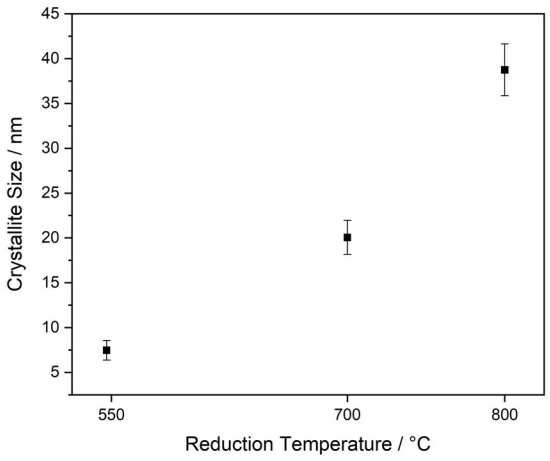

Figure 6: Influence of the reduction temperature on the tungsten metal crystallite sizes as determined from the XRD data using the Scherrer equation.

The influence of the reduction temperature can also clearly be seen by SEM images of the WO_3 precursor after reduction at varying temperatures (Figure 7). After reduction at 550 °C, the general particle shape remained largely unchanged from that of the parent WO_3. However, each particle displayed numerous star-shaped cracks that were evenly distributed across the particle. Large cracks were also visible, but the dominant type of cracking here is a star-shaped cracking pattern, which is typical for the low-temperature reduction of WO_3. According to Wilken *et al*., these cracks are caused by local contraction of the tungsten oxide due to reduction to a lower oxide.[159] In fact, the densities of the compounds involved in the sequence of Scheme 9 are as follows: WO_3 7.25 g/cm^3, $W_{20}O_{58}$ 6.67 g/cm^3, beta tungsten 18.83 g/cm^3, suggesting an expansion of the specific volume followed by contraction.

The products of reduction of WO_3 at 700 and 800 °C also feature star-shaped cracks; however, these are much fewer and larger in size. Also, the parent particle structure was much less intact than in the case of reduction at 550 °C. There appears to be a disintegration to form smaller grains from the parent.

As reported in Table 2, reduction at 550 °C resulted in a product with about 19 m^2/g, which is very high for a bulk metal with very high density, and it is considerably higher than the surface area of the parent WO_3 precursor (9 m^2/g). The specific surface area of the tungsten product after reduction of WO_3 at 800 °C was low with only 4 m^2/g. Similarly, significantly higher pore volumes of 0.049 mL/g and 0.047 mL/g were observed after reduction at 550 °C and 700 °C, respectively, compared to 0.030 mL/g for the WO_3 precursor. In contrast, reduction at 800 °C resulted in only 0.017 mL/g.

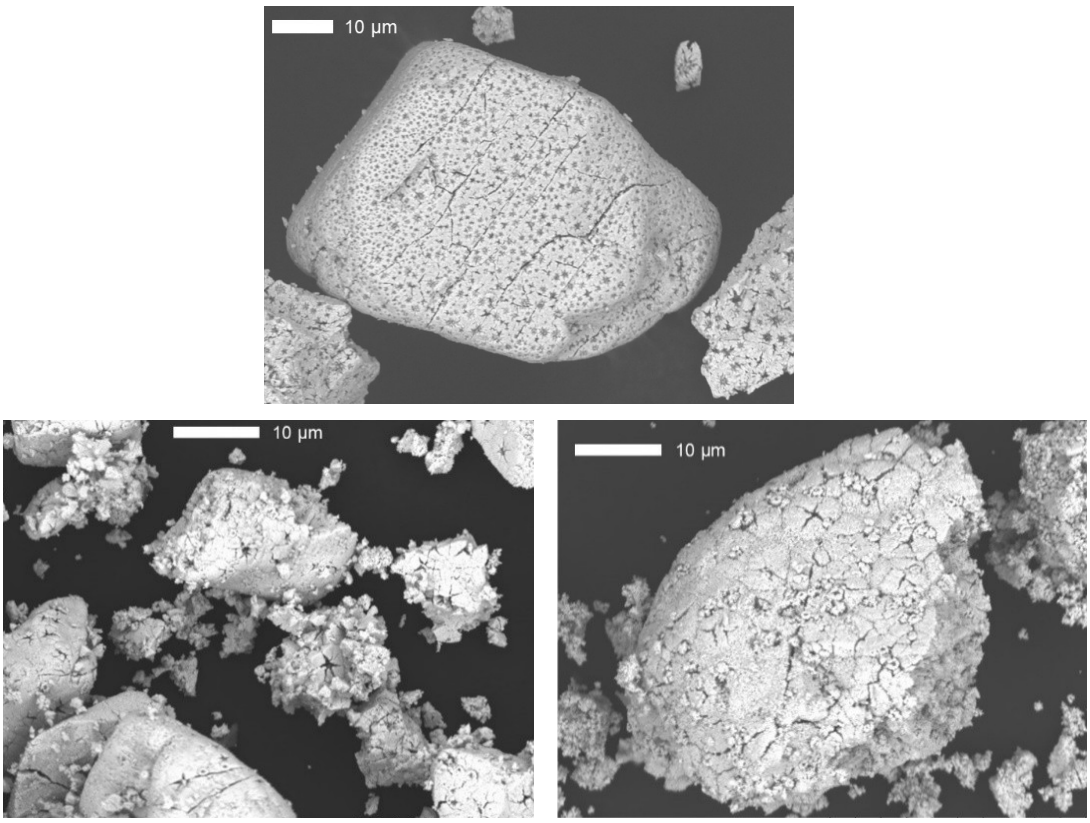

Figure 7*:* SEM images of the products from hydrogen reduction of the WO_3 precursor at different temperatures (1000x magnification). Top: 550 °C; bottom left: 700 °C; bottom right: 800 °C.

2.2.3 Reasons for the formation of the different tungsten phases

Beta tungsten, as a modification of tungsten metal, is significantly less studied in literature than the alpha phase of tungsten. In contrast to the body-centered cubic crystal structure of alpha tungsten, beta tungsten crystalizes in a cubic A15 structure (Pm3n)[164] and is slightly less dense at 18.83 g/cm^3 vs 19.16 g/cm^3 for alpha tungsten. The phase is described as a low temperature, meta-stable modification, which can be transformed to alpha tungsten by temperature increase.[165] The reaction conditions leading to beta tungsten are rather complex as factors such as the water vapor in the reduction atmosphere or the state of the starting material can play a role.[159],[164],[166],[167],[168] Related to such observations, a number of reasons can be found in the literature for stabilization of beta tungsten: impurities, kinetics, and surface energy. Thermodynamically, alpha tungsten is 0.127 eV/atom more stable than beta tungsten[169] while beta tungsten has a smaller surface energy, ~ 3.4 J/m^2 vs ~ 4 J/m^2 for alpha tungsten.[170] Therefore, at small crystallite sizes, beta-tungsten should become the stable phase.[171] For spherical crystals, the stability of the two phases would be equal around a size of 3 nm, and, consequently, the beta phase would be thermodynamically preferred already at larger sizes for other shapes. This behavior is of particular relevance and interest for the synthesis of tungsten carbide (W_2C) catalysts of higher surface areas.

2.3 Carburization of metallic alpha and beta tungsten

2.3.1 Overview

Here, the carburization of the metallic tungsten phases prepared by reduction of WO_3 described in section 2.2 is reported. The complete synthesis procedure includes reduction followed by carburization, as illustrated in Scheme 12.

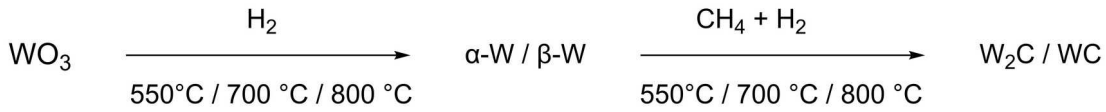

Scheme 12: Reaction sequence of tungsten carbide synthesis via separated reduction and carburization as used in this study.

To evaluate and optimize the final tungsten carbide phase purity and morphology, the most relevant carburization conditions - temperatures, time, and carburization gas composition - have been varied. The synthesis duration needs to be sufficiently long in order to achieve full conversion of metallic tungsten. The gas composition (methane to hydrogen ratio) requires a balance such that during carbide formation, CH_4 adsorbs onto the metallic tungsten surface and dissociates into adsorbed carbon or CH_x species and hydrogen. This can, however, lead to a build-up of carbon on the surface if the migration of carbon into the metal lattice is significantly slower than the decomposition of CH_4.[110] Hydrogen mitigates carbon buildup by reacting with adsorbed carbon species, but an excessive hydrogen partial pressure can lead to insufficient carbon availability for complete tungsten carbide formation.[122]

2.3.2 Phase evolution during carburization

Carburization of metallic tungsten as bulk powder was investigated at 550 °C and 700 °C by *in situ* XRD. Prior to carburization, the WO_3 precursor was reduced isothermally in the *in situ* cell at the same temperature (550 °C or 700 °C). The evolution of the XRD pattern for carburization at 550 °C is shown in Figure 8. The reaction of the β-W phase to tungsten carbide proceeded very rapidly (Figure 9), as after 20 min under CH_4 and H_2, 79% of the β-W phase was already converted to W_2C. No more reflections of β-W were present in the XRD pattern after 30 min under CH_4 and H_2 gas flow (see Figure 9). After complete conversion of β-W to W_2C, no significant changes in the product XRD pattern occurred even after 240 min under CH_4 and H_2. This shows that the W_2C phase is stabilized against further reaction to WC under these conditions, see 2.3.4 for further discussion of this behavior. No sintering was observed, as the W_2C crystallite sizes remained in the range of 7 to 8 nm over time.

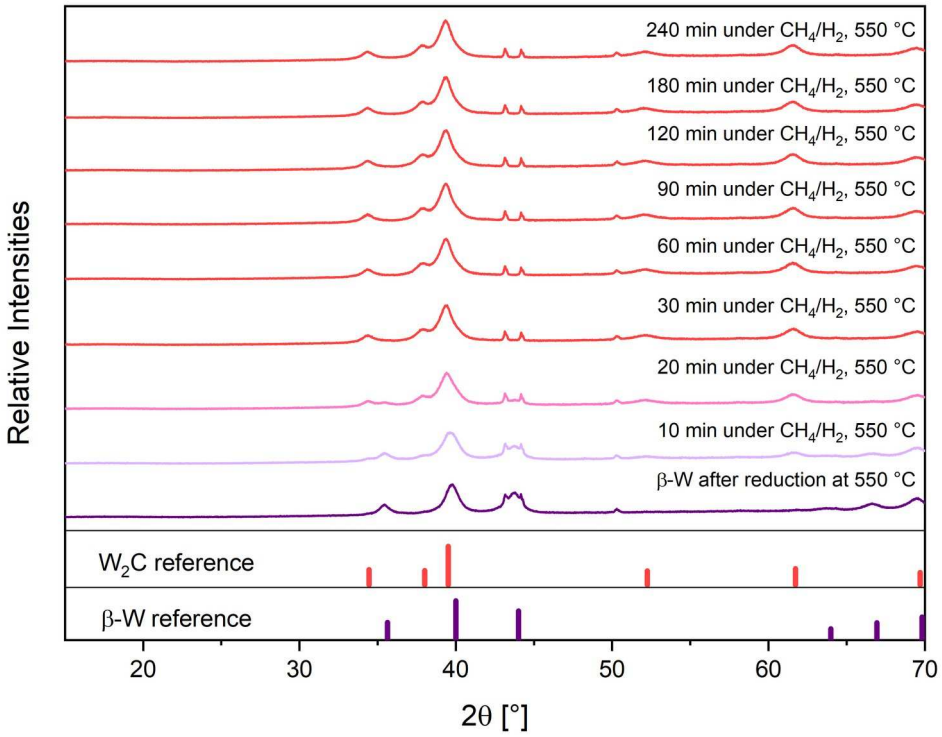

Figure 8: Evolution of the XRD patterns during in situ isothermal carburization of tungsten at 550 °C directly after isothermal reduction at 550 °C of WO_3. The carburization was performed using a 2:1 mixture of CH_4 and H_2 and a 100 mL/min total gas flow. The minor reflections at 43.1°, 44.2° and 50.4° stem from the sample holder of the In-situ XRD cell. The reference patterns were sourced from the following database entries: Beta tungsten: ICSD-150496. W_2C: ICSD-619097.

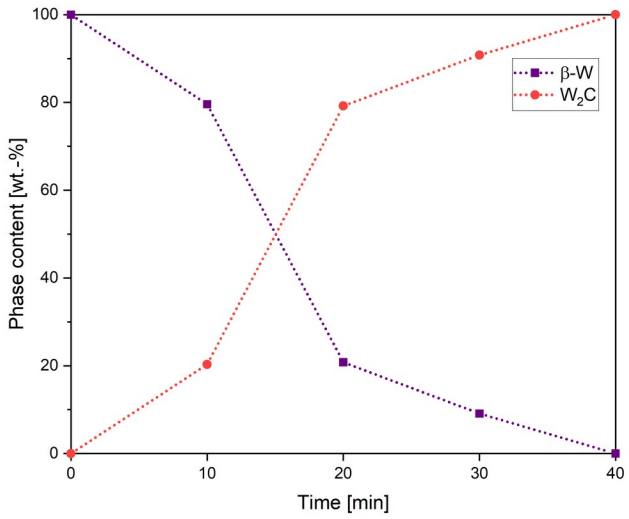

Figure 9: Change of the phase composition over time during in situ isothermal carburization of tungsten at 550 °C directly after isothermal reduction at 550 °C of WO_3. The carburization was performed using a 2:1 mixture of CH_4 and H_2 and a 100 mL/min total gas flow. The quantification was conducted by Rietveld refinement using the following reference patterns Beta tungsten: ICSD-150496. W_2C: ICSD-619097.

Carburization of metallic alpha tungsten (obtained by reduction at 700 °C in H_2) at a temperature of 700 °C was investigated by *in situ* XRD, as shown in Figure 10. Upon introduction of the carburization gas mixture, conversion of α-W was observed. W_2C was formed as the first carbide phase but reacted further to WC. However, the conversion of W_2C to

WC progressed significantly more slowly than the conversion of α-W to W_2C, see Figure 11. In addition, the rate of conversion of W_2C to WC became slower over time (Figure 11). The maximum portion of W_2C was present after 60 min of carburization, with a phase content of 79 wt.-% (2 wt.-% WC and 20 wt.-% α-W). The phase content of W_2C decreased to 74 wt.-% after 90 min of carburization with a significant increase in the content of WC to 21 wt.-% and further decline of α-W to 5 wt.-%. This trend continued in a similar manner until 180 min under carburization gas with a further decline of the W_2C content to 33 wt.-% and an increase of the WC content to 66 wt.-%. In the time interval between 180 min and 240 min, the changes in the phase composition were more subtle with an increase of the WC content of only 4 wt.-% to 70 wt.-%. After 240 min under CH_4/H_2 flow, the conversion of W_2C was still incomplete. It is possible that full transformation to WC would occur, as observed under similar conditions during catalyst synthesis (Figure 12). Nevertheless, further investigations with extended carburization times are required to confirm this.

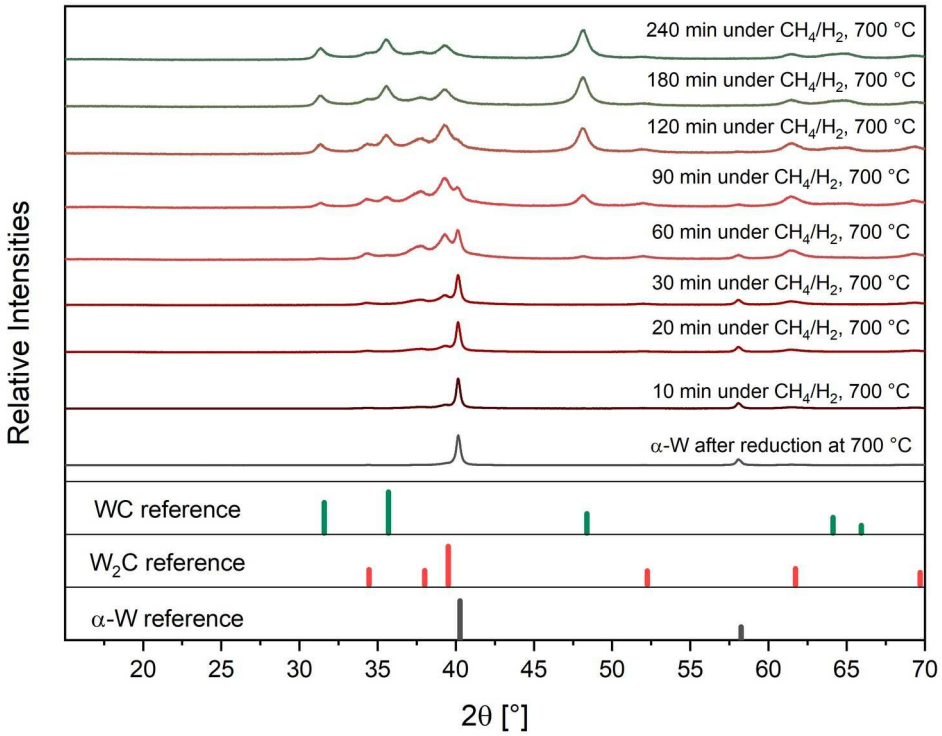

Figure 10: Evolution of the XRD patterns in the course of in situ isothermal carburization of tungsten at 700 °C directly after isothermal reduction at 700 °C of WO_3. The carburization was performed using a 4:1 mixture of H_2 and CH_4 and a 100 mL/min total gas flow. The reference patterns were sourced from the following database entries: Alpha tungsten: ICSD-44393. W_2C: ICSD-619097. WC: ICSD-5212.

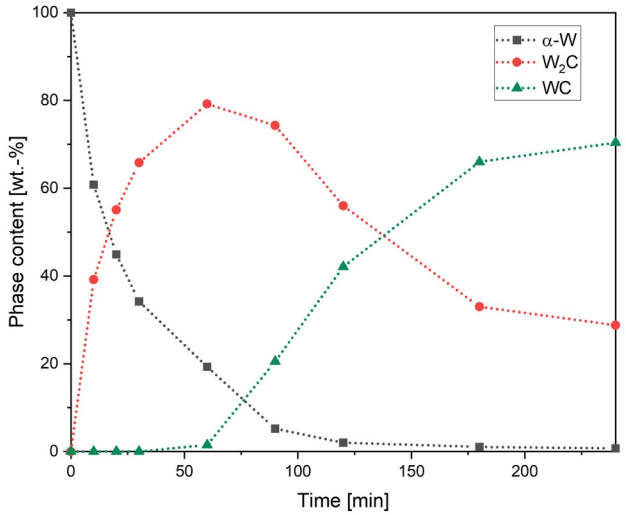

Figure 11: Change of the phase composition over time during in situ isothermal carburization of alpha tungsten at 700 °C directly after isothermal reduction at 700 °C of WO_3. The carburization was performed using a 4:1 mixture of H_2 and CH_4 and a 100 mL/min total gas flow. The quantification was conducted by Rietveld refinement using the following reference patterns: Alpha tungsten: ICSD-44393. W_2C: ICSD-619097. WC: ICSD-5212.

As shown by the *in situ* XRD studies, the conversion of β-W proceeded in principle much faster than that of α-W, when the temperature is taken into account. Transformation rates, determined from the decline of the tungsten phase content over time, showed that α-W exhibited a higher initial rate during the first 10 minutes of carburization (7.6 µmol(tungsten)/min) compared to β-W (4.0 µmol(tungsten)/min), see Table 3. However, when the initial rates were calculated over the first 20 minutes, the trend was reversed, with β-W reaching 7.7 µmol(tungsten)/min versus 5.3 µmol(tungsten)/min for α-W. This indicates that α-W transformed most rapidly immediately after the onset of carburization, with the rate declining thereafter (Figure 11), whereas β-W exhibited its maximum transformation rate in the 10–20 minute interval following the start of carburization (Figure 9). Moreover, full tungsten conversion was reached after 40 min for β-W, much earlier than in the case of α-W (180 min, compare Figure 9 and Figure 11). In addition, it is important to consider that carburization of β-W was performed at 550 °C, while that of α-W was performed at 700 °C, a temperature gap of 150 K. This clearly indicates significant differences in the carburization kinetics between α-W and β-W. However, more comprehensive solid-state kinetic investigations and theoretical calculations are required for accurate quantitative analysis of this effect. Also, it has to be noted that the higher specific surface area of the β-W precursor would increase the rate of conversion; however, surface area alone is not sufficient to account for such a pronounced difference in rate. More likely, the β-W is inherently more reactive toward carburization than α-W. In fact, conversion of α-W to tungsten carbide was not possible at 550 °C, even at prolonged synthesis duration. This underlines the relevance of the investigated synthesis strategy with separated reduction and carburization. By using β-W as an intermediate, the synthesis of tungsten carbide can be accomplished at significantly lower temperatures.

Table 3: Overview of the tungsten transformation rates during the in situ XRD carburization measurements as calculated from the changes in the phase contents of the tungsten phase.

Phase	Temperature [°C]	Transformation rate 0-10 min [µmol(tungsten)/min]	Transformation rate 0-20 min [µmol(tungsten)/min]
α-W	550	7.6	5.3
β-W	700	4.0	7.7

The corresponding reduction-carburization experiments in the horizontal tube furnace gave results similar as those observed in the in situ XRD measurements. As shown in Figure 12, temperature has a strong influence on the phase composition of the products. Reduction and carburization of the WO_3 precursor at 550 °C resulted in pure W_2C, while reduction and carburization at 700 °C (with 4 h holding time during carburization) resulted in pure WC. Reduction and carburization at 800 °C also produced pure WC.

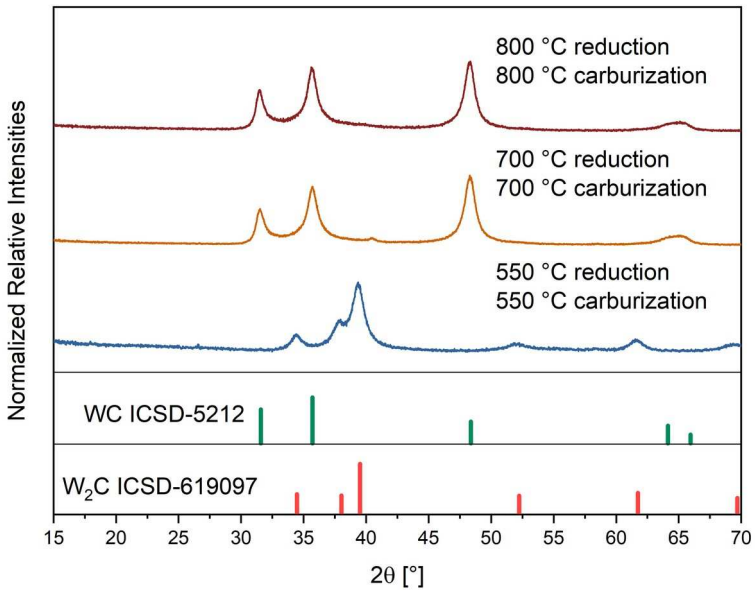

Figure 12: XRD patterns of the products from stepwise synthesis of tungsten carbide via isothermal reduction and carburization of WO_3-SiO_2 at different temperatures. Reference stick patterns were included for W_2C (ICSD-619097) and WC (ICSD-5212).

The beta tungsten prepared by reduction at 550 °C was also carburized at 700 °C and 800 °C. The XRD patterns of the resulting products are presented in Figure 13 (along with the beta tungsten carburized at 550 °C). While carburization of beta tungsten at 550 °C resulted in pure W_2C, carburization at 700 °C and 800 °C resulted in phase pure WC. The combination of a low reduction temperature with a low carburization temperature is therefore the only route to phase-pure W_2C.

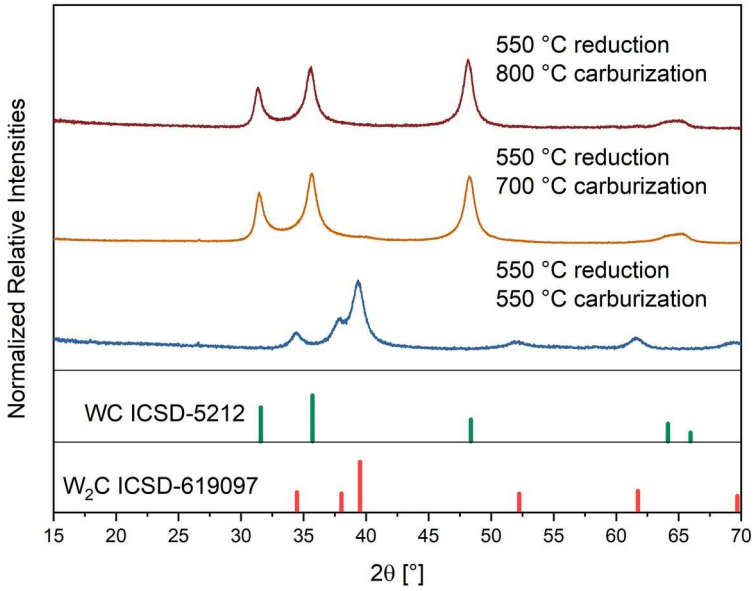

Figure 13: XRD patterns of the catalysts synthesized by reduction of WO_3 at 550 °C followed by carburization at varying temperatures. Reference stick patterns were included for W_2C (ICSD-619097) and WC (ICSD-5212).

2.3.3 Properties of the carbides and their dependence on the synthesis parameters

The crystalline domain sizes of the carbides generated in the synthesis furnace are summarized in Table 4, together with other properties. The crystallite sizes, determined from XRD reflection broadening, increased slightly with rising synthesis (reduction plus carburization) temperature (Table 4) from around 7 nm at 550 °C to 9 nm at 700 °C and to 12 nm at 800 °C. The crystallite domain sizes also increased when only the carburization temperature was elevated. However, this increase was rather gentle, with approximately 7.5 nm for 550 °C, 8.9 nm for 700 °C, and 9.7 nm for 800 °C carburization (Table 4). Alpha tungsten could not be carburized at 550 °C.

SEM images show that the morphology of the tungsten carbide products strongly resembles their tungsten metal precursors (Figure 14). With a reduction temperature of 550 °C, all three carburization temperatures leave the particles with a similar size, with predominantly rounded edges, and with the star-shaped cracks that are present after reduction. In the same vein, carburization after reduction at 700 °C or 800 °C resulted in more broken particles with jagged edges. Hence, it can be concluded that the most significant structural changes occur during the reduction of WO_3, and thereafter, the morphology is preserved during carburization.

Interestingly, the BET surface areas of all five carbide samples were similar (Table 4). The highest BET surface area was observed for the sample reduced and carburized at 550 °C with 25 m^2/g, while those carburized at 700 °C or 800 °C were about 20 m^2/g. The pore volumes of the catalysts determined by physisorption were also very similar with values around 0.055 mL/g. An exception was the two catalysts with 800 °C carburization, which exhibited pore volumes of 0.077 mL/g (550 °C reduction) and 0.066 mL/g (800 °C reduction). This can likely

be explained by a more pronounced porous carbon deposition separated from the tungsten carbide surface at these high carburization temperatures (800°C). These deposits can obviously not be removed under the conditions applied through reduction by hydrogen, which is not activated by a catalyzing tungsten carbide surface. This separately deposited porous carbon, however, does not influence the catalytic hydrogenation reaction (see below).

For the carbides that were carburized from beta tungsten, CO chemisorption measurements show a decline in the CO uptake with higher carburization temperature, from 0.0038 to 0.0010 to 0.0007 mol CO per mol W for the carburization temperatures 550 °C, 700 °C, and 800 °C, respectively (Table 4). For the carbides that were carburized from alpha tungsten, carburization at 700 °C resulted in a CO uptake of 0.0011 mol CO per mol W, and carburization at 800 °C resulted in a CO uptake of 0.0001 mol CO per mol W.

These results show substantially different CO coverages for the different samples. The W_2C sample had substantially higher uptake than the other samples, and the somewhat greater surface area for the W_2C sample does not alter this conclusion. Of course, quantification of the tungsten carbide active surface with CO adsorption is not well developed because the stoichiometry of CO adsorption for W_2C and WC is unclear. Volpe and Boudart reported that adsorption only occurs in 11% of a monolayer, while Ribeiro *et al.* found up to 40% coverage.[126],[172] Moreover, it is possible that the CO adsorption behavior and hence the stoichiometry is different for W_2C and WC. Bretzler *et al.* arrived at the conclusion that W_2C contributes significantly more to CO adsorption than WC.[65] It is also important to consider that both the CO adsorption and, to a lesser extent, the BET surface area and BJH pore volume measurements can be influenced by the presence of carbon on the surface or in pores. Due to the inability to transfer the catalyst into the chemisorption unit without exposure to air, carbide synthesis was directly performed in the chemisorption unit using the same synthesis parameters. It has to be kept in mind that this can lead to differences in the properties of the materials to some extent, especially due to differences in the removal of excess carbon at the end of the synthesis. Overall, it is noted that the interpretation of the CO uptake is highly complex, with various factors casting doubt on its significance for quantifying the active surface sites of tungsten carbide. Therefore, the BET surface area serves as a more reliable method in this investigation for the assessment of the catalyst surface structure.

Table 4: Summary of the product characteristics after isothermal carburization at varying temperatures for different precursors.

Reduction temperature	Carburization temperature	Phase composition	Crystallite size[a] [nm]	BET surface area [m^2/g]	BJH Pore Volume [mL/g]	CO uptake [mol_{CO}/mol_W]	CO adsorbed per m^2 [mol/m^2]
550 °C	550 °C	100wt.-% W_2C	7.5 ± 0.7	25	0.056	0.0038 ± 0.0003	8.0 E-7
550 °C	700 °C	100wt.-% WC	8.9 ± 0.7	21	0.055	0.0010 ± 0.0001	2.5 E-7
550 °C	800 °C	100wt.-% WC	9.7 ± 0.7	20	0.077	0.0007 ± 0.0001	1.8 E-7
700 °C	700 °C	100wt.-% WC	8.5 ± 0.4	20	0.055	0.0011 ± 0.0001	2.8 E-7
800 °C	800 °C	100wt.-% WC	12.3 ± 0.7	20	0.066	0.0001 ± 0.0001	2.5 E-7

[a] as determined from the FWHM of the XRD reflections using the Scherrer equation. The reflections at 34.4 °, 37.8 °, 39.3 ° and 61.6 ° were used for W_2C and the reflections at 31.3 °, 35.6 °, 48.2 °were used for WC.

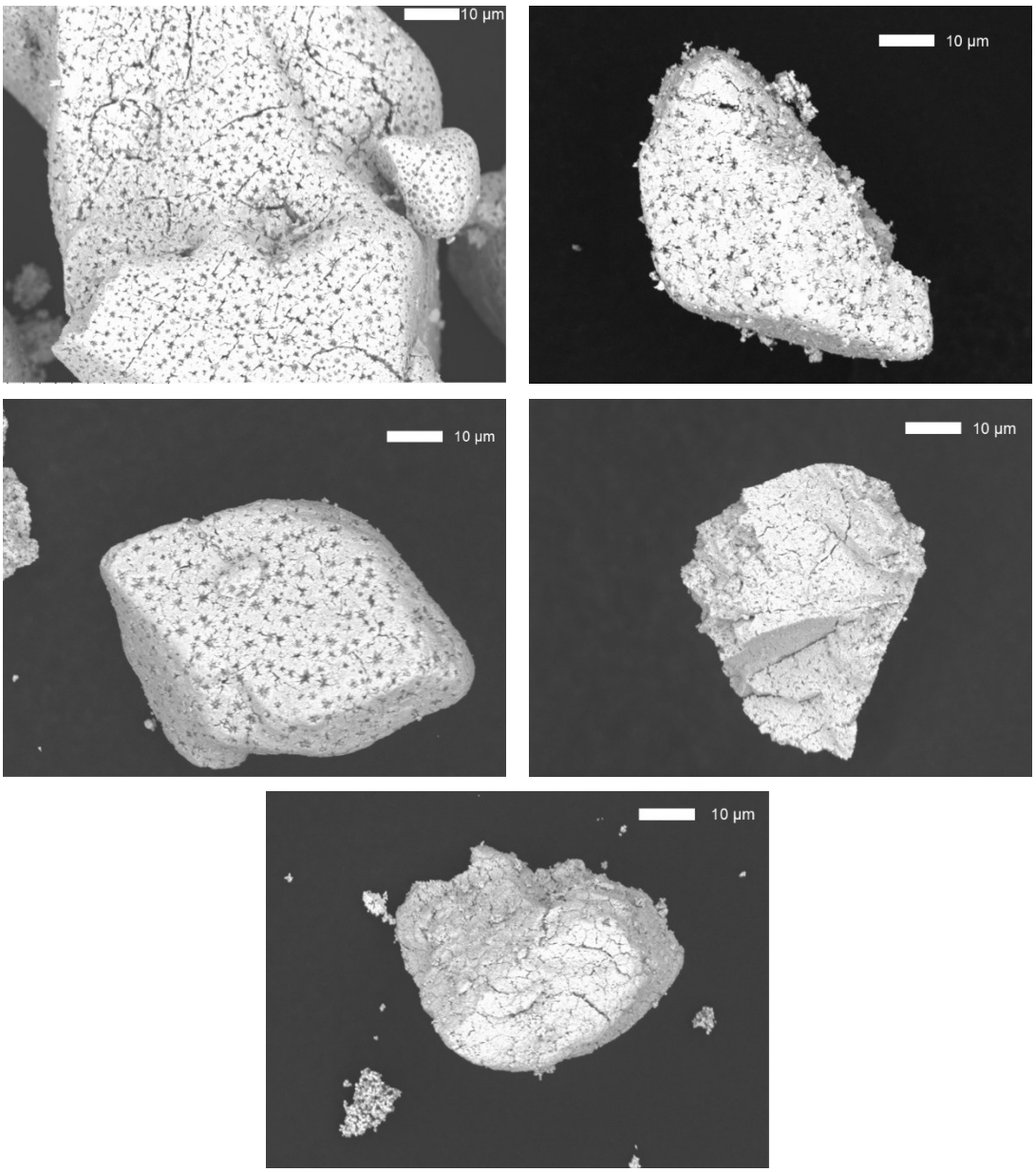

Figure 14: SEM images of the products from stepwise tungsten carbide synthesis via reduction and carburization of WO_3 bulk (1000x magnification). Top left: reduction and carburization at 550 °C. Top right: reduction at 550 °C, carburization at 700 °C. Center left: reduction at 550 °C, carburization at 800 °C. Center right: reduction and carburization at 700 °C. Bottom: reduction and carburization at 800 °C.

2.3.4 Discussion on the role of surface area for phase stability

Tungsten carbide exists primarily in two different stoichiometries: tungsten monocarbide WC and tungsten semicarbide W_2C.[95] The most stable phase below 1250 °C is hexagonal WC (δ-WC), which features a simple hexagonal lattice of tungsten atoms with carbon atoms filling the octahedral vacancies.[96] W_2C can exist in a variety of polymorphs (α, β, γ, ε or β, β', β'', ε).[97],[98] All of these share the same hcp lattice of tungsten atoms, but with different locations of carbon, making them practically indiscriminate by X-ray diffraction.[99]

Consistent with the results of Gao and Kear, separated synthesis of tungsten carbide allowed for more control over the phase composition. It is evident that the influence of the tungsten metal phase on the tungsten carbide phase can be rationalized by two effects. First, the W_2C phase might be kinetically stabilized as carbon diffusion can be the rate-limiting step in carburization of metallic tungsten.[107] The rate of carbon diffusion was shown to be dependent on the carbon concentration in tungsten, resulting in slower carbon diffusion in W_2C compared to metallic tungsten.[173] Higher temperatures, therefore, favor the transformation of W_2C to WC due to faster carbon diffusion. The higher reactivity of beta tungsten toward carburization allows for a lower synthesis temperature, which hinders further reaction to WC. In addition to kinetic effects, it can be assumed that thermodynamic considerations, as a second factor, also play a role through surface energy contributions to phase stability. It is known from literature that the particle size of nanoparticles can have an effect on the phase stability.[171],[174] The surface-to-volume ratio increases strongly with smaller particles, which can lead to surface energy contributions surpassing bulk energy contributions.[175] Metastable phases with high bulk energy, but low surface energy, can therefore become thermodynamically favored when increasing the specific surface area of a material.[176] This effect has been shown for a large variety of materials. For instance, anatase becomes the preferred TiO_2 phase over rutile for particle sizes below roughly 14 nm.[177] Similarly, the metastable γ-Al_2O_3 phase becomes energetically more stable under standard conditions than α-Al_2O_3 for specific surface areas above 125 m^2/g.[178] Theoretical work of Shrestha *et al.* show that the same principle also applies for tungsten carbide.[175] The authors predict hexagonal WC as the most stable tungsten carbide modification at particle sizes above 10 nm, while W_2C becomes the dominant stoichiometry below 10 nm. This trend follows the surface energies of the specific surface energies of the phases, with 3.93 J/m^2 for hexagonal WC and 2.28-2.83 J/m^2 for W_2C.[175] Moreover, Shrestha *et al.* predicted that the cubic WC_{1-x} modification is the most stable phase below 2.5 nm, as it has the lowest surface energies of all tungsten carbide modifications (0.74 J/m^2).[175] Consistent with these general trends, Bretzler *et al.* experimentally observed that W_2C crystalline domains dominate below 10 nm, while WC prevails at larger sizes above 10 nm.[65] The observed crystallite size of WC in this study was consistently larger than 8 nm (Table 4), whereas that of W_2C was below 8 nm, in good agreement with the proposed cut-off size of 10 nm cited above. These results suggest that the W_2C phase of the W_2C catalyst was thermodynamically stabilized by surface energy contributions. This interpretation is further supported by the *in situ* XRD carburization experiment at 550 °C. Even after prolonged carburization for 240 min, no reflexes of WC were detected (Figure 8), indicating the suppression of W_2C to WC conversion.

2.4 Catalytic performance of W_2C and WC in the hydrogenation of butyraldehyde

2.4.1 Catalysis results

The products of the carbide syntheses were subsequently used as catalysts in the hydrogenation of butyraldehyde to 1-butanol, which can serve as a model reaction for the assessment of the catalytic activity of tungsten carbide.[65] The reaction was performed in a liquid-phase batch process at 200 °C, 65 bar H_2 pressure, and with ethanol as solvent. Comparable product selectivity to 1-butanol of roughly 80% was observed for all catalysts. Deoxygenation reactions are expected to be the main contributors to incomplete carbon balance through the formation of butane and butene, which could not be determined by gas chromatography of the liquid phase.[56],[65] However, since the selectivity was similar, the catalytic performance could be assessed by the 1-butanol formation rate. It is noted that some uncertainty remains in the product distribution, with possible deviations depending on the catalyst.

As the primary goal of the study was to compare the intrinsic catalytic activity of phase-pure W_2C and WC, it was focused on the initial catalytic performance, and long-term stability tests were not conducted. Due to deviations in the individual catalyst loadings, the 1-butanol formation rates were normalized to the molar amount of tungsten. The experimental error resulting from the different catalyst loadings was evaluated for a representative catalyst, indicating that the deviation falls approximately within the range of the general quantification error.

The rates normalized to the molar amount of tungsten are presented in Figure 15. A clear performance gap between the two tungsten carbide phases, W_2C and WC, is evident. The 1-butanol formation rate of the catalysts with WC as a product phase ranged from approximately 7 $mmol_{BuOH}/(mmol_W\ h)$ to 13 $mmol_{BuOH}/(mmol_W\ h)$, while that of the catalyst with W_2C was higher and around 19 $mmol_{BuOH}/(mmol_W\ h)$.

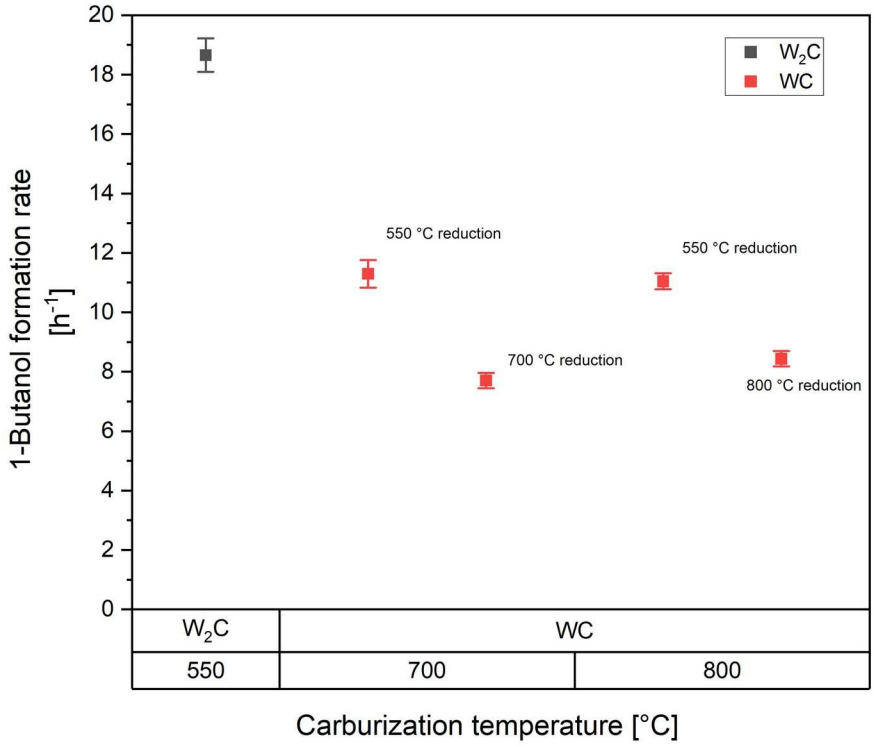

Figure 15*:* 1-Butanol formation normalized to the tungsten content for tungsten carbide catalysts prepared by reduction of WO_3 followed by carburization. The catalytic tests were conducted at 200 °C, under a 65 bar H_2 atmosphere and with ethanol as solvent using 0.05 g of catalyst and 4 g of butyraldehyde, equivalent to a butyraldehyde-to-tungsten molar ratio of approximately 210.

Since the differences in the tungsten carbide surface areas are small (2.3.3, Table 4, SEM images), these results strongly indicate the superior catalytic hydrogenation activity of W_2C over WC. An influence of the catalyst surface areas can be concluded from the comparison of the tungsten monocarbide, WC, catalysts prepared by reduction at 550 °C and variable carburization temperatures. The WC catalysts prepared at 550 °C reduction, followed by 700 °C and 800 °C carburization, performed better than the corresponding catalysts with both steps at the same temperature. The presentation of the 1-butanol formation rate normalized to the BET surface areas of the catalysts gives, therefore, a very similar picture (Figure 16 and Table 5). Although the performance gap between W_2C and WC decreases from 65 % ± 3 % to 30 % ± 1 % when surface area effects are considered, W_2C still shows a clear and significant advantage in catalytic performance. The problems of CO chemisorption data in general have been discussed above together with the discrepancies in the literature. In particular, the different unit used for material synthesis for the chemisorption experiments limits the significance of the chemisorption data. For this reason it was refrained from assessing the 1-butanol formation rate normalized to CO uptake in order to avoid potentially misleading conclusions. The application of alternative probe molecules, such as N_2O, for quantification of the active surface sites, represents an important direction for future investigations.

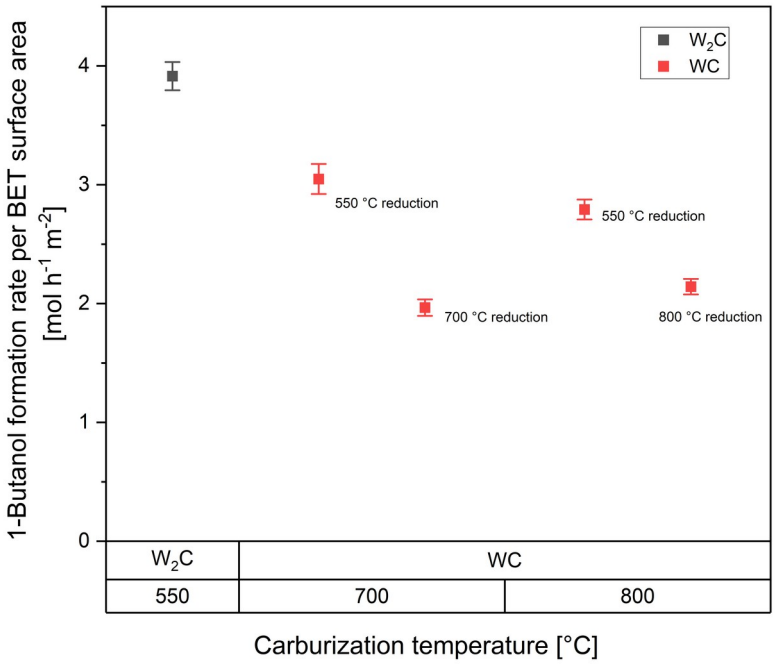

Figure 16: 1-Butanol formation rate normalized to the BET surface area of the catalysts.

Table 5: Overview of the 1-Butanol formation rates including 1-Butanol rates normalized to the BET surface areas and 1-Butanol formation rates normalized to the CO uptake.

Reduction temperature	**Carburization temperature**	**Phase composition**	**Butanol formation rate [mol mol_W^{-1} h^{-1}]**	**1-Butanol formation rate normalized to BET surface area [mol h^{-1} m^{-2}]**	**1-Butanol formation rate normalized to CO uptake [s^{-1}]**
550 °C	550 °C	W_2C	18.6 ±0.6	18.6 ±0.6	1.4
550 °C	700 °C	WC	11.3 ±0.5	12.2±0.5	3.1
550 °C	800 °C	WC	11.0 ± 0.3	10.3± 0.3	4.4 ± 0.1
700 °C	700 °C	WC	7.7 ± 0.3	7.6 ± 0.3	1.9 ± 0.1
800 °C	800 °C	WC	8.4 ± 0.3	8.2 ± 0.3	23.4 ± 0.7

2.5 Discussion on the catalytic activity of W_2C and WC

As described earlier, literature reports on the differences in the intrinsic catalytic activity of the two main tungsten carbide modifications, W_2C and WC, are very rare. In the context of thermal heterogeneous catalysis, this topic was, for the most part, only addressed as a side note, particularly because of the general difficulty in obtaining the pure phases. Neylon *et al.* found a slightly higher n-butane conversion over a W_2C bulk catalyst with 112 nmol/m^2 s compared to a WC bulk catalyst with 95 nmol/m^2 s in the dehydrogenation, hydrogenolysis, and isomerization of n-butane.[179] Fang *et al*. investigated tungsten carbide catalysts embedded in carbon spheres (W_xC/CS) in the hydrogenolysis of guiacol and reported a significantly lower apparent activation energy for W_2C/CS with 111.1 kJ/mol compared to WC/CS with 151.9 kJ/mol.[180] The authors rationalized the different catalytic behavior by differences in the electron density distribution between W and C between W_2C and WC. Moreover, structural effects on the carbide surface, such as a higher amount of carbon defects and W-terminated sites for W_2C, were assumed to facilitate the adsorption of oxygen-containing groups.[180]

In contrast to the field of thermal catalysis, the phase-dependent catalytic activity of tungsten carbide for the hydrogen evolution reaction (HER) has been investigated in more detail. Gong *et al*. performed theoretical calculations suggesting a potentially higher intrinsic HER performance of W_2C compared to WC.[143] In addition, they experimentally tested carbon nanotube-supported W_2C and WC as electrocatalysts under acidic conditions and observed a higher HER activity for W_2C. The authors explained their results by the inherently different properties of W_2C and WC in terms of the Gibbs free energy of hydrogen adsorption (ΔG_H) and the electronic density of states (DOS) near the Fermi level. They calculated a ΔG_H on the (0001) surface of -0.56 eV for WC and a ΔG_H of -0.31 eV for W_2C for a hydrogen coverage of ¼ monolayer. This would mean that W_2C is closer to the optimum ΔG_H of 0 than WC. Both materials are limited by the hydrogen release step, as they feature negative ΔG_H. Other studies calculating the ΔG_H on W_2C and WC came to similar conclusions.[181] Esposito *et al*. calculated a ΔG_H of -0.99 eV for a WC(0001) surface and a ΔG_H of -0.67 eV. for a W_2C(0001) for a hydrogen coverage of 1/9 monolayer.[182]

Another strong expectation for the different catalytic behavior of W_2C and WC in both thermal and electrocatalysis is the different electronic DOS near the Fermi level. In fact, the significantly higher catalytic activity of WC compared to tungsten metal was explained already very early in the history of research on tungsten carbide for catalytic purposes. Bennett *et al.* demonstrated in 1974 by X-ray photoelectron spectroscopy (XPS) of the valence band and core levels that WC has a higher DOS near the Fermi level than W.[42] This makes the electronic structure of WC more similar to Pt than to tungsten metal. Colton *et al.* specified that the occupied electronic DOS are similar to Pt, while the unoccupied electronic DOS are different.[43] They also showed that electron density shifts from the tungsten 5d orbitals to the C 2p orbitals, which

results in a higher catalytic activity of WC compared to W. More recently, Gong *et al.* confirmed by density functional theory (DFT) calculations the high electronic DOS close to the Fermi level.[143] In fact, they also calculated an even larger DOS near the Fermi level for W_2C compared to that of WC. The authors also showed that the d-band center of $W_2C(0001)$ is much lower than that of WC(0001) and closer to that of Pt(111). This is in line with the more advantageous ΔG_H for W_2C as a lower d-band center is associated with weaker bonding between the catalyst and adsorbate.[143] Suetin *et al.* also calculated that the metallic character of W_2C is stronger than that of WC.[97] All these results point to inherently different catalytic behavior of W_2C and WC. Interestingly, the pioneering work of Levy and Boudart 1973 showing Pt-like behavior for WC used a WC-based material with slight carbon deficiency, as later shown by Ross and Stonehart.[41],[44] The latter authors also observed strong parallels in hydrogen chemisorption characteristics for W_2C and the tungsten carbide used by Levy and Boudart, in contrast to WC, which again hints at different catalytic properties depending on the carbon content in tungsten carbide.

The present study further confirms these differences by providing a first direct comparison of the pure bulk phases W_2C and WC in hydrogenations. The stepwise synthesis approach for tungsten carbide allowed to prepare phase-pure W_2C and WC catalysts with comparable active surface areas. Clear differences in the catalytic hydrogenation of butanal to 1-butanol were observed with higher catalytic activity of W_2C compared to WC. This also matches the findings of Bannert *et al*.[183] The authors observed significant differences in the HER performance of W_2C and WC in a gas-phase solid-acid electrolyzer. Phase-pure materials with comparable BET surface areas were applied as electrode material. Within the investigated temperature range of 200-240 °C, W_2C showed higher HER performance than WC. Moreover, different properties regarding electric conductivity were found. While both materials show semi-conducting behavior, the dominant charge carrier type differs between WC (p-type) and W_2C (n-type). It has to be noted that testing additional hydrogenation and deoxygenation reactions will be necessary to further assess the extent to which the W_2C > WC activity trend can be generalized for this type of reaction, as the catalytic comparison is based solely on butyraldehyde hydrogenation in this study. Moreover, the phase-dependent catalytic activity might be different for other types of reactions, such as isomerization.

Significantly more pronounced formation of 1,1-diethoxyethane (also called acetal) was observed over WC catalysts from ethanol as the solvent, as summarized in Table 6. This may imply that WC has more pronounced acidic-base properties than W_2C and is better suited to reactions that profit from these properties, such as isomerization. Further investigations on phase-pure W_2C and WC bulk catalysts in such reactions, combined with in-depth characterization using techniques such as CO-Temperature programmed desorption (TPD) and NH_3-TPD, will be necessary to achieve a more comprehensive understanding of their

acid–base properties. Different reaction chemistries could be an interesting prospective investigation.

Table 6: Summary of the 1,1-diethoxyethane formation rates observed for the different tungsten carbide catalysts.

Reduction temperature [°C]	Carburization temperature [°C]	Phase	1,1-diethoxyethane formation [mmol 1,1-diethoxyethane formed per hour per W]
550	550	W_2C	3.7 ± 0.1
550	700	WC	9.0± 0.1
550	800	WC	10.8 ± 0.2
700	700	WC	8.9 ± 0.1
800	800	WC	5.6± 0.2

2.6 Conclusion

Unsupported tungsten carbide catalysts can be synthesized from tungsten oxide using a two-step approach with separated reduction and carburization. The products of WO_3 reduction differ depending on the temperature. The metastable beta tungsten modification is formed at 550 °C, while reduction at 700 °C and 800 °C leads to alpha tungsten. Surface energy contributions appear to be relevant in stabilizing the beta tungsten phase.

The reduction mechanism shows deviations in the sequence of intermediate species during the reduction of WO_3, depending on the reduction temperature, which can be concluded from *in situ* XRD investigations of the solid-state reactions. The two tungsten phases differ drastically in their reactivity toward carburization. The conversion of beta tungsten to W_2C progressed significantly faster than that of alpha tungsten to W_2C and further to WC. This tendency can be exploited for tungsten carbide synthesis at lower temperatures than conventionally, demonstrating a significant strength of this synthesis approach.

The catalytic properties of the W_2C and WC in the hydrogenation of butanal to 1-butanol differ clearly for comparable tungsten carbide dispersions. W_2C shows substantially higher intrinsic hydrogenation activity of W_2C compared to WC, which also aligns well with theoretical work from the literature.

The results of this chapter highlight the advantages of the alternative two-step synthesis route, providing an approach to adjust the phase composition of tungsten carbide-based materials. Moreover, testing in other hydrogenation and deoxygenation reactions is required for the generalization of the phase-dependent activity.

2.7 Disclaimer

This chapter (Chapter 2, as well as section 1.2 and parts of Chapter 6) is based on a manuscript published in *The Journal of Physical Chemistry C*, titled “Synthesis of Phase-Pure W_2C and WC by Separation of Reduction and Carburization and their Differing Performance as Hydrogenation Catalysts” with the following citation: [82]

Patrick Schlachta, Rolf E. Jentoft, Friederike C. Jentoft, Klaus Köhler, *The Journal of Physical Chemistry C*, **2025**, *129***,** 47, 20907-20921.
DOI: 10.1021/acs.jpcc.5c05153

The author of this dissertation (Patrick Schlachta) is also the first author of the manuscript. The contributions of Patrick Schlachta to the manuscript in the sense of the CRediT author statement definitions include conceptualization, investigation, methodology, validation, formal analysis, visualization and writing (original draft and editing). The content has been edited and restructured to some extent, to align with the format and context of this dissertation. All co-authors, that is Rolf E. Jentoft, Friederike C. Jentoft and Klaus Köhler have approved the use of the manuscript in this dissertation. The article is intended to be published as open access and is reused here for the purpose of this dissertation in accordance with the Creative Commons Attribution 4.0 International License (CC BY, see https://creativecommons.org/licenses/by/4.0/), which allows unrestricted reuse of the work in any medium or format, as long as appropriate credit is given to the original work.

3

Supported tungsten carbide catalysts for hydrogenation reactions

3.1 Motivation and aim[3]

The synthesis conditions strongly affect the performance of tungsten carbide catalysts. It is particularly challenging to prepare materials with a high surface area due to high synthesis temperatures. In the previous chapter (Chapter 2), it was shown that the phase composition of the catalysts is an important factor, as the intrinsic activity of the W_2C phase was found to be higher than the WC phase for hydrogenation reactions. It is therefore desirable to improve the tungsten carbide synthesis in order to maximize the surface area of the catalysts and to selectively obtain W_2C as the product phase. As described in the previous chapter, an effective way to achieve these goals is by performing reduction and carburization separately, similar as reported by Gao and Kear.[153] This allows to carry out reduction at relatively low temperatures (550 °C) to obtain high surface area β-W precursors, which can also be converted selectively to W_2C at the same low temperatures due to the higher reactivity of these materials towards carburization. While this approach was specifically investigated for bulk materials, it is an important next step to extend the investigation of this alternative synthesis method to supported tungsten carbide catalysts for improved understanding of the synthesis conditions and further enhancing the catalytic efficiency through higher tungsten carbide dispersion. Within the scope of this chapter, profound insight into how the synthesis conditions affect the catalyst structure and how these properties determine their catalytic performance is intended. For this purpose, four precursors with differing WO_3 dispersions were implemented in order to gain insight into the effect of the dispersion on the solid-state reactions concerning reduction and carburization. *In situ* XRD investigations are conducted to examine phase transitions in supported systems during synthesis. The influence of key synthesis parameters on the product characteristics after reduction and carburization is studied by XRD, BET, and partially by Transmission electron microscopy (TEM). The performance of the catalysts, depending on their structural properties, in hydrogenation reactions, shall be compared. Special emphasis shall be placed on the effect of tungsten carbide dispersion and phase composition, for further investigation of the different behavior of W_2C and WC.

3.2 Synthesis and characterization of the WO_3 based precursors

Different WO_3 based precursors were used for the synthesis of tungsten carbide: pure WO_3 and different silica-supported WO_3 precursors. Pure WO_3 was used from a commercial supplier, while the WO_3-SiO_2 precursors were synthesized by incipient-wetness impregnation. Fumed silica of the type *Aerosil*® with surface areas of 90 m^2/g, 200 m^2/g, and 380 m^2/g was used, although these surface areas were lower after agglomeration of the materials as a

[3] Disclaimer: This chapter (Chapter 3) is based on a manuscript, see section 3.7 for more information.

pretreatment. The agglomerated *Aerosil*® materials were impregnated with an aqueous solution of ammonium metatungstate. After loading the silica particles with the tungsten-salt solution, they were dried and calcined resulting in a mixture of tungsten (VI) oxide and silica. All SiO_2 supported WO_3 precursors were prepared with a tungsten content of approximately 50 wt.-% (30 mol.-%) as confirmed by elemental analysis. In order to distinguish between the different WO_3 precursor-related systems are from here on referred to as "(WO_3) Bulk", "AE90", "AE200", and "AE380". The numbers stem from the surface area of the respective *Aerosil*® parent.

The specific surface areas of the WO_3 precursors as determined by BET measurements are summarized in Table 7. The surface area after incipient-wetness impregnation is significantly lower than the specific surface area of the pure SiO_2 materials. This is due to the transport of the impregnation solution containing the soluble W-precursor into the pores of SiO_2 by capillary forces, leading to smaller pore volume and lower BET surface area after the synthesis. Nonetheless, the general trend remained the same as the surface area increased in the order of Bulk < AE90 < AE200 < AE380.

Table 7: Overview of the properties of the WO_3 based precursors.

WO_3 precursor	**W content [wt.-%]**	**BET surface area [m^2/g]**	**Crystalline domain sizes[1] [nm]**
WO_3 bulk	79	9	38.2 ± 0.3
AE90	48	34	21.1 ± 3.1
AE200	48	64	19.9 ± 0.8
AE380	51	97	17.3 ± 1.0

1 as determined from the FWHM of the XRD reflexes (23.6 °; 24.2°) using the Scherrer equation

The XRD patterns of the WO_3-based precursors are shown in Figure 17. All precursors show exclusively reflexes of monoclinic WO_3, which is the thermodynamically stable modification at room temperature.[156] However, significant reflex broadening for the SiO_2 supported precursors compared to WO_3 bulk can be observed. The crystalline domain sizes were determined using the Scherrer equation and are summarized in Table 7. It appears that a higher surface area of the SiO_2 support leads to smaller crystalline domain sizes of WO_3 and likely a higher WO_3 dispersion.

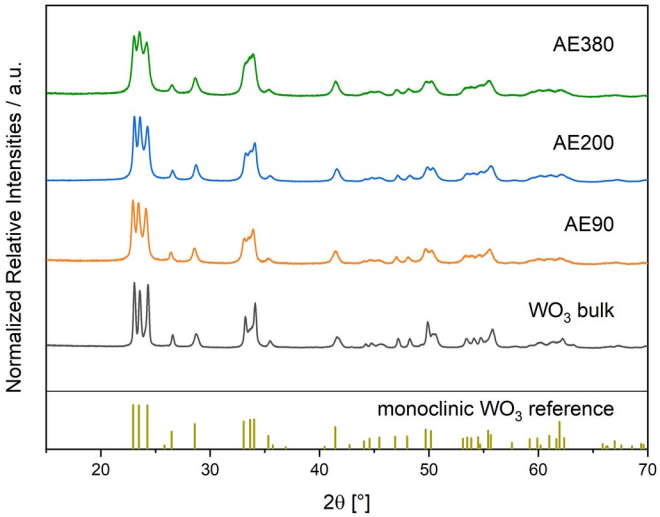

Figure 17: XRD patterns of the WO_3 precursors with a reference stick pattern of monoclinic WO_3 (ICSD-80056).

The diffuse UV/vis spectra of the WO_3 precursors are presented in Figure 18. The shape of the WO_3 band is significantly different depending on the precursor. It becomes generally broader with a lower surface area, and the broadest band is observed for bulk WO_3. In addition, the maximum of the band clearly shifts towards smaller wavelengths from Bulk > AE90 > AE200 ≈ AE200 < AE380. This "blueshift" is likely due to quantum-confinement effects and can be linked to decreasing WO_3 crystallite sizes in this order.[184],[185]

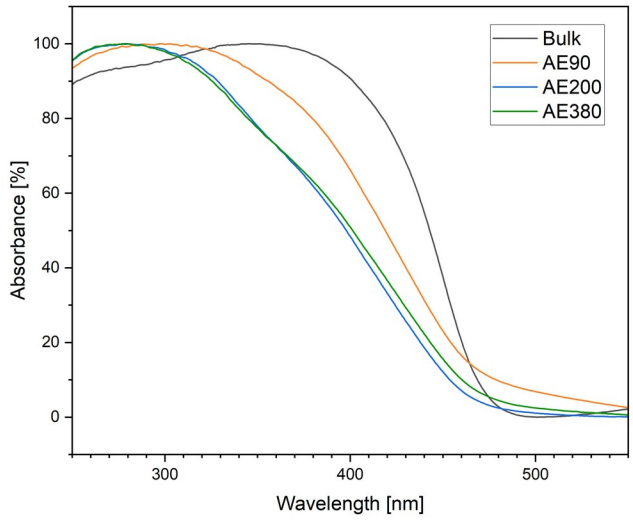

Figure 18: Diffuse UV/vis spectra of the WO_3 precursors.

The Raman spectra of all precursors show the vibrations of crystalline WO_3 with similar relative intensities (Figure 19). The vibrations at 806 cm^{-1}, 714 cm^{-1} can be assigned as O–W–O stretching modes, and the vibrations at approximately 327 cm^{-1} and 273 cm^{-1} can be assigned as O-W-O bending modes.[186] Terminal W=O vibrations, which would be around 900-1000 cm^{-1}, are not visible. This points to rather large WO_3 crystallite sizes in general, as the

intensity of W=O vibrations increases with smaller crystallites.[187] The Raman peaks of the SiO_2 supported precursors are noticeably broader than the ones of WO_3 bulk, likely due to smaller crystallites.[188] This is consistent with the observations from XRD and UV/vis, which indicate smaller crystallite sizes for the WO_3-SiO_2 precursors compared to WO_3 bulk. However, the SiO_2 supported precursors show no clear differences between each other in contrast to their XRD patterns and UV/vis spectra.

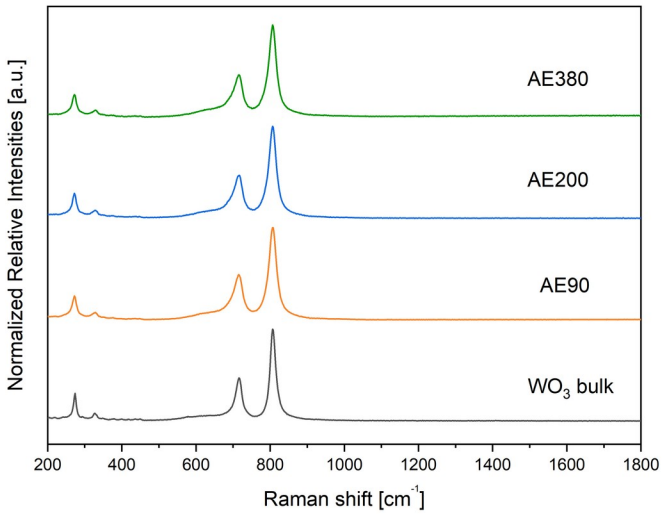

Figure 19: Raman spectra of the WO_3 precursors.

3.3 Products and mechanism of the reduction of tungsten oxide to tungsten metal

3.3.1 Phase evolution during reduction of WO_3

As the first step of the investigated tungsten carbide synthesis approach, reduction of the tungsten oxide precursors is carried out. This reduction step was therefore investigated isothermally at different reduction temperatures: 550 °C, 700 °C, and 800 °C (Scheme 13).

$$WO_3 + 3H_2 \xrightarrow[550\ °C\ /\ 700\ °C\ /\ 800\ °C]{} W + 3H_2O$$

Scheme 13: General reaction equation for the WO_3 reduction to W metal.

The reducibility of the WO_3 precursors was assessed by temperature-programmed hydrogen reduction measurements (Figure 20). The H_2-TPR profile of WO_3 bulk showed three overlapping main peaks at around 600 °C, 715 °C and 805 °C, which can likely be assigned to the stepwise reduction of W(+6) to W(0) (Scheme 14) as determined by *in situ* XRD

investigations using the same precursor (see section 2.2.1) and according to other literature sources:[189],[190]

$$WO_3 \longrightarrow W_{10}O_{29} \longrightarrow WO_2 \longrightarrow W$$

Scheme 14: Reaction sequence from WO_3 bulk reduction to W metal.

The reducibility of the precursors increases clearly with a higher WO_3 dispersion in the order Bulk < AE90 < AE200 < AE380, as the onset of WO_3 reduction shifts from around 500 °C for bulk WO_3 to 450 °C for AE380. Moreover, the three main reduction peaks became less defined for increased WO_3 dispersion, which can be explained by differences in the reduction mechanism, as also confirmed by the *in situ* XRD measurements in the following section. The determined reduction degrees were slightly higher than 100%, with around 5-13 % more hydrogen consumed than theoretically expected.

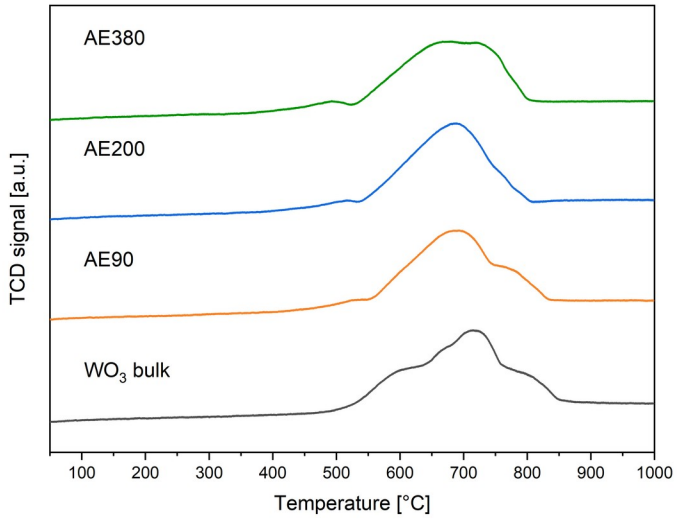

Figure 20: TPR profiles of the WO_3 precursors, recorded with 10 K/min heating rate, 50 ml/min gas flow, 5% H_2 in Ar and a sample weight corresponding to around 0.12 mmol W.

The isothermal reduction at 550 °C and 700 °C was investigated by *in situ* XRD for the system AE200. The *in situ* XRD investigations of the bulk system are described in section 2.2.1. The transformations of the XRD pattern of AE200 during reduction at 550 °C are shown in Figure 21. Interestingly, while heating up under inert gas flow to 550 °C, a tungsten bronze phase $H_{0.23}WO_3$ was formed even in the absence of H_2, which is a major difference to the bulk system. Hydrogen necessary for the conversion of WO_3 to $H_{0.23}WO_3$ might stem from water present in the crystal structure. As soon as hydrogen was introduced into the *in situ* cell, the tungsten bronze phase disappeared and a pure $W_{10}O_{29}$ phase was formed (10 min under H_2). After 20 min under H_2 flow, already the majority of $W_{10}O_{29}$ was converted into metallic β-W without WO_2 as an intermediate species. This conversion proceeded somewhat more slowly until no more reflexes of $W_{10}O_{29}$ were observed (50 min under H_2). After the reduction was complete,

hydrogen flow was continued until a total time of 180 min under H_2 flow. No clear further changes of the β-W pattern were observed, including no decrease of the FWHM, which would indicate sintering.

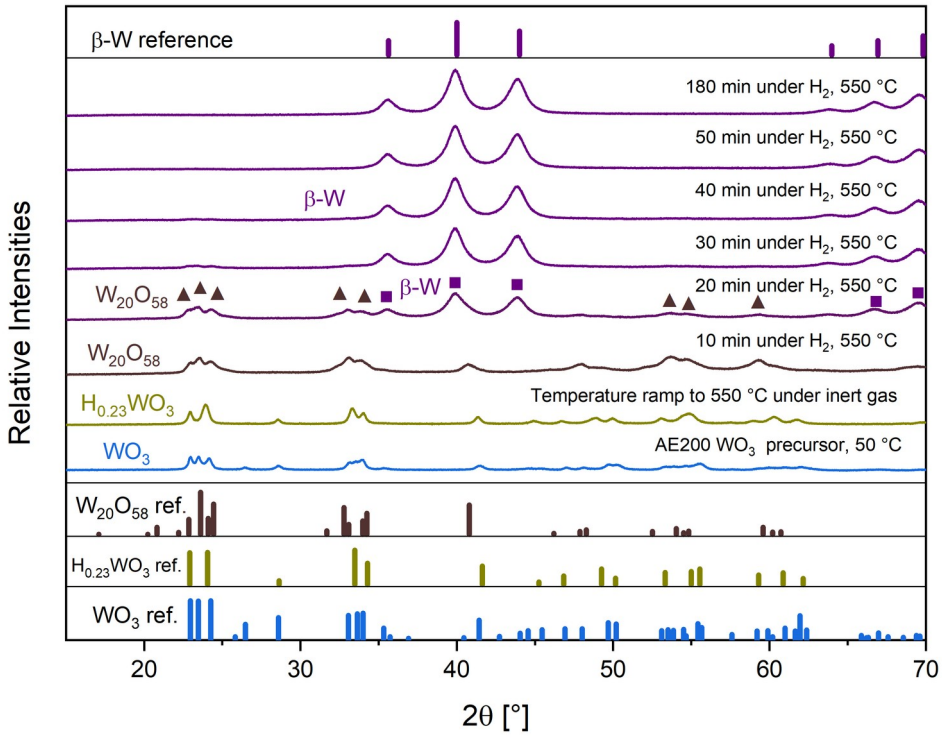

Figure 21: Evolution of the XRD patterns in the course of in situ isothermal hydrogen reduction of the AE200 precursor at 550 °C (70 mg AE200, 100 mL/min H_2 flow after heating up under inert gas). Stick patterns and selected markers were added for improved visual assignment. The reference patterns were sourced from the following database entries: WO_3: ICSD-80056. $H_{0.23}WO_3$: ICSD-8217. $W_{20}O_{58}$: ICSD-27705. Beta tungsten: ICSD-150496.

The transformations of the XRD pattern of AE200 during reduction at 700 °C are shown in Figure 22. The XRD pattern of the sample after heating to 700 °C under inert gas flow shows that partial reduction of WO_3 already took place even in the absence of H_2, as $W_{10}O_{29}$ was formed, likely due to thermal loss of oxygen. After hydrogen flow was initiated, further reduction of $W_{10}O_{29}$ to metallic tungsten proceeded very rapidly and was finished after 20 minutes. The product after complete reduction was a mixture of 40 wt.-% α-W and 60 wt.-% β-W as determined by Rietveld refinement. This is in contrast to the reduction product of bulk WO_3 under the same conditions, which was pure α-W, as described in section 2.2.1.

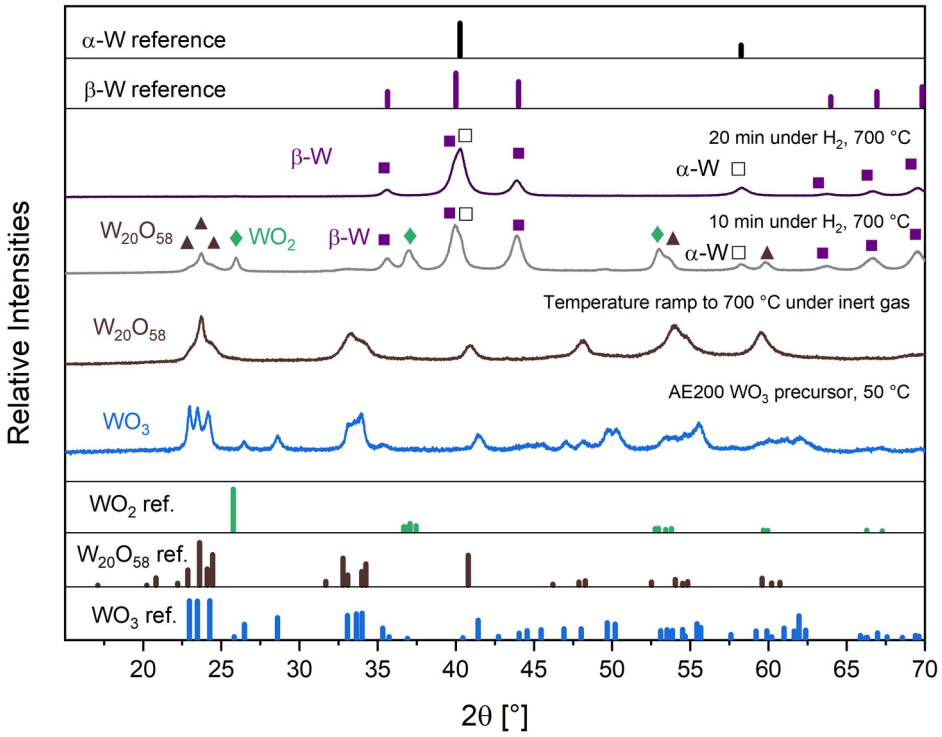

Figure 22: Evolution of the XRD patterns in the course of in situ isothermal hydrogen reduction of the AE200 precursor at 700 °C (70 mg AE200, 100 mL/min H_2 flow after heating up under inert gas). Stick patterns and selected markers were added for improved visual assignment. The reference patterns were sourced from the following database entries: WO_3: ICSD-80056. WO_2: ICSD-80829. $W_{20}O_{58}$: ICSD-27705. Beta tungsten: ICSD-150496. Alpha tungsten: ICSD-44393.

Summarizing the *in situ* XRD findings, the reduction process to metallic tungsten involves several steps and proceeds via intermediate tungsten oxide species. Comparing the reaction sequences at 550 °C and 700 °C shows that there are small differences. No intermediate WO_2 was detected for reduction at 550 °C, in contrast to reduction at 700 °C. Similar observations were also reported in the literature and are likely attributed to differing reaction pathways leading to the formation of α-W and β-W. With this in mind, the reaction sequence to β-W as indicated by the *in situ* measurements can be described as (Scheme 15):

$$WO_3 \longrightarrow H_{0.23}WO_3 \longrightarrow W_{20}O_{58} \longrightarrow \beta\text{-W}$$

Scheme 15: Reaction sequence from WO_3 reduction to beta- W

The reduction to α-W appears to follow the following reaction sequence (Scheme 16):

$$WO_3 \longrightarrow W_{10}O_{29} \longrightarrow WO_2 \longrightarrow \alpha\text{-W}$$

Scheme 16: Reaction sequence from WO_3 reduction to alpha W.

3.3.2 Characterization of the reduction products

The reduction step as part of the tungsten carbide catalyst synthesis was further investigated in the synthesis set-up. This was performed for the four investigated systems: Bulk, AE90, AE200, and AE380. As observed by XRD, reduction at 550 °C led to beta tungsten as the only product phase for all four investigated WO_3 precursors (Figure 23). This metastable modification of tungsten is significantly less studied in literature than the alpha phase of tungsten. The reduction temperature plays an important role for its formation, and it can become the favored reduction product at lower temperatures (below 600 °C).[153] However, other factors can also have an influence, including the content of water vapor in the reduction atmosphere or the state of the starting material. [159],[164],[166],[167],[168]

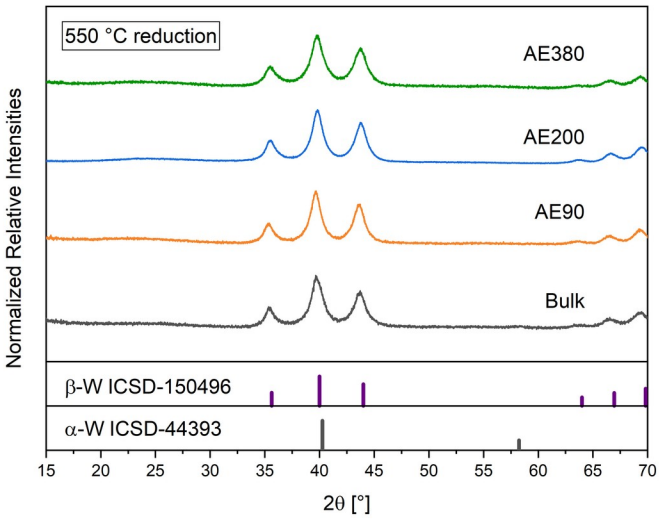

Figure 23: XRD patterns of the products from isothermal hydrogen reduction of the different WO_3 precursors at 550 °C in a horizontal high-temperature furnace.

Reduction at 700 °C resulted in significantly different product compositions depending on the WO_3 precursor (Figure 24). Pure alpha tungsten was the product phase of the bulk precursor, while the supported precursors resulted in mixtures of both alpha and beta tungsten. There was a clear correlation between the specific surface area of the precursor and the content of beta tungsten of the product. AE90 resulted in 32 wt.-% β-W, AE200 in 70 wt.-% β-W and AE380 in 88 wt.-% β-W. This indicates a critical role of the surface area in the formation of β-W, as the content of β-W increased with a higher surface area of the precursor.

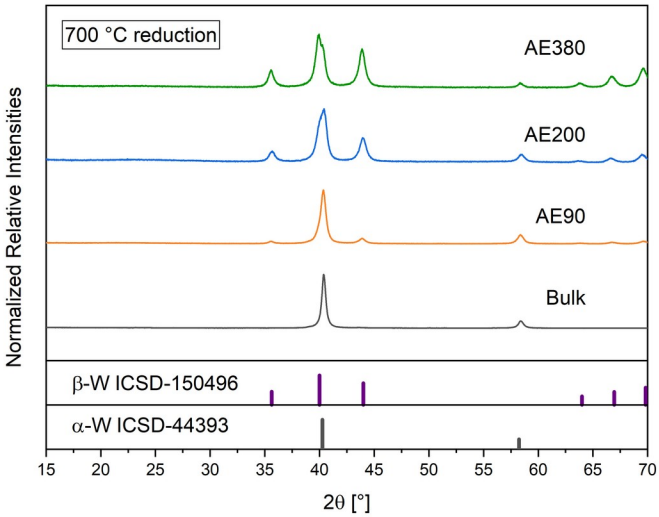

Figure 24: XRD patterns of the products from isothermal hydrogen reduction of the different WO_3 precursors at 700 °C in a horizontal high-temperature furnace.

Reduction at 800 °C (see Figure 25) led to pure alpha tungsten as the product phase for the bulk precursor and for AE90. For AE200 and AE380, a β-W content of 15 wt.-% and 31 wt.-% was determined for this precursor (Table 8). This demonstrates that even at this high temperature, the formation of β-W can play a role. Moreover, the precursors with higher surface area again led to a higher content of β-W. Figure 26 presents an overview of the β-W content depending on the reduction temperature and precursor.

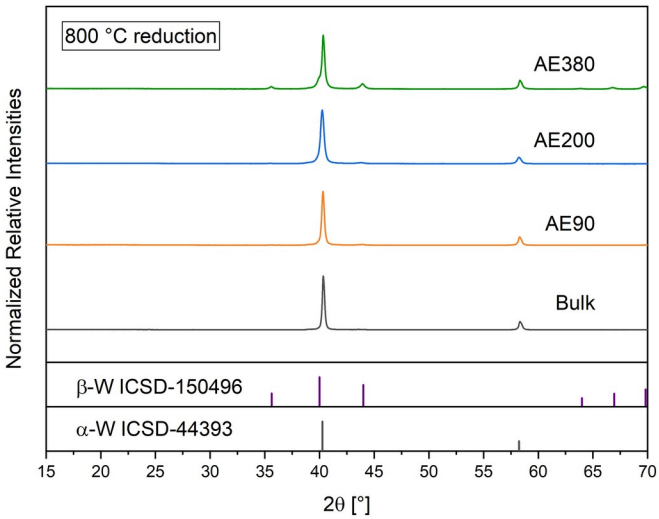

Figure 25: XRD patterns of the products from isothermal hydrogen reduction of the different WO_3 precursors at 800 °C in a horizontal high-temperature furnace.

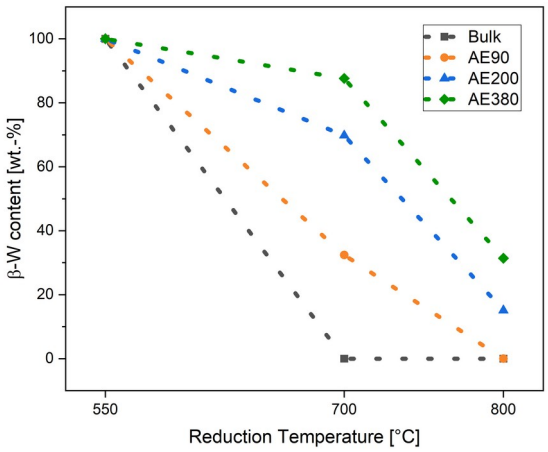

Figure 26: Content of beta tungsten determined by Rietveld depending on the WO_3 precursor and reduction temperature.

The BET surface areas of the products after reduction were measured and are summarized in Table 8. The surface area trends after reduction reflected those of the parent WO_3 precursors. At each reduction temperature, the lowest surface area was observed for the product derived from WO_3 bulk, while progressively higher surface areas were obtained from precursors with increasing initial surface areas in the order AE90, AE200 and AE380. For all precursors, the product surface areas decreased strongly with increased reduction temperature. This may be attributed to particle growth by volatile tungsten oxide species formed through the reaction of tungsten oxide with water. See also section 2.2.2. Sintering occurring before and during the reduction is also expected to contribute to the decline in surface area with higher temperatures (see section 2.2.2). The loss of surface area was more severe for the bulk system, while the SiO_2 supports appeared to stabilize the structure to some extent.

The crystalline domain sizes of the products showed similar (Table 8, Figure 27). A higher surface area of the corresponding WO_3 precursor mostly led to smaller crystalline domain sizes of the product. Consequently, the domain sizes decreased in the following order: Bulk, AE90, AE200, and AE380. As for the BET surface areas, the reduction temperature had a strong influence on the crystalline domain sizes. A significant increase in the domain sizes was observed with rising reduction temperatures, which also points to particle growth. Notably, the crystalline domain sizes of β-W were smaller than those of α-W for samples with both phases present.

Table 8: Overview of the properties of the products after reduction at different temperatures.

Reduction temperature	Precursor	β-W content [wt.-%]	α-W Crystalline domain size[1] [nm]	β -W Crystalline domain size[1] [nm]	BET surface area [m^2/g]
550 °C	*WO_3 bulk*	100	-	7.8 ± 0.3	19
550 °C	*AE90*	100	-	7.7 ± 0.3	70
550 °C	*AE200*	100	-	7.3 ± 0.4	90
550 °C	*AE380*	100	-	6.4 ± 0.1	149
700 °C	*WO_3 bulk*	0	20.9 ± 2.0	-	13
700 °C	*AE90*	32	14.9 ± 0.1	13.6 ± 0.7	53
700 °C	*AE200*	70	13.6 ± 0.2	13.0 ± 0.8	78
700 °C	*AE380*	88	15.4 ± 1.7	11	102
800 °C	*WO_3 bulk*	0	40.5 ± 3.0	-	4
800 °C	*AE90*	0	37.4 ± 1.7	-	42
800 °C	*AE200*	15	25.6 ± 0.6	13.1 ± 0.2	72
800 °C	*AE380*	31	28.2 ± 2.8	12	83

1 as determined by Rietveld analysis of the XRD patterns. Reference patterns: ICSD 44393 (α-W), ICSD 150496 (β-W).

2 as determined from the FWHM of the XRD reflexes using the Scherrer equation.

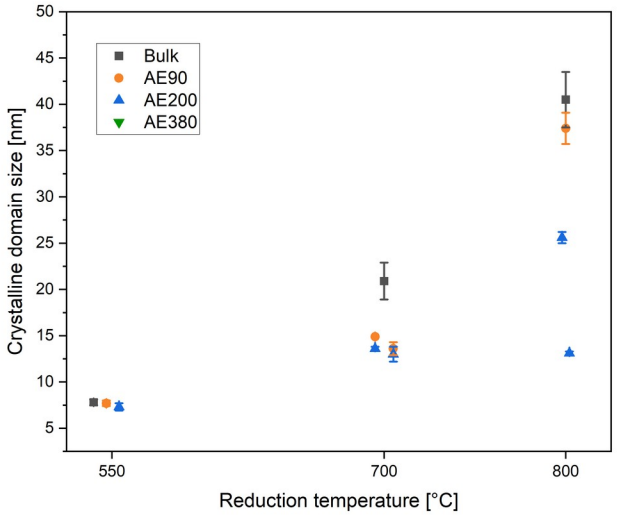

Figure 27: Crystalline domain sizes of the products of reduction depending on the reduction temperature and precursor.

3.4 Carburization of metallic alpha and beta tungsten

3.4.1 Phase evolution during carburization

As the second step of the tungsten carbide catalyst synthesis, carburization of the metallic tungsten precursors was investigated. The system AE200 was chosen as a representative example for insight into the transformation process of tungsten into tungsten carbide, *in situ* XRD measurements for these experiments. *In situ* XRD studies of the bulk system are described in section 2.3.2. Carburization at 550 °C was performed directly after the reduction of AE200 to metallic tungsten, which was discussed in section 3.3.1. Rapid conversion of the β-W phase was observed as the intensities of its reflexes gradually declined and the reflexes of W_2C emerged (Figure 28). After 60 min under a continuous flow of the carburization gas mixture, no more metallic tungsten was present in the XRD pattern of the material. The changes in the phase composition over time are visualized in Figure 29. The increase of W_2C proceeds in the shape of a sigmoidal curve, with slow conversion of β-W towards the start and end of carburization. No further changes of the XRD reflexes were determined after full reaction to W_2C, which demonstrates that the product was stable against reaction of W_2C to WC. Moreover, the crystalline domain sizes of the product over prolonged carburization time remained stable, indicating that no sintering of the material occurred after W_2C formation.

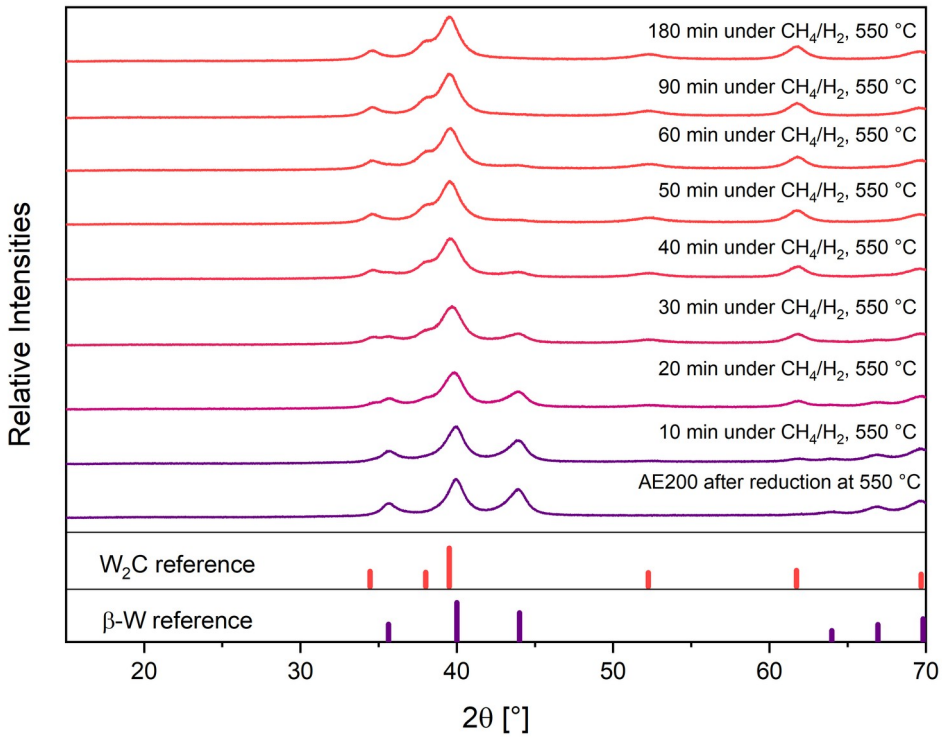

Figure 28: Evolution of the XRD patterns in the course of in situ isothermal carburization at 550 °C directly after isothermal reduction of the AE200 precursor at 550 °C. The carburization was performed using a 1.5:1 mixture of CH_4 and H_2 (100 mL/min). Stick patterns were added for improved visual assignment. The reference patterns were sourced from the following database entries: Beta tungsten: ICSD-150496. W_2C: ICSD-619097.

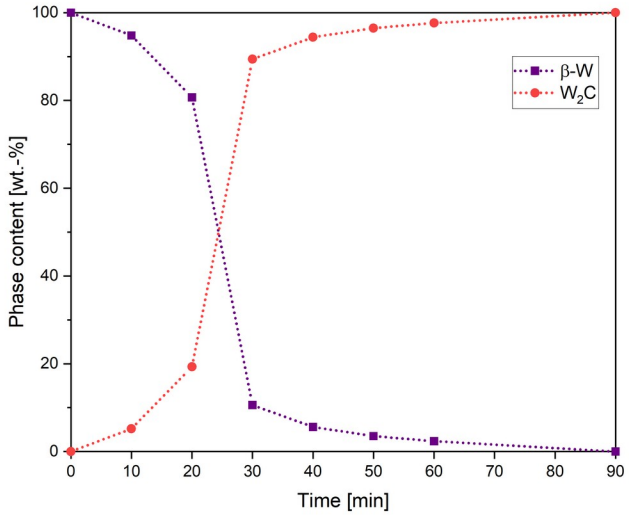

Figure 29: Change of the phase composition over time during in situ isothermal carburization at 550 °C of AE200, directly after isothermal reduction at 550 °C of AE200. The carburization was conducted using a 2:1 mixture of CH_4 and H_2, and a 100 mL/min total gas flow. The quantification was performed by Rietveld refinement using the following reference patterns Beta tungsten: ICSD-150496. W_2C: ICSD-619097.

Carburization of AE200 at 700 °C was investigated by *in situ* XRD as shown in Figure 30. Before this investigation, the WO_3 precursor was reduced at 700 °C in the *in situ* cell as described in section 3.3.1. A visualization of the changes regarding the phase composition is given in Figure 31. The conversion of both α-W and β-W to W_2C occurred very rapidly, with almost all metallic tungsten converted already after 10 min under the carburization atmosphere. However, further reaction of W_2C to WC proceeded considerably slower than the reaction of metallic W to W_2C. After 180 min under the carburization mixture, the material reached a stable state with no additional formation of WC. The product consisted of only a small amount of WC, while under the same conditions, a much larger WC content was observed (see 2.3.2).

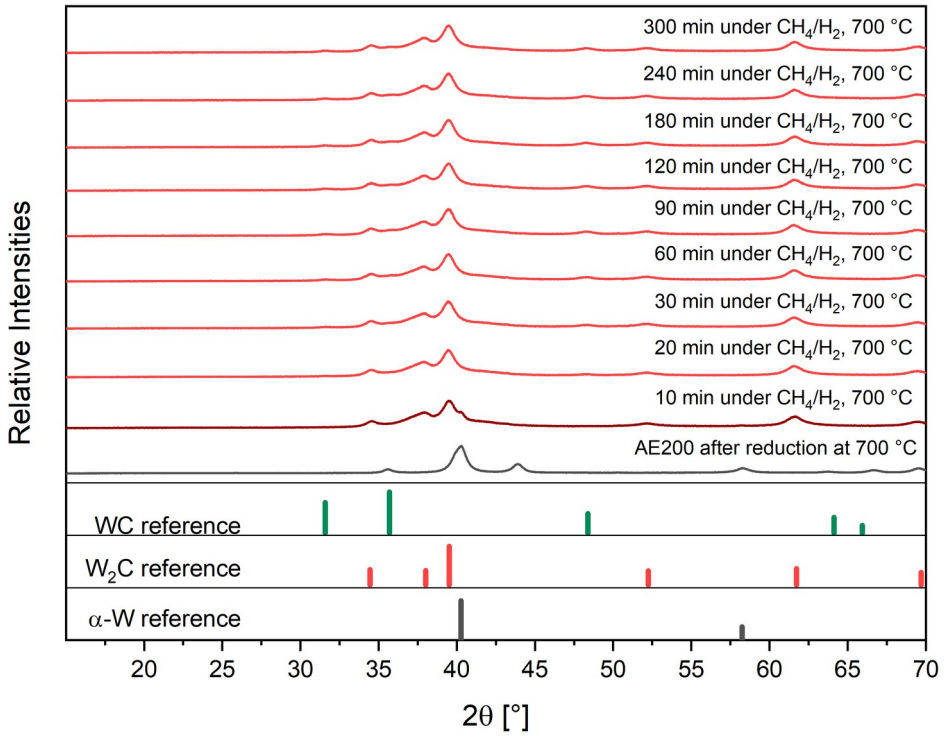

Figure 30: Evolution of the XRD patterns in the course of in situ isothermal carburization at 700 °C directly after isothermal reduction of the AE200 precursor at 700 °C. The carburization was performed using a 1.5:1 mixture of CH_4 and H_2. Stick patterns were added for improved visual assignment. The reference patterns were sourced from the following database entries: Beta tungsten: ICSD-150496. Alpha tungsten: ICSD-44393. W_2C: ICSD-619097. WC: ICSD-5212.

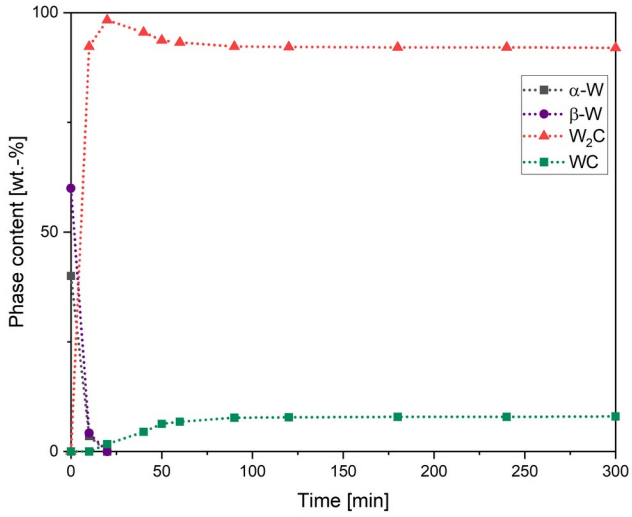

Figure 31: Change of the phase composition over time during in situ isothermal carburization at 700 °C of AE200, directly after isothermal reduction at 700 °C of AE200. The carburization was performed using a 4:1 mixture of H_2 and CH_4 and a 100 mL/min total gas flow. The quantification was conducted by Rietveld refinement using the following reference patterns: Alpha tungsten: ICSD-44393. W_2C: ICSD-619097. WC: ICSD-5212.

3.4.2 Characterization of the carburization products

The stepwise synthesis with reduction and carburization was applied for the synthesis of tungsten carbide catalysts. Carburization was carried out directly after the reduction step within the same catalyst synthesis setup. The carburization was performed at the same temperature as the preceding reduction, specifically at 550 °C, 700 °C, and 800 °C.

A fundamental understanding of the reaction conditions tungsten carbide synthesis at 550 °C using methane as the carbon source is essential for optimizing catalyst synthesis at this temperature. In that sense, the influence of the carburization time and the carburization gas mixture was investigated exemplarily for the system AE200. After the reduction of this WO_3 precursor at 550 °C under identical conditions, different carburization procedures were performed.

The XRD patterns of the products with carburization times of 0.5 h, 1.5 h, and 2.5 h are presented in Figure 32 (left side). As observed by *in situ* XRD measurements, the conversion of β-W to W_2C proceeded very rapidly. No more metallic tungsten was detected after only 0.5 h. Similarly to the *in situ* XRD investigation, no clear changes in the XRD reflexes over time were visible. The XRD patterns of the tungsten carbide catalysts prepared by different carburization gas compositions are depicted in Figure 32 (right side). Also in this case, the XRD patterns showed strong resemblance to each other, and no striking differences were visible.

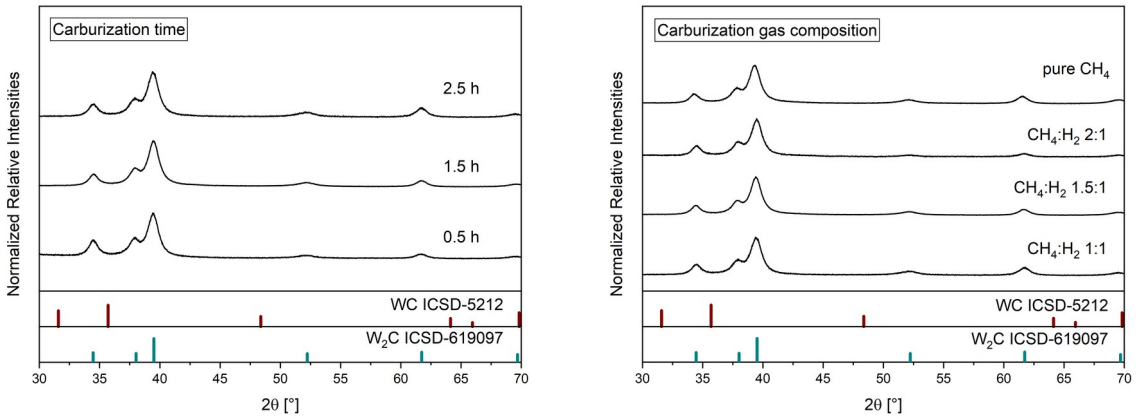

Figure 32: *XRD patterns of the products from stepwise synthesis of tungsten carbide via isothermal reduction and carburization of AE200 at 550 °C depending on the carburization time (left) and on the carburization gas composition (right).*

Influence of the precursor and carbide synthesis temperature on the catalyst structure

Tungsten carbide catalysts were prepared from the four different WO_3 precursors by sequential reduction and carburization at the same temperature. In order to investigate the influence of the synthesis temperature, carbide synthesis was performed at 550 °C, 700 °C, and 800 °C.

As observed by XRD, reduction and carburization at 550 °C led to phase-pure W_2C catalysts independent of the precursor (Figure 33). This situation was completely different for a

synthesis temperature of 700 °C. The phase composition of the product catalysts was determined by the precursor. Pure WC was the product phase of the bulk precursor, while the supported precursors resulted in mixtures of both W_2C and WC (Figure 34). There was a strong correlation between the specific surface area of the precursor and the W_2C content of the product. AE90 resulted in 33 wt.-% W_2C, AE200 in 55 wt.-% W_2C and AE380 in 60 wt.-% W_2C. This demonstrates that the surface area is an important factor for the stabilization of W_2C, as its content increased with a higher surface area of the precursor. Similar effects were observed for a synthesis temperature of 800 °C. Only small amounts of W_2C were present for AE380 with 7 wt.-% W_2C and AE200 with 5 wt.-% W_2C, whereas the other precursors led to pure WC as the product phase (Figure 35).

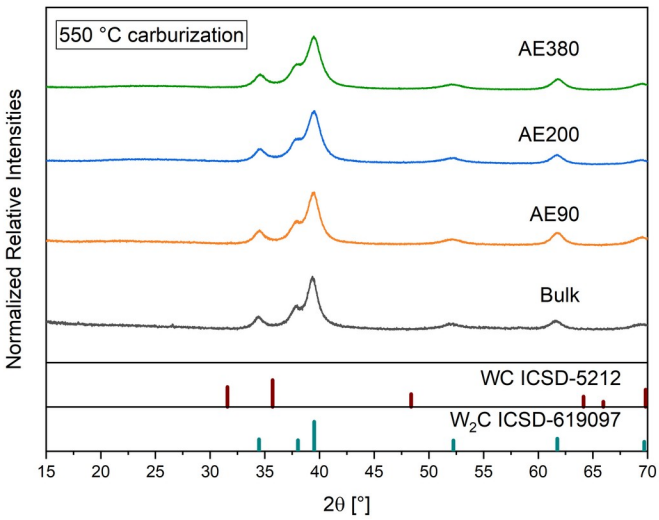

Figure 33: XRD patterns of the products from stepwise synthesis of tungsten carbide via isothermal reduction and carburization of the different WO_3 precursors at 550 °C

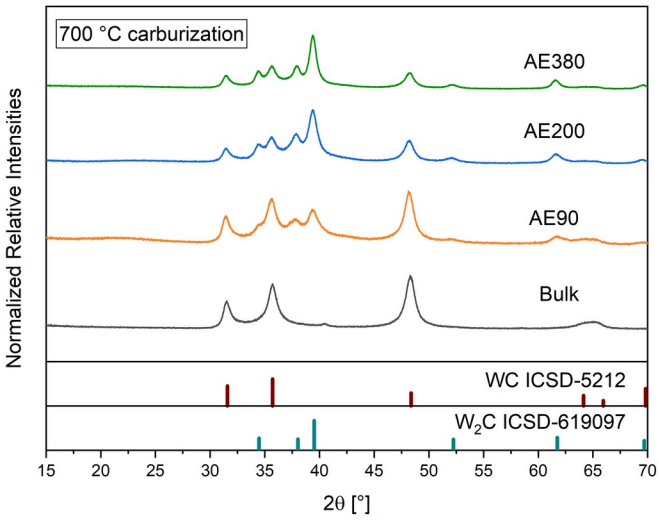

Figure 34: XRD patterns of the products from stepwise synthesis of tungsten carbide via isothermal reduction and carburization of the different WO_3 precursors at 700 °C

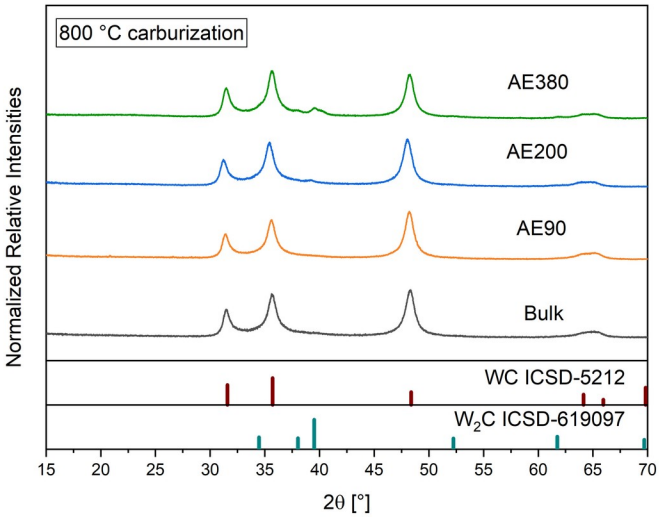

Figure 35: XRD patterns of the products from stepwise synthesis of tungsten carbide via isothermal reduction and carburization of the different WO_3 precursors at 800 °C

The BET surface areas of the products after reduction were measured and are summarized in Table 9. The surface area of the tungsten carbide catalysts increased in the same order as their WO_3 and W metal precursor counterparts: Bulk < AE90 < AE200 < AE380. Moreover, the surface areas were in general very close to their W metal precursors, however typically slightly lower.

The crystalline domain sizes of the tungsten carbide catalysts are also given in Table 9. Similar to the reduced W precursors, the crystalline domain sizes decreased in general in the order Bulk > AE90 > AE200 > AE380.

Regarding the influence of crystallite size on phase composition, a general increase in W_2C content is observed with decreasing crystallite size. This trend is more pronounced when considering the WC crystallite size (Figure 36) compared to that of W_2C (Figure 37).

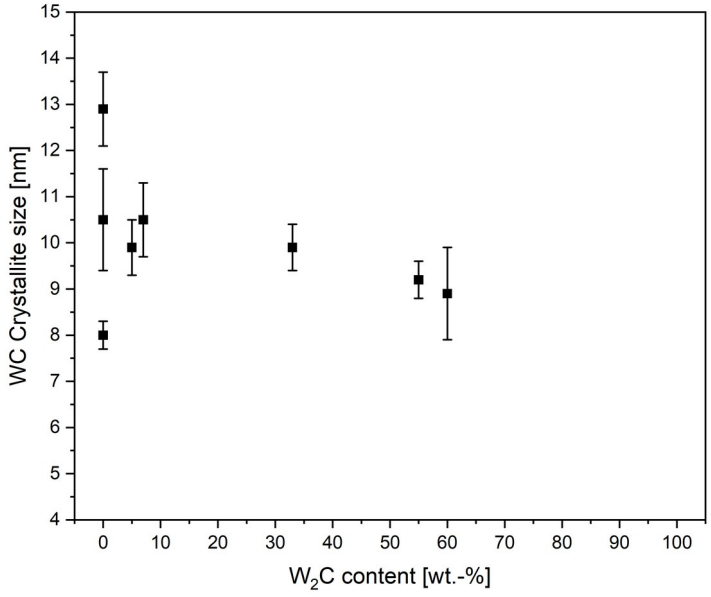

Figure 36: Influence of the WC crystallite sizes on the W_2C content.

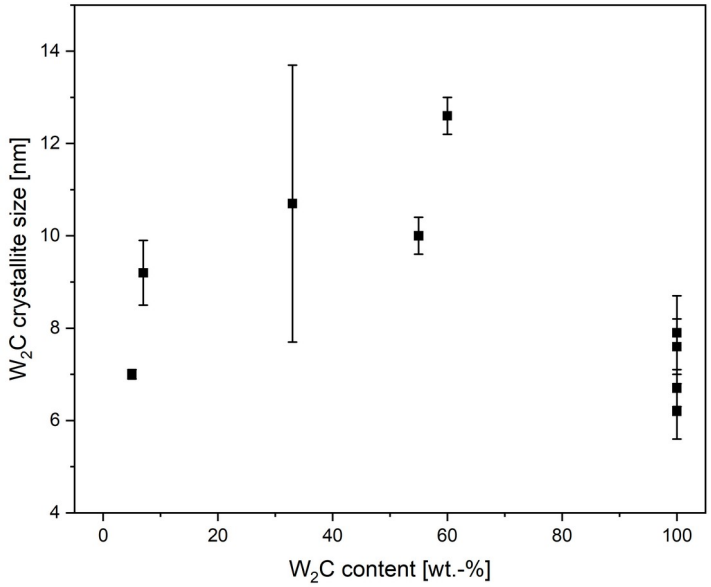

Figure 37: Influence of the W_2C crystallite sizes on the W_2C content.

TEM images of the AE200 catalysts prepared at 550 °C confirm that the primary particles are below 10 nm (Figure 38). However, statistical evaluation of the particle sizes was not possible due to the agglomeration and overlapping of the primary particles.

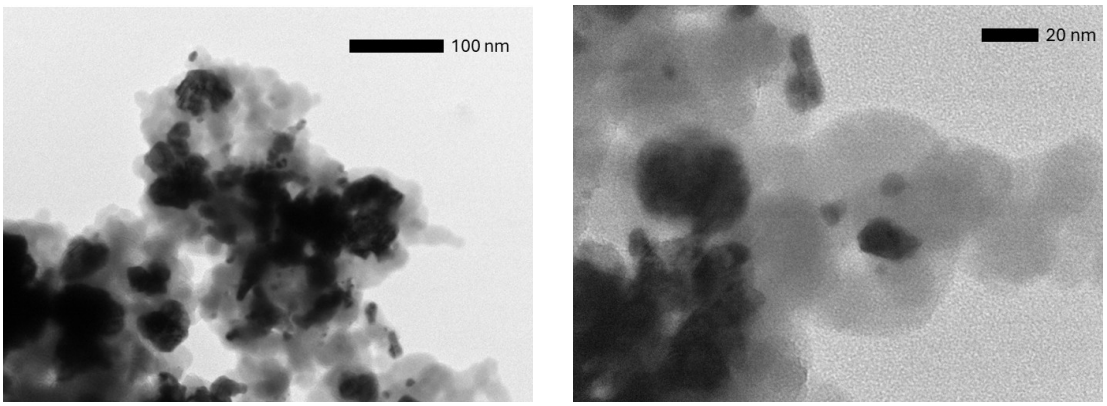

Figure 38*:* TEM images of the AE200 catalyst prepared by reduction and carburization at 550 °C.

In order to analyze the tungsten carbide surface of the catalysts, CO chemisorption measurements were performed. The determined CO uptakes are summarized in Table 9.
Figure 39 shows a general, though not entirely consistent, correlation between the W_2C content of the catalysts and their CO uptake. This confirms that the tungsten carbide dispersion of the catalysts plays an important role in the stability of the W_2C phase. However, the significance of the CO chemisorption measurements may be limited due to several complicating factors. In particular, the stoichiometry of CO adsorption on W_2C and WC surfaces remains uncertain, with conflicting information in the literature.[126],[172] It is also possible that the stoichiometry is different for W_2C and WC, and W_2C contributes significantly

more to CO adsorption than WC, which was assumed by Bretzler et al.[65] Moreover, it is important to note that the presence of carbon on the surface or within the pores can affect CO adsorption measurements, and to a lesser extent, BET surface area measurements. This might be the case for the catalysts prepared at 800 °C, where the formation of excess carbon is expected to be most relevant due to the higher temperature. Another factor is that transferring the catalyst to the chemisorption unit without air exposure was not feasible and the carbide synthesis was therefore carried out directly within the chemisorption setup using synthesis conditions as close as possible. However, it should be acknowledged that this approach may introduce variations in material properties, which are particularly related to the removal of excess carbon at the end of the synthesis.

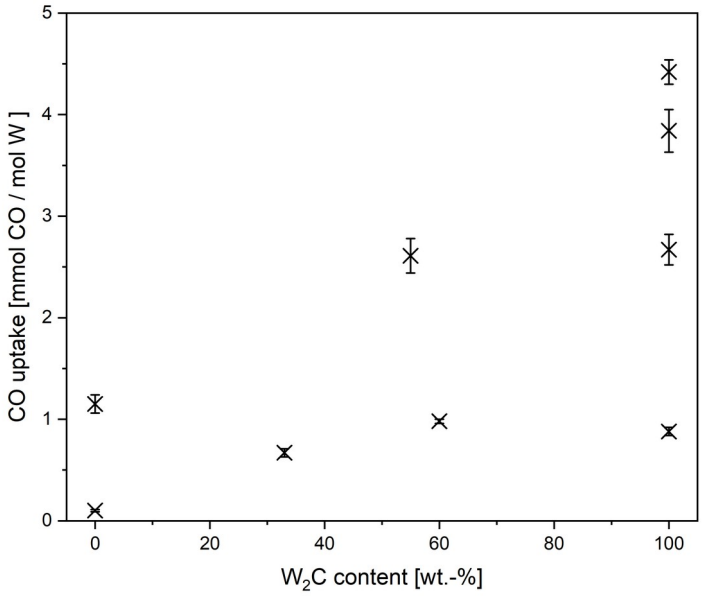

Figure 39: Influence of the W_2C content on the CO uptake of the catalysts.

Table 9*:* Overview of the properties of the products after carbide synthesis at different temperatures.

Carbide Synthesis temperature	Precursor	W_2C content[1] [wt.-%]	W_2C Crystallite size[2] [nm]	WC Crystallite size[2] [nm]	BET surface area [m^2/g]	CO uptake [$mmol_{CO}$ / mol_W]	1-Butanol formation rates [$mmol_{BuOH}$ / ($mmol_W$ h)]
550 °C	*WO_3 bulk*	100	7.9 ± 0.8		25	3.84± 0.21	18.7± 0.6
550 °C	*AE90*	100	7.6 ± 0.6		66	0.88 ± 0.04	24.5 ±0.6
550 °C	*AE200*	100	6.7 ± 0.4		87	4.42± 0.12	27.7 ± 1.1
550 °C	*AE380*	100	6.2 ± 0.6		141	2.67± 0.15	23.0 ±0.6
700 °C	*WO_3 bulk*	0		8.0 ± 0.3	20	1.15 ± 0.09	7.7 ±0.3
700 °C	*AE90*	33	10.7 ± 3.0	9.9 ± 0.5	50	0.67 ± 0.04	6.2 ±0.5
700 °C	*AE200*	55	10.0 ± 0.4	9.2± 0.4	73	2.61± 0.17	9.7± 0.3
700 °C	*AE380*	60	12.6 ± 0.4	8.9 ± 1.0	142	0.98± 0.02	6.2± 0.1
800 °C	*WO_3 bulk*	0		12.9± 0.8	20	0.10 ± 0.01	8.4 ±0.3
800 °C	*AE90*	0		10.5 ± 1.1	38	Not quantifiable	4.6± 0.1
800 °C	*AE200*	5	7.0 ± 0.1	9.9± 0.6	65	Not quantifiable	5.1± 0.3
800 °C	*AE380*	7	9.2± 0.7	10.5 ± 0.8	95	Not quantifiable	2.4± 0.1

1 as determined by Rietveld refinement.

2 as determined from the FWHM of the XRD reflexes using the Scherrer equation.

3.4.3 Discussion on the effects of surface area on the tungsten carbide phase composition

For both steps, reduction and carburization, two possible product phases can be obtained. In the case of reduction, this concerns the thermodynamically stable α-W and the metastable β-W modification. In analogy, carburization can afford the thermodynamically stable WC or the metastable W_2C modification. It is evident from the results of this study that two main factors drive the phase composition of the products for both synthesis steps: The reaction temperature and the surface area of the materials. Lower reaction temperatures help to kinetically stabilize the meta-stable phases β-W and W_2C, since further reaction to α-W or WC is prevented by an activation energy barrier.[191] Besides kinetic effects, contributions of the surface energy to the thermodynamic stability need to be taken into account. For comparison of the thermodynamic stability of phases, only the bulk energy is considered. However, this situation can be different for the surface energy, and a metastable phase with high bulk energy can have a low surface energy. When increasing the surface area of a material, the contributions of the surface energy become more relevant. At some point, a meta-stable phase with high bulk energy, but low surface energy, therefore becomes thermodynamically preferred.[176] This effect can be seen, for example, for TiO_2, as the anatase phase becomes the favored TiO_2 phase over rutile for particle sizes below approximately 14 nm.[177] Moreover, the metastable γ-Al_2O_3 phase becomes the thermodynamically preferred Al_2O_3 phase over α-Al_2O_3 when the specific surface area exceeds 125 m^2/g.[178] The same concept has also been proposed for tungsten carbide, based on theoretical calculations by Shrestha *et al.*[175] According to these results, hexagonal WC is the most stable tungsten carbide modification at particle sizes above 10 nm, while W_2C becomes the preferred phase for particle sizes below 10 nm. This behavior can be attributed to the surface energy characteristics of the respective phases, with hexagonal WC exhibiting a relatively high surface energy of 3.93 J/m², compared to lower values ranging from 2.28 to 2.83 J/m² for W_2C.[175] Supporting these theoretical insights, Bretzler *et al.* found experimentally that W_2C appeared to be preferred in crystallites smaller than 10 nm, whereas WC was predominantly formed in particles larger than 10 nm.[65]

This effect of the surface area on the phase composition is also clearly reflected in the present study. There is a decisive effect of the WO_3 precursor on both the content of β-W after the reduction step and on the W_2C content after the carburization step. Both phases are metastable under standard conditions; however, they exhibit lower surface energies than their counterparts. In the case of the two tungsten metal phases, bulk alpha tungsten is more stable than bulk beta-tungsten by 0.127 eV per atom from a thermodynamic perspective.[169] However, beta tungsten has a lower surface energy, < 3.5 J/m^2 vs ~ 4 J/m^2 of alpha-tungsten.[170] Smaller crystallite sizes should therefore be in favor of beta-tungsten as the stable phase.[171]

In the context of this study, using WO_3 precursors with different WO_3 dispersions provided clear experimental evidence for these relationships. With higher WO_3 dispersion, increased content of both β-W and W_2C was found in the products of reduction and carburization, respectively. This shows that the surface area plays a critical role in the phase selectivity in the synthesis of tungsten carbide.

3.5 Catalytic performance in hydrogenation reactions

3.5.1 Catalytic results

The products of the carbide syntheses were subsequently tested as heterogeneous catalysts in the hydrogenation of butyraldehyde to 1-butanol, which can serve as a model reaction for the assessment of the catalytic activity of tungsten carbide.[65] The reaction was performed in a liquid-phase batch process at 200 °C, 65 bar H_2 pressure, and with ethanol as solvent. Comparable product selectivity to 1-butanol of roughly 80% was observed for all catalysts. Deoxygenation reactions are expected to be the main contributors to incomplete carbon balance through the formation of butane and butene, which could not be determined by gas chromatography of the liquid phase.[56],[65] The catalytic performance was measured in the 1-butanol formation rate, normalized to the molar amount of W.

Figure 40 shows the influence of the carburization gas composition at a 550 °C carburization temperature on the catalytic activity. This investigation was carried out on system AE200, although the observed trends are likely representative of other systems as well. In the hydrogenation of butyraldehyde, the optimal gas composition at this temperature was found to be a CH_4:H_2 ratio of 1.5:1, yielding a 1-butanol formation rate of around 28.8 $mmol_{BuOH}/(mmol_W\ h)$. Using a CH_4:H_2 ratio of 2:1 led to a similar, but lower performance, with a 1-butanol formation rate of 27.7 $mmol_{BuOH}/(mmol_W\ h)$. Carburization using only methane and no hydrogen led to an inactive catalyst with no meaningful 1-butanol formation. On the other hand, using a 1:1 ratio also led to a significant drop in the catalytic activity to 21.8 $mmol_{BuOH}/(mmol_W\ h)$.

In order to further validate these findings, catalysts prepared under analogous conditions were investigated in the hydrogenation of toluene to methylcyclohexane (MCH), a well-established test reaction for transition metal carbides in the literature.[192],[193] The results for the system AE200 are presented in Figure 41 and reveal a similar relationship between the gas composition and the catalytic performance as in the case of the butyraldehyde hydrogenation. Carburization with only methane again produced an inactive catalyst, with negligible MCH formation. In contrast to the hydrogenation of butyraldehyde, the optimal performance in the hydrogenation of toluene was found to be a CH_4:H_2 ratio of 2:1 with 9.2 $mmol_{MCH}/(mmol_W\ h)$. However, the performance for a ratio of 1.5:1 was quite close with 9.0 $mmol_{MCH}/(mmol_W\ h)$. As

with the previous reaction, reducing the ratio to 1:1 led to a significant decline in catalytic performance to 7.1 $mmol_{MCH}/(mmol_W\ h)$. Therefore, the overall behavior is consistent with both hydrogenation reactions.

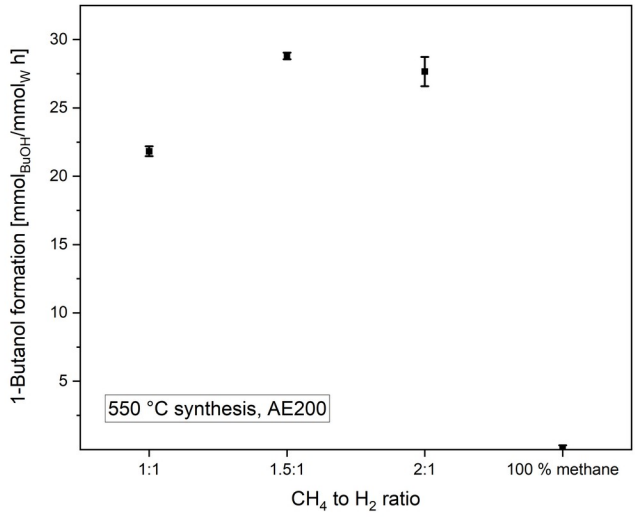

Figure 40: Influence of the carburization gas composition on the catalytic activity of AE200 for a carbide synthesis temperature of 550 °C. The catalytic tests were conducted at 200 °C, under a 65 bar H_2 atmosphere and with ethanol as solvent using 0.1 g of catalyst and 4 g of butyraldehyde, equivalent to a butyraldehyde-to-tungsten molar ratio of approximately 180.

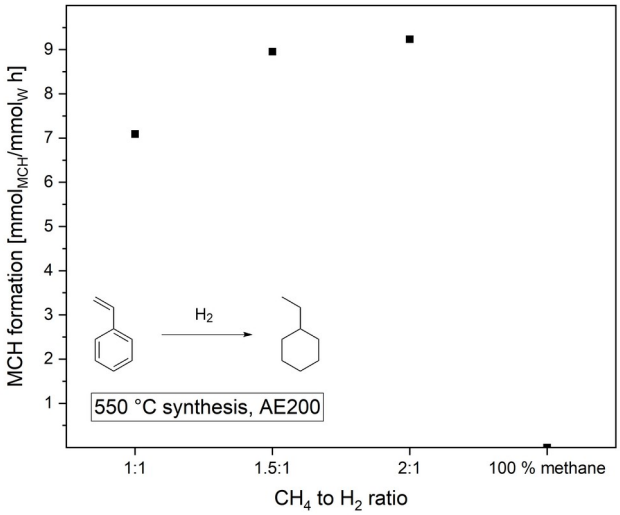

Figure 41: Influence of the carburization gas composition on the catalytic activity of AE200 for a carbide synthesis temperature of 550 °C. Catalytic hydrogenation of toluene was performed over 0.03 g catalyst at 230°C, 20 bar, continuous hydrogen flow, GHSV = 450,000 h^{-1}.

As another important aspect, the influence of the carburization time for carburization at a temperature of 550 °C was examined for the system AE200. As shown in Figure 42, the catalytic performance was improved drastically with longer carburization durations. Using a carburization time of 0.5 h afforded a 1-butanol formation rate of 6.6 $mmol_{BuOH}/(mmol_W\ h)$, while extending the time to 1.5 h increased the rate to 16.3 $mmol_{BuOH}/(mmol_W\ h)$. Increasing the carburization time further to 2.5 h resulted in a maximum rate of 27.7 $mmol_{BuOH}/(mmol_W\ h)$.

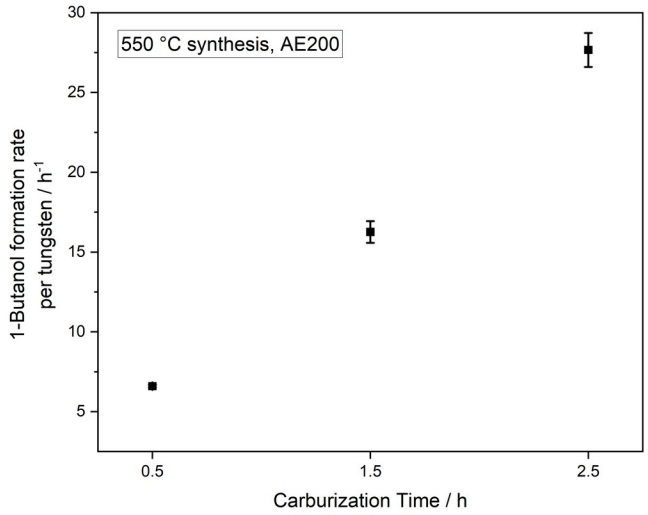

Figure 42: Influence of the carburization time on the catalytic activity of AE200 for a carbide synthesis temperature of 550 °C. The catalytic tests were conducted at 200 °C, under a 65 bar H_2 atmosphere and with ethanol as solvent using 0.1 g of catalyst and 4 g of butyraldehyde, equivalent to a butyraldehyde-to-tungsten molar ratio of approximately 180.

The catalytic performance of the tungsten carbide catalysts synthesized from different precursors and at different temperatures is shown in Figure 43. The highest catalytic activity was observed at a synthesis temperature of 550 °C, with a significant decline at higher temperatures. Interestingly, the performance ranking of the precursors was different for each synthesis temperature. For a synthesis temperature of 550 °C, the highest performance was observed for AE200 with 27.7 $mmol_{BuOH}/(mmol_W\ h)$, followed by AE90 (24.5 $mmol_{BuOH}/(mmol_W\ h)$), AE380 (23.0 $mmol_{BuOH}/(mmol_W\ h)$), and finally the bulk catalyst, which showed the lowest butanol formation rate with 18.7 $mmol_{BuOH}/(mmol_W\ h)$. For a synthesis temperature of 700 °C, this order was AE200 > Bulk > AE90 ≈ AE380, while for 800 °C, the bulk catalyst outperformed the supported catalysts, and the ranking shifted to Bulk > AE200 > AE90 > AE380.

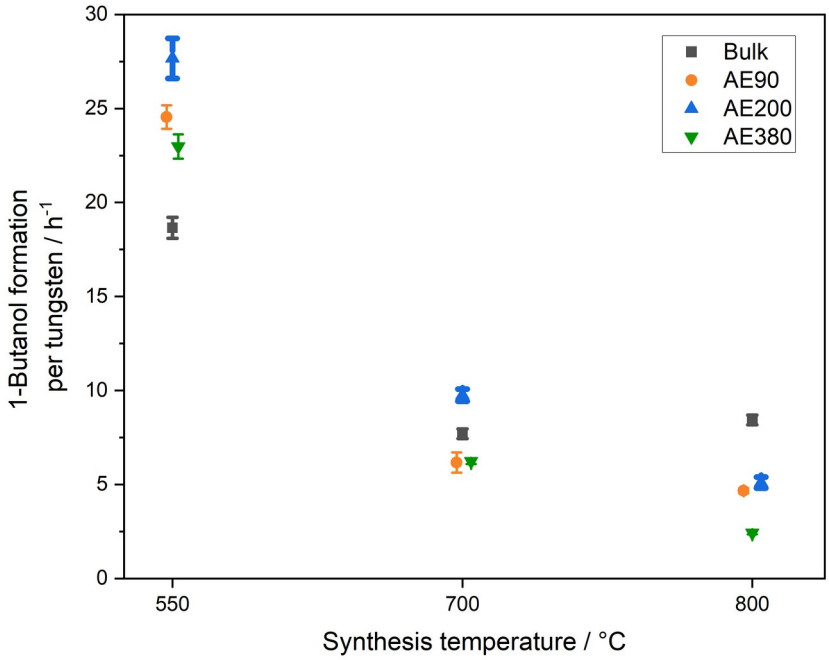

Figure 43: 1-Butanol formation normalized to the tungsten content for tungsten carbide catalysts prepared from different precursors. The catalytic tests were conducted at 200 °C, under a 65 bar H_2 atmosphere and with ethanol as solvent using 0.1 g of catalyst and 4 g of butyraldehyde, equivalent to a butyraldehyde-to-tungsten molar ratio of approximately 180.

Considering the phase composition of the catalysts, there is a general, although not simple, correlation between the W_2C content and the 1-butanol formation rate (Figure 44). In particular, catalysts at the two extreme ends of the spectrum with 100% and 0% W_2C exhibit catalytic activities clearly distinct from each other. The performance of pure W_2C catalysts exceeded that of pure or close to pure WC catalysts by factors ranging from 2 to 5, and in some cases, reaching up to 10.

Similarly, the 1-butanol formation rate exhibits an inverse correlation with the crystallite size of the catalysts (see Figure 45 and Figure 46). For both tungsten carbide phases, W_2C and WC, the formation rate generally decreased as crystallite size increased. It should be noted that crystallite size and phase composition are interrelated (see 3.4.2 and 3.4.3), which complicates the isolated assessment of their individual effects on catalytic performance.

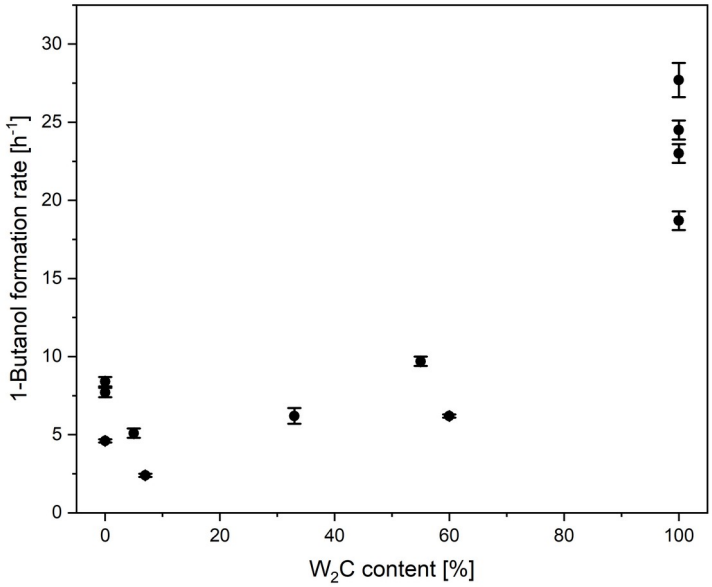

Figure 44: Influence of the W_2C content on the 1-butanol formation rate.

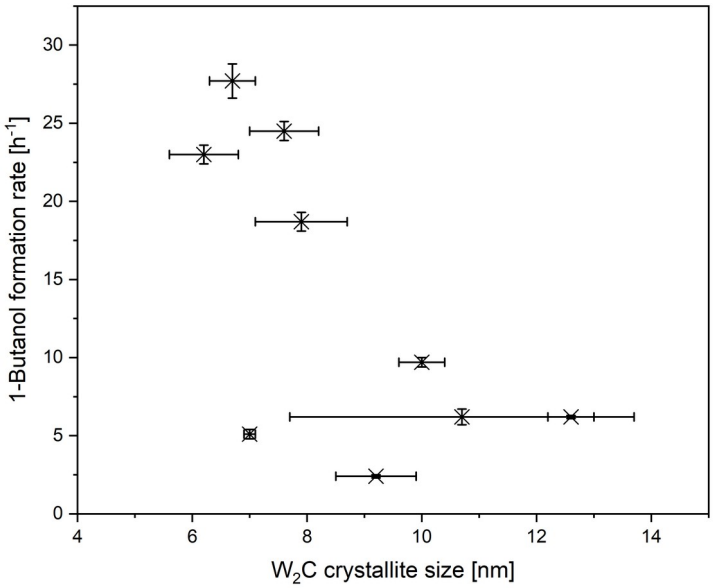

Figure 45: Influence of the W_2C crystallite size on the 1-butanol formation rate.

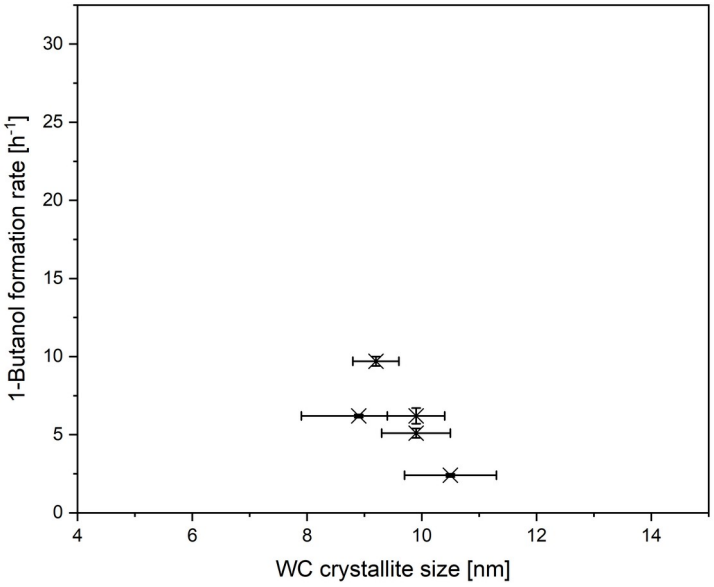

Figure 46: Influence of the WC crystallite size on the 1-butanol formation rate.

3.5.2 Discussion on the influence of the carburization conditions

For tungsten carbide synthesis at 550 °C, a strong influence of the carburization time and carburization gas mixture on the catalytic performance was observed. However, the differences in the catalytic activity are in this case not related to significant differences in the XRD. For a better understanding of this discrepancy, it is important to consider the underlying mechanisms regarding the structural transformation during carburization.

While complete conversion of tungsten metal to W_2C would be expected from the XRD data, even after only 0.5 h carburization, the 1-butanol formation rate is almost one order of magnitude lower than the catalyst produced by 2.5 h carburization. It appears reasonable that further processes occur after the rearrangement of the W atoms. Through the combination of carbon and tungsten orbitals during carbide formation, the s-p electron count is increased, which, in the sense of the Engel-Brewer theory, causes a transformation of the crystal structure. [194],[195],[196] This transition of a cubic W lattice to a hexagonal one is responsible for changes in the XRD patterns. On the other hand, changes in the arrangement of carbon are mostly negligible for XRD analysis.[99]

It might be the case that the transformation of the tungsten metal lattice to the W_2C lattice already starts rather early at a lower carbon content than necessary for full stoichiometric conversion to W_2C. The decrease in catalytic activity with shorter carburization times may be attributed to carbon deficiency in the tungsten carbide due to incomplete formation of W_2C. In fact, literature studies indicate that transition metal carbides are strongly nonstoichiometric compounds.[197] Carbon atoms are located in the interstitial spaces of the metal sublattice and

form a non-metal sublattice.[96] Also, structural vacancies are present, which are unoccupied interstitial sites.[198] The concentration and distribution of these can differ to some extent. It was reported that W_2C has a homogeneity region from $WC_{0.34}$ to $WC_{0.52}$ at a temperature of about 3000 K, even though this range narrows at lower temperatures.[96],[198] With this in mind, it is conceivable that the carbon content is somewhat lower at the beginning of the carburization and approaches the stoichiometry of W_2C with longer carburization duration. This could show that the catalytic properties of tungsten carbide are possibly very sensitive to the carbon content in the lattice.

The carburization gas composition is another key parameter in the synthesis of the tungsten carbide catalysts at 550 °C, which can strongly affect the catalytic performance. In addition to methane as a carbon source, hydrogen is added to the carburization mixture. The presence of hydrogen plays an important role in controlling the amount of carbon deposited on the tungsten surface. CH_4 is decomposed into deposited carbon or adsorbed CH_x species and hydrogen (Scheme 17).[121]

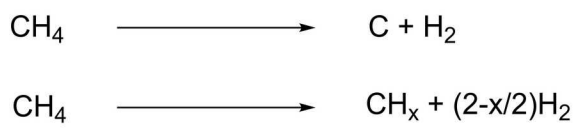

Scheme 17: Reaction equations of CH_4 decomposition on the W-metal surface during carbide synthesis.[121]

If the subsequent migration of carbon from the surface of W into the bulk is significantly slower than the decomposition of CH_4, carbon can build up on the surface.[110] In the context of catalysis, this is an undesirable effect as it can block the tungsten carbide surface sites.[172] Hydrogen helps to balance the amount of carbon on the surface by impeding the adsorption of CH_4 and by reacting with adsorbed carbon to CH_4.[119]

As shown in Figure 40 and Figure 41, adjusting the ratio of CH_4 and H_2 in the carburization atmosphere is critical. It can be concluded that the optimum catalytic performance can be reached by applying CH_4 to H_2 ratios of 2:1 and 1.5:1. When increasing or decreasing this range, the catalytic activity decreased significantly. It is plausible that a higher content of hydrogen causes a lower concentration of deposited carbon on the tungsten surface. This, in turn, could lead to a carbon deficiency in the W_2C products. This explanation would be in line with the previous assumption that the carbon content in W_2C might deviate depending on the synthesis conditions. This also indicates a high sensitivity of the catalytic activity on the stoichiometric composition of W_2C.

On the contrary, a high concentration of CH_4 leads to a higher concentration of deposited carbon on the surface, which, over time, forms carbon aggregates. The latter might not be fully removed during the hydrogen treatment at the end of the carburization period and block the active sites of the tungsten carbide catalysts. This is particularly noticeable in the case of pure

methane, as the buildup of carbon is the strongest due to the highest surface concentration of carbon and due to the absence of hydrogen, which would counteract carbon accumulation. This leads to almost inactive catalysts both in toluene and butyraldehyde hydrogenation.
These results also demonstrate that the optimum CH_4 to H_2 ratio is different depending on the carburization temperature, as a CH_4 to H_2 ratio of 1:4 is typically applied for carbide synthesis at 700-800 °C.[65] Lower carburization temperatures, therefore, require a higher CH_4 concentration, which may be explained by the kinetics of CH_4 activation declining faster than the kinetics of H_2 activation with decreasing temperature.

3.5.3 Discussion on the influence of the precursor on the catalytic activity

The catalytic activity of the tungsten carbide catalysts was strongly affected by the precursor; however, the relative performance for the precursors varied with synthesis temperature. This highly complex situation is caused by multiple factors that have an impact on the catalytic performance. As it is typical for heterogeneous catalysis, the tungsten carbide dispersion plays an important role as it equates to the number of active surface sites available for catalysis. This is clearly the dominating factor for carbide synthesis at 550 °C, as the order of catalytic performance follows in principle the order of tungsten carbide dispersion as suggested by the crystalline domain sizes. The only exception in this case is AE380, which would be expected to result in the highest catalytic activity due to the smallest crystalline domain sizes. Besides dispersion, the phase composition of the catalysts has been shown to play a role in the catalytic activity. As shown in Chapter 2, Bulk tungsten catalysts with pure W_2C and WC phases showed clear differences in the catalytic hydrogenation of butyraldehyde to 1-butanol, with higher catalytic activity of W_2C compared to WC. In addition, Bretzler *et al.* observed a strong correlation of the catalytic activity and the W_2C content in hydrogenation reactions.[65] Higher performance of W_2C over WC was also observed in the hydrogen evolution reaction (HER) over tungsten carbide electrocatalysts.[143],[183] Theoretical investigations of Gong *et al.* explained the distinct catalytic performances of the tungsten carbide phases by different electronic properties, as the electronic density of states (DOS) near the Fermi level was found to be higher for W_2C than for WC.[143] Similarly, Suetin *et al.* reported a stronger metallic character of W_2C than WC according to calculations.[97]
The effect of the phase composition can also be seen in this study, as the catalysts with pure W_2C (550 °C synthesis temperature) performed significantly better than their counterparts with pure WC or mixtures of W_2C and WC. However, no clear correlation was observed between phase composition and catalytic performance for the catalysts synthesized at 700 °C and 800 °C. For example, the AE380 catalyst showed the highest W_2C content at 700 °C (60 wt.-%) yet exhibited one of the lowest 1-butanol formation rates. Similarly, at 800 °C, the bulk catalyst displayed the highest activity despite its low dispersion and pure WC phase composition. It is

plausible that this discrepancy can be attributed to another important aspect for the catalytic activity, which is the presence of carbon deposits on the catalyst surface, as discussed in 3.5.2. It appears that precursors with higher tungsten dispersion might be more reactive towards carburization. Due to the enhanced rate of CH_4 decomposition, more carbon is formed at the surface. In addition, systems with high dispersion stabilize the initially formed W_2C phase against further carbon insertion into the lattice and therefore more carbon remains at the surface. This might cause the low performance of highly dispersed W_2C catalysts (AE200, AE380) synthesized at 700 °C and 800 °C.

3.6 Conclusion

Tungsten carbide catalysts with different dispersions were synthesized from WO_3 precursors using a two-step approach with separated reduction and carburization. Both synthesis steps, reduction and carburization, were studied in-depth by various characterization methods. The properties of the tungsten metal and tungsten carbide products were strongly determined by the temperature and the structure of the WO_3 precursors. Investigation of the reduction revealed that higher precursor surface areas favor the formation of metastable β-W over thermodynamically stable α-W, as well as low reduction temperatures. Similarly, the carburization step showed that lower synthesis temperatures and higher precursor surface areas stabilize the metastable W_2C phase, which exhibits superior catalytic activity compared to WC. This shows that both metastable phases can be stabilized thermodynamically due to surface energy contributions.

Catalytic tests in hydrogenation reactions, such as butyraldehyde to 1-butanol, revealed superior performance for tungsten carbide synthesis at 550 °C due to increased tungsten carbide dispersion and due to the selective synthesis of W_2C as the more active tungsten carbide phase. The optimal carburization conditions at 550 °C were identified as a CH_4:H_2 ratio of 1.5:1 or 2:1, which balances carbon deposition and prevents blockage of the active sites. Longer carburization times further enhanced catalytic activity, likely due to improved stoichiometric carbon incorporation into the W_2C lattice.

Catalyst synthesis at 700 °C and 800 °C was found to be strongly detrimental for catalysts with high tungsten carbide dispersion, due to excessive carbon deposition.

Overall, this study provides detailed insights into the synthesis-structure-performance relationships of tungsten carbide catalysts. It can be seen that the alternative synthesis approach with separated reduction and carburization is highly beneficial for optimizing the catalytic efficiency, as it enables low temperature synthesis of tungsten carbide catalysts.

3.7 Disclaimer

This chapter (chapter 3 and associated experimental descriptions in chapter 6) is based on a manuscript, which is not yet submitted, with the anticipated title: “The decisive role of the dispersion on the phase composition (W_2C and WC) of supported tungsten carbides as hydrogenation catalysts”. The author of this dissertation (Patrick Schlachta) is also the first author of the manuscript. The contributions of Patrick Schlachta to the manuscript in the sense of the CRediT author statement definitions include conceptualization, investigation, methodology, validation, formal analysis, visualization and writing (original draft and editing). The content has been edited and restructured to some extent, to align with the format and context of this dissertation. All co-authors, that is Rolf E. Jentoft, Elena Willinger, Friederike C. Jentoft and Klaus Köhler have approved the use of the manuscript in this dissertation. The article is intended to be published as open access and is reused here for the purpose of this dissertation in accordance with the Creative Commons Attribution 4.0 International License (CC BY, see https://creativecommons.org/licenses/by/4.0/), which allows unrestricted reuse of the work in any medium or format, as long as appropriate credit is given to the original work.

4

Reduction of N_2O by H_2

4.1 Introduction

4.1.1 Catalytic reduction of nitrous oxide (N_2O) by hydrogen

In addition to producing value-added chemicals, heterogeneous catalysts play a crucial role in removing undesirable compounds from exhaust streams. In this context, catalytic hydrogen activation can also be a relevant approach as described in section 1.3. One compound of growing concern is nitrous oxide (N_2O), which is a strong greenhouse gas with an estimated global warming potential of about 300 times greater than that of CO_2.[70] In addition, N_2O exhibits potent ozone-depleting properties and is now even the leading cause of this atmospheric degradation.[71] Anthropogenic N_2O emissions could nearly double between 2005 and 2050 under business-as-usual scenarios.[199] While the large majority of anthropogenic N_2O emissions come from agriculture, technical processes are also important sources for N_2O emissions.[200] This includes industrial plants such as for the production of nitric acid or adipic acid (the main intermediate in nylon 6,6 production), as well as combustion processes of energy sources.[201],[202],[203] In these cases, exhaust gas catalysis plays a crucial role in lowering N_2O emissions. Furthermore, it is expected that the use of ammonia will play an increasingly important role in the coming decades as an alternative energy carrier to fossil fuels in maritime shipping.[204] This further underscores the continued relevance of exhaust gas catalysis as a key technology, as ammonia combustion also generates N_2O as a by-product, along with other nitrogen oxides.[205],[206] The use of hydrogen for the selective catalytic reduction (SCR) of nitrogen oxides is a promising approach in this regard, offering high catalytic performance and environmentally friendly products in the form of water and nitrogen.[81] While the selective catalytic reduction of NO with hydrogen has been extensively studied in the literature,[81] the corresponding reduction of N_2O has received much less attention. Roy *et al*. investigated H_2-SCR of N_2O over noble metal substituted TiO_2 catalysts and reported high N_2O conversion in the 50-120 °C temperature range for $Ti_{99}Pd_{0.01}O_x$, $Ti_{99}Rh_{0.01}O_x$, and $Ti_{99}Pt_{0.01}O_x$ with a GHSV of 43,000 h^{-1}.[207] In the case of Ru substituted TiO_2, on the other hand, temperatures of more than 250 °C were necessary for full N_2O conversion. The authors proposed a bi-functional reaction mechanism with N_2O adsorption and dissociation on oxide vacancies, while hydrogen activation takes place at the noble metal sites. While this mechanism is plausible for the special case of solid-solution type catalysts, a different kind of mechanism can be assumed for the more typical case of supported metal catalysts. Studies on H_2-SCR of N_2O over the Ir(110) surface by Carabineiro and Nieuwenhuys revealed a reaction pathway involving catalytic decomposition of N_2O into N_2 and adsorbed oxygen, followed by hydrogen dissociation and a subsequent surface reaction forming water (more details in 4.5.1).[208] Burch *et al.* suggested that thermally non-equilibrated oxygen, so-called “hot-oxygen”, plays a role in the reaction mechanism of H_2-SCR of N_2O, see also 4.5.1.[209]

It is generally assumed that the energy resulting from a bond scission is dissipated immediately over the catalyst surface and therefore does not influence the kinetics of subsequent reaction steps.[210] This model has been increasingly questioned in the literature, especially theoretical works predict a more complex situation.[210],[211],[212] The extremely high exothermicity of H_2-SCR of N_2O with a ΔH of -323.3 kJ/mol (at 298 K) makes this reaction, therefore, a highly interesting model reaction for further investigation of this fundamental research interest.
Also, due to the high cost and rarity of noble metals, it is crucial to better understand how the catalytic efficiency can be maximized for potential industrial applications of H_2-SCR of N_2O. This chapter, therefore, intends to provide further insight into structure-activity relationships of the catalysts, as described in the next section (4.1.2).

4.1.2 Aim and Motivation

This chapter explores the use of hydrogen for the selective catalytic reduction of N_2O. Given the limited research to date on the catalytic reaction between N_2O and H_2, an improved understanding of general and fundamental aspects is intended. Quasi *in situ* X-ray Photoelectron Spectroscopy (XPS) measurements are performed in order to gain insight into the catalyst behavior during catalytic reduction of N_2O by H_2. In order to evaluate the effectiveness of different hydrogen activating noble metals, Rh, Pd, and Ru catalysts supported on Al_2O_3 and CeO_2 are compared. Moreover, the influence of various relevant structural properties of the catalyst on the catalytic performance in the reduction of N_2O by H_2 shall be systematically analyzed. This includes the effects of noble metal dispersion, synthesis method, type of noble metal precursor, promoter addition, and choice of catalyst support. For this purpose, Pd catalysts are prepared using different synthesis specifications. These catalysts and others are characterized by elemental analysis, BET measurements, temperature programmed reduction, H_2-chemisorption measurements, and transmission electron microscopy. Catalytic tests are conducted in a continuous flow fixed-bed reactor.
The heat transfer aspect of the highly exothermic H_2-SCR of N_2O shall be examined by investigating the influence of the support's thermal conductivity.

4.2 Synthesis and characterization of the catalysts

4.2.1 Catalyst synthesis

Supported palladium catalysts were synthesized using two different methods: incipient wetness impregnation and precipitation deposition. For all catalysts, a palladium content of 1 wt.-% was intended. For incipient-wetness impregnation, the support materials were impregnated with a defined volume of aqueous solution containing a palladium precursor, followed by drying and calcination, leading to PdO on the supports. Precipitation deposition was carried out using a modified protocol adapted from Pearlman.[213],[214] By controlled increase of the pH of an acidic palladium solution, palladium hydroxide was precipitated onto the support (see Scheme 18). The products were dried and calcined under the same conditions as used in the incipient-wetness synthesis.

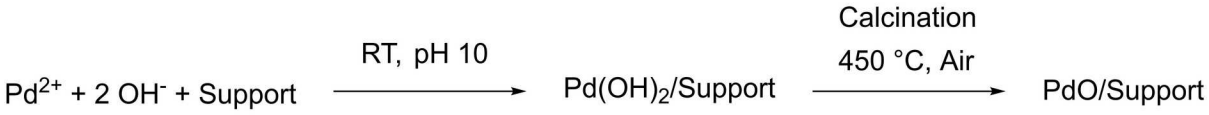

Scheme 18: Reaction sequence for the controlled precipitation synthesis of supported palladium catalysts.

Different types of catalyst supports were used in order to study the influence of the support on the catalytic activity, including AlF_3, Al_2O_3, CeO_2, SiC, SiO_2, TiO_2, ZnS, and sulfonated ZrO_2. These materials were selected due to their distinct physicochemical properties. SiO_2 served as a relatively neutral and inert reference support, whereas Al_2O_3 and sulfonated ZrO_2 represented supports with weak and strong acidity, respectively. The effect of support reducibility was studied using TiO_2 and CeO_2, which provide weak and strong redox characteristics, respectively. To examine non-oxidic supports, AlF_3 was included, as it can serve as a reference material for comparison with oxygen-containing supports (see also section 4.3.4).[215],[216] ZnS was selected as another non-oxidic support, enabling evaluation of the impact of sulfide presence on catalytic performance. Finally, SiC was chosen for its high thermal conductivity, allowing investigation of heat-transfer effects during catalysis (see also 4.3.6 and 4.5.1).[217]

Moreover, palladium nitrate, palladium chloride, and palladium acetyl acetonate were used as different precursors for both synthesis methods. Catalysts containing promoters were prepared by incipient-wetness impregnation of Pd/Al_2O_3 with aqueous alkali metal nitrate solutions.

For investigation of other noble metals in the catalytic N_2O reduction by H_2, Rh and Ru catalysts supported on Al_2O_3 and CeO_2 were synthesized by precipitation deposition. In order to ensure

high comparability, the same synthesis conditions as described for Pd were applied. Elemental analysis confirmed noble metal loadings of around 1 wt.-%.

Moreover, Rh catalysts supported on SiC and nanodiamond as supports with high thermal conductivity were synthesized by precipitation deposition. Pure, unsupported rhodium oxide was synthesized using a modified Pechini-type sol-gel approach similar to Santos *et al*.[218] Citric acid was implemented for coordinating to the Rh centers. Subsequently, polymerization of free and coordinated citric acid with ethylene glycol led to the formation of a polymeric resin. Calcination resulted in the removal of the polymeric resin, and pure rhodium oxide with a rather high surface area (roughly 20 m^2/g) was obtained.

4.2.2 Catalyst characterization

H_2 chemisorption measurements were carried out for the evaluation of the palladium dispersion on the catalysts. It is important to note that the absolute values of the palladium dispersion are not completely reliable, since the exact stoichiometry of hydrogen adsorption on Pd can vary depending on several complex factors. Typically, a ratio of one hydrogen atom per Pd surface atom is assumed.[219] However, hydrogen spillover and hydrogen uptake into Pd bulk can result in different ratios.[219],[220],[221] It was also shown that the stoichiometry of hydrogen adsorption on Pd can depend on the Pd dispersion itself.[222] Despite these limitations, the data are valuable for comparing the relative palladium dispersion across different catalyst samples. As determined by H_2 chemisorption, the palladium dispersions varied significantly between the catalysts.

As expected, deposition–precipitation synthesis by controlled precipitation of palladium hydroxide led to a higher Pd dispersion compared to incipient wetness impregnation (Table 10). This is a general, well-known observation for these catalyst synthesis methods. It is commonly assumed that the interaction between the Pd species and the support is stronger during precipitation, preventing sintering and enabling small particle sizes.[223],[224] Incipient-wetness impregnation typically leads to lower dispersion due to weaker interaction between the precursor and the support, which favors mobility of the precursor during the thermal treatment after impregnation.[225] However, in the case of $Pd(acac)_2$ as precursor in the catalyst synthesis, precipitation actually resulted in a lower Pd dispersion than impregnation, with 64% compared to 91%. This behavior may be attributed to the deposition mechanism. During impregnation, the intact $Pd(acac)_2$ complex adsorbs onto the support, whereas in precipitation, Pd is deposited as a hydroxide precipitate. Unlike palladium nitrate and chloride, $Pd(acac)_2$ must first dissociate, but the high stability of the metal complex due to chelating effects of the ligand slows this process. Therefore, the precipitation likely proceeds much more slowly than in the case of unbound Pd^{2+}, possibly resulting in more nucleation and particle agglomeration.

In contrast, in the case of the impregnation synthesis, the organic ligand might be favorable, as it may help to prevent agglomeration during the impregnation process.

The influence of the Pd precursor can also be seen for $Pd(NO_3)_2$ and $PdCl_2$. Using $PdCl_2$ as a precursor for precipitation deposition led to significantly higher Pd dispersion than using $Pd(NO_3)_2$ with 80% compared to 70%. Similarly, impregnation with $PdCl_2$ led to a dispersion of 43% compared to 23% with $Pd(NO_3)_2$.

The Pd dispersion was also affected by the choice of the catalyst support for otherwise identical synthesis conditions (palladium nitrate, precipitation deposition). Rather comparable dispersions were determined for Pd/Al_2O_3, Pd/ZrO_2, and Pd/SiO_2 with 70%, 71% and 60% respectively. On the other hand, the Pd dispersions of Pd/TiO_2 and Pd/SiC were significantly lower, with 33% and 26%. This may be attributed to the low BET surface areas of the support materials with 57 m^2/g and 25 m^2/g (Table 10), offering less available space for deposition. Very low Pd dispersion was measured for AlF_3 and ZnS, with 14% for Pd/AlF_3 and only 1% for ZnS. In this case, it is likely that the Pd particles were partially covered by fluoride and sulfide, or even formed palladium fluoride and sulfide, leading to fewer hydrogen chemisorption sites.

The addition of alkali metal promoters should, in principle, not significantly change the Pd particle sizes, as they were added by impregnation of synthesized Pd/Al_2O_3 after calcination. However, a strong decline in the H_2-uptake was determined for the promoted catalysts. This indicates that the Pd surface was partially covered by the alkali metals. Loading of Pd/Al_2O_3 with K decreased the measured Pd dispersion from 70% to 49% for 1 wt.-% K and down to 36 % for 2 wt.-% K.

Table 10: Overview of the characteristics of the Pd based catalysts.

Catalyst	Comment	BET surface area [m^2/g]	Palladium dispersion [%]*	Palladium surface area [m^2/g]*	Palladium particle size [nm]*
Pd/Al_2O_3.	Impregnated, Nitrate precursor	185	23	1.0	5.8
Pd/Al_2O_3.	Precipitated, Nitrate precursor		70	3.1	1.9
Pd/Al_2O_3.	Impregnated, Cl^- precursor, 450 °C calcination		43	1.9	3.1
Pd/Al_2O_3.	Impregnated, Cl^- precursor, 700 °C calcination		93	4.1	1.5
Pd/Al_2O_3.	Precipitated, Chloride precursor		79	3.6	1.7
Pd/Al_2O_3	Impregnated, acac precursor		91	1.5	
Pd/Al_2O_3	Precipitated, acac precursor		64	2.9	
Pd/CeO_2		143	Not quantifiable		
Pd/ZrO_2		136	71	3.2	1.9
Pd/TiO_2		57	33	2.7	4.1
Pd/SiO_2		128	60	2.7	2.3
Pd/SiC		32	26	1.2	5.2
Pd/AlF_3		60	14	0.6	9.3
Pd/ZnS			1	<0.1	100
1wt.-% $Na/Pd/Al_2O_3$			n.a.	n.a.	n.a.
1wt.-% $K/Pd/Al_2O_3$			49	2.2	2.8
2wt.-% $K/Pd/Al_2O_3$			36	1.6	3.7

* as calculated from H_2 pulse chemisorption measurements.

Hydrogen chemisorption measurements were also conducted for the determination of the Rh and Ru dispersion, see Table 11. As in the case of Pd, the determined values might deviate from the actual dispersion. Therefore, comparisons should be understood in a semi-quantitative sense. The highest H_2-uptake was measured for Rh/Al_2O_3, resulting in a Rh dispersion of 95% and a Rh particle size of 1.5 nm when assuming a stoichiometric adsorption of one hydrogen atom per Rh surface atom. This also shows that the synthesis approach of deposition precipitation, which was originally intended for Pd, also works very well for Rh. Similar, but lower dispersion was measured for Pd/Al_2O_3 with 70%, corresponding to a Pd particle size of 1.9 nm. In contrast, the Ru dispersion of Ru/Al_2O_3 was substantially lower, with only 6% and a noble metal particle size of 24.5 nm. This discrepancy might arise from the synthesis, which could have produced larger particles for Ru. Determination of the noble metal dispersion on CeO_2 was not feasible as CeO_2 itself participated as an adsorption site for H_2.

Table 11: Overview of the characteristics of the catalysts with different active noble metals.

Catalyst	**Noble metal dispersion [%]**	**Noble metal surface area [m^2/g]***	**Noble metal particle size [nm]**
Rh/Al_2O_3	95	4.1	1.5
Pd/Al_2O_3	70	3.1	1.9
Ru/Al_2O_3	6	0.26	24.5
Rh/CeO_2	n.a.	Not quantifiable	Not quantifiable
Pd/CeO_2	n.a	Not quantifiable	Not quantifiable
Ru/CeO_2	n.a	Not quantifiable	Not quantifiable

* as determined by H_2-chemisorption measurements.

Transmission electron microscopy (TEM) images of selected catalysts were recorded for further information on the catalyst dispersion. Figure 47 shows TEM images of Pd/Al_2O_3 prepared by precipitation deposition using $Pd(NO_3)_2$ as precursor. A large number of palladium particles were visible, which were distributed rather evenly over the Al_2O_3 surface. Statistical evaluation of the particle size distribution is presented in Figure 48. Most particles ranged from 2 to 8 nm in size, with only a few outliers having smaller or larger dimensions. The average particle size was 4.8 nm, notably larger than the 1.9 nm calculated from chemisorption data. This shows that hydrogen chemisorption led to overestimation of the Pd dispersion, likely due to the factors described above. However, it also needs to be pointed out that Pd particles smaller than 2 nm are significantly harder to detect in the TEM images, which might lead to overrepresentation of larger particle dimensions to some extent.

TEM images of Pd/CeO_2 (Figure 49), on the other hand, show no visible presence of palladium particles, potentially due to very small Pd particle sizes.

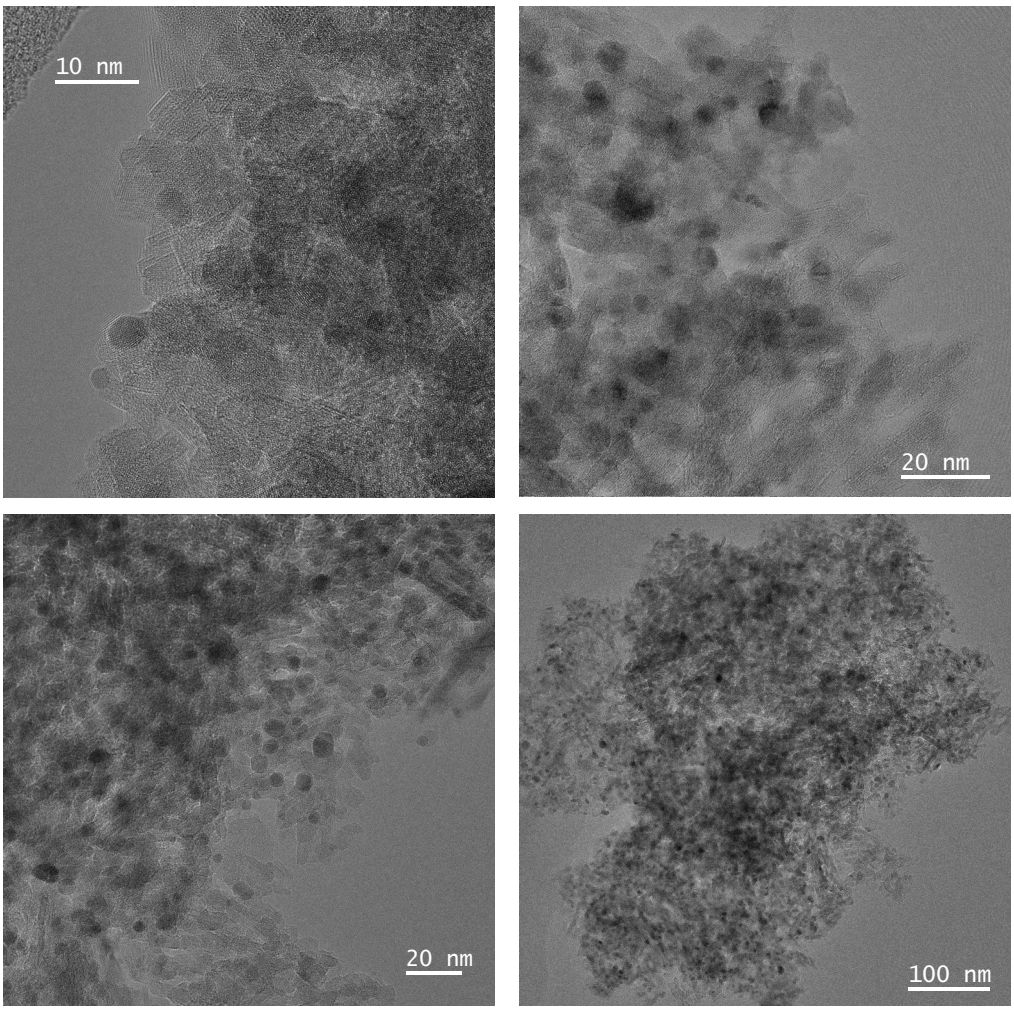

Figure 47: TEM images of Pd/Al2O3 (as synthesized).

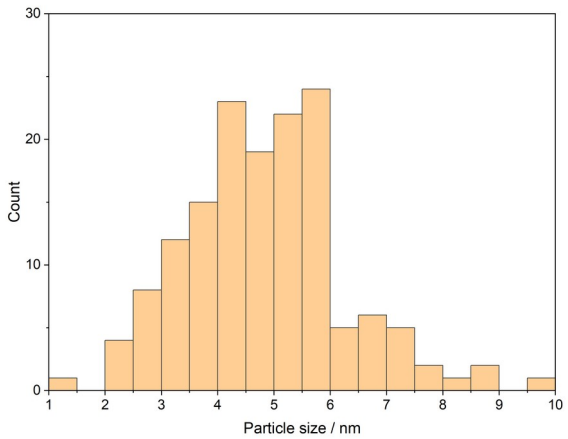

Figure 48: Particle size distribution for Pd/Al_2O_3 as determined from TEM images.

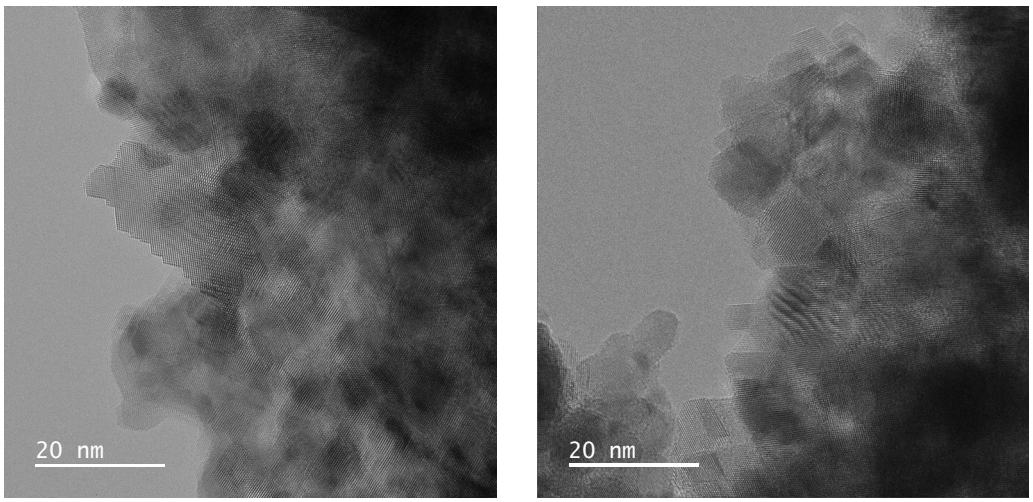

Figure 49: TEM images of Pd/CeO_2 (as synthesized).

TEM images of Rh/Al_2O_3 show significantly smaller particles compared to Pd/Al_2O_3 (Figure 50). A mean particle size of 1.8 nm was determined with a very narrow particle size distribution ranging from 1-3 nm, as depicted in Figure 51. The measured particle sizes are in good accordance with the value of 1.5 nm calculated from H_2 chemisorption. It appears that the stoichiometric ratio for hydrogen chemisorption for Rh is closer to one than for Pd, which likely is caused by more pronounced sub-surface adsorption and hydrogen spillover in the case of Pd.

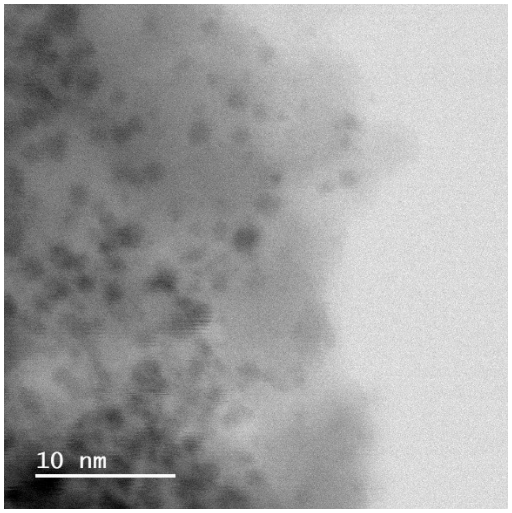

Figure 50: TEM image of Rh/Al_2O_3 (as synthesized).

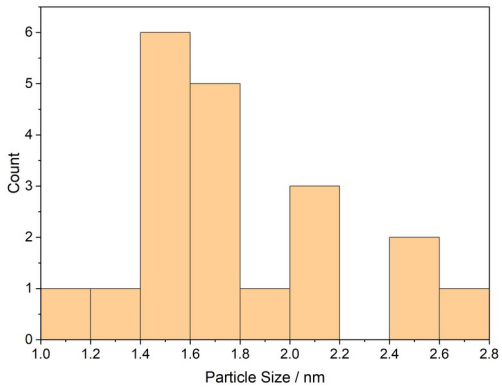

Figure 51: Rh particle size distribution of Rh/Al_2O_3 determined from TEM images.

Temperature programmed reduction (TPR) measurements were carried out in order to investigate the reduction behavior of the catalysts. The temperature was increased from -50 °C to 650 °C with a 10 K/min heating rate. The data was evaluated in a qualitative manner in most cases, as quantification of hydrogen consumption typically exceeded the calculated values for reduction of the palladium content. Figure 52 shows the TPR curves of Pd on different supports. In general, the reduction of Pd started already at very low temperatures, even below 0 °C in the case of Pd/TiO_2, Pd/ZrO_2, and Pd/Al_2O_3. The maxima of hydrogen consumption were mostly in the range of 0-50 °C, with a few exceptions. The reducibility of Pd/CeO_2 was slightly lower with a maximum of hydrogen consumption at around 64 °C, likely due to stronger interaction of Pd with the CeO_2 support and CeO_2 impeding the reduction of PdO.[226] Partial reduction of CeO_2 at the Pd-CeO_2 interfaces due to hydrogen spillover is suggested from the quantification of the hydrogen consumption in this case. In addition, a broad peak with low intensity between 300 °C and 450 °C indicates the reduction of surface CeO_2.[227] For the catalyst Pd/Al_2O_3, a small negative peak at 66 °C can be attributed to the release of hydrogen that had been inserted into Pd to form palladium hydride species at lower temperatures.[228] Moreover, a small broad peak between 250 °C and 300 °C is likely linked to palladium particles strongly interacting with the Al_2O_3 support.[229] The TPR curve of Pd/ZrO_2 is characterized by a variety of broad peaks. The first peak between 0-100 °C can be attributed to the reduction of PdO, while the peaks at around 245 °C and 470 °C represent the reduction of the ZrO_2 support at close proximity to Pd and the sulfate species at the ZrO_2 surface.[230] Very high temperatures were necessary for the reduction of PdO on ZnS, which took place between 300 °C and 400 °C. This shows that the presence of sulfide strongly hinders the reduction of palladium, likely due to palladium-sulfide interactions.

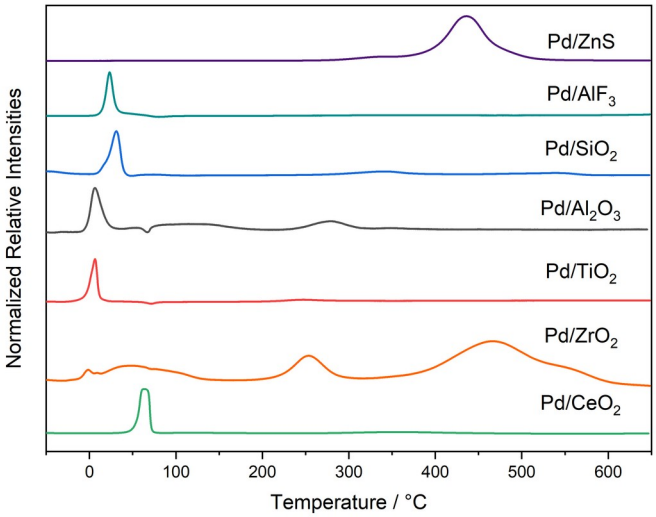

Figure 52: TPR curves for Pd catalysts with different supports. The data were recorded using a heating rate of 10 K/min and 20 mL/min total gas flow (10% H_2 in Ar).

The TPR curves, depending on the Pd precursor used in the catalyst synthesis, are shown in Figure 53. While the reduction peak of Pd was very sharp for the catalysts prepared by $Pd(NO_3)_2$, the catalysts prepared by $PdCl_2$ and $Pd(acac)_2$ exhibited very broad reduction peaks stretching from slightly above 0 °C to about 220 °C. Moreover, a second peak with lower intensity was observed for several catalysts, which was likely caused by strong interactions with the support.

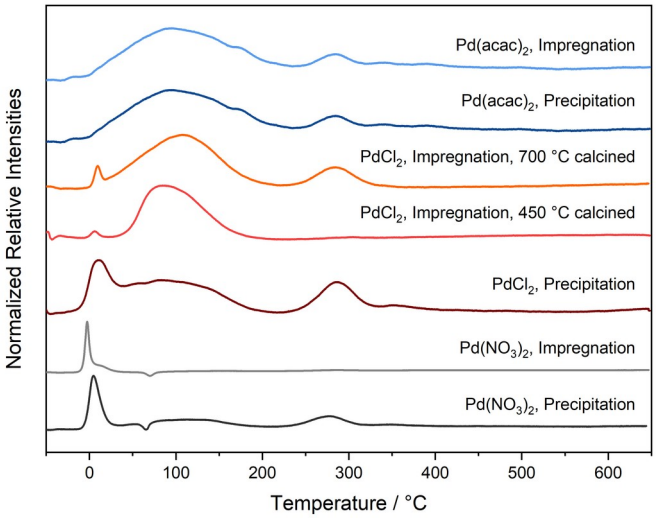

Figure 53: TPR curves for Pd/Al_2O_3 catalysts prepared from different Pd precursors. The data were recorded using a heating rate of 10 K/min and 20 mL/min total gas flow (10% H_2 in Ar).

The TPR profiles for Rh, Pd, and Ru on Al_2O_3 and CeO_2 are presented in Figure 54. The catalyst supported on CeO_2 exhibited not only reduction of the noble metal but also partial reduction of CeO_2, likely occurring in close proximity to the noble metal particles. This can be concluded from quantitative analysis of the peak areas and also can be seen by peak

broadening. The peaks for the reduction of Rh and Ru were shifted to significantly lower temperatures (around 57 °C and 25 °C, respectively) on CeO_2 compared to Al_2O_3 (86 °C and 120 °C), possibly due to less interaction with the support. On the other hand, the reduction temperature for Pd was higher on CeO_2 (9°C) than on Al_2O_3 (65 °C). Notably, Rh/Al_2O_3 exhibited an extremely broad reduction peak consisting of an initial rather sharp peak at 86 °C with an adjacent shoulder stretching to 500 °C. The latter can likely be attributed to Rh particles with very strong support interactions, which might occur due to the small Rh particle sizes as determined by H_2-chemisorption and from TEM images (see above). It is known from literature studies that formation of rhodium aluminates and diffusion of Rh atoms into the Al_2O_3 lattice can occur.[231],[232]

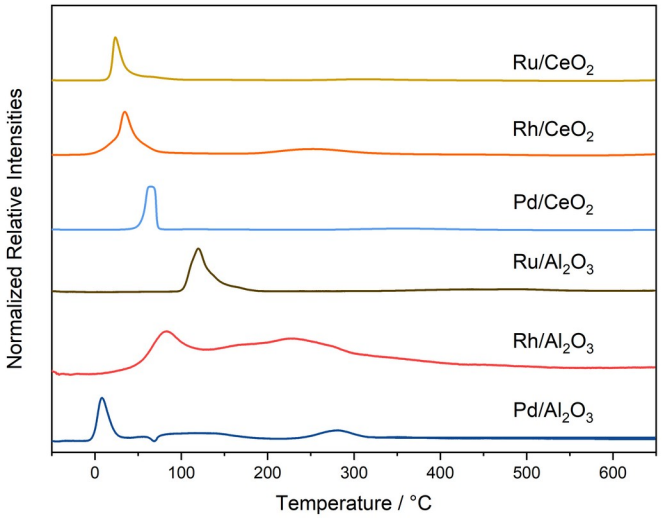

Figure 54: TPR curves for Pd, Rh and Ru catalysts supported on CeO_2 and Al_2O_3. The data were recorded using a heating rate of 10 K/min and 20 mL/min total gas flow (10% H_2 in Ar).

4.3 Investigations on the catalytic reduction of N_2O by H_2 in a fixed-bed reactor

The catalytic activity of the catalysts was determined in a fixed-bed continuous flow reactor using the catalysts in their calcined form. The reaction gas mixture (1100 ppm N_2O, 1500 ppm H_2, N_2 as carrier gas) was initially introduced at room temperature, but no N_2O conversion was observed under these initial conditions. The temperature of the reactor was stepwise increased until significant N_2O conversion commenced. While holding this individual temperature, the conversion increased over time. After full conversion, the activation temperature was maintained further for a prolonged period in order to ensure fully activated catalysts. The performance of the catalysts was then evaluated by stepwise variation of the reactor temperature, in order to obtain temperature-activity curves. Interestingly, when changing the temperature, there was a long equilibration time until the N_2O conversion reached a stable value. This phenomenon will be discussed in section 4.5.1. Moreover, in order to reach a

reactor temperature with no N_2O conversion, it was necessary for many catalysts to cool the reactor clearly below room temperature.

The focus of this investigation was to elucidate structure-activity relationships, which was performed by variation of palladium catalysts through different synthesis methods, different palladium precursors, the addition of promoters, and variation of the catalyst support. Moreover, the performance of different noble metals was investigated for rhodium, palladium, and ruthenium in order to further broaden the understanding of catalytic behavior. The focus remained on the catalytic reaction in the low-temperature range, as this temperature range is highly atypical for heterogeneous catalysis. The H_2-SCR of N_2O presents a practically unique model reaction in this regard.

4.3.1 Influence of the synthesis method

The influence of the synthesis method on the catalytic activity was investigated exemplarily for Pd supported on Al_2O_3. As described in 4.2.1, incipient-wetness impregnation and precipitation deposition were applied. The temperature-conversion curves of the catalysts are presented in Figure 55 for a WHSV of 12,000 $mL g^{-1} h^{-1}$ (estimated GHSV of approximately 6000 h^{-1}). Both catalysts were extremely active, as they exhibited full N_2O conversion at room temperature and needed to be cooled for assessment of the temperature-conversion relationships. Even around -70 °C, some conversion of N_2O could still be observed for both catalysts. The performance of the catalyst prepared by precipitation deposition is higher than that of the catalyst prepared by incipient-wetness impregnation. The temperature of 50% conversion, T_{50} of Pd/Al_2O_3 precipitated, was approximately -27 °C, while the T_{50} of Pd/Al_2O_3 impregnated was around -19 °C. This difference can be attributed to the Pd dispersion of Pd/Al_2O_3 precipitated being significantly higher than that of Pd/Al_2O_3 impregnated, as determined by chemisorption measurements (see 4.2.2). This demonstrates that higher Pd dispersion is favorable for improved efficiency of the catalysts in the H_2-SCR of N_2O. However, this effect is surprisingly small, considering the large discrepancy in the Pd dispersions with 70% for precipitation and 23% for impregnation.

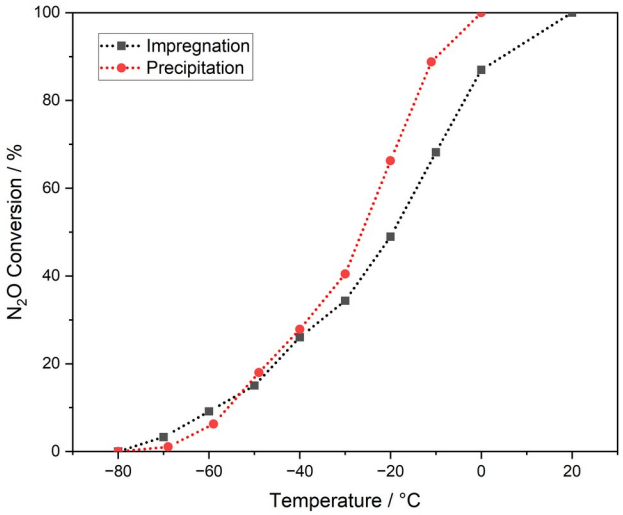

Figure 55: Conversion of N_2O over Pd/Al_2O_3 catalysts prepared by precipitation (red curve) and impregnation (black curve) depending on the reaction temperature (WHSV = 12 000 $mLg^{-1}h^{-1}$, 1100 ppm N_2O, 1500 ppm H_2, balance gas: N_2). Pretreatment: Activation at 50 °C under catalysis gas flow.

4.3.2 Influence of the palladium precursor

The influence of the palladium precursor on the catalytic activity was investigated for Pd supported on Al_2O_3 for both synthesis methods, impregnation and precipitation. Three different Pd precursors were used: Palladium nitrate, palladium acetylacetonate, and palladium chloride. Figure 56 shows the temperature-conversion curves of the catalysts prepared by impregnation. The highest catalytic activity was observed for palladium nitrate as a precursor with a T_{50} of around -19 °C, compared to the T_{50} for $Pd(acac)_2$ with -12 °C and the T_{50} for $PdCl_2$ of 78 °C. The drastically lower performance with $PdCl_2$ indicates that calcination at 450 °C did not completely remove all the chloride present after impregnation. Instead, some remains of chloride likely still existed in the product, which caused severe impairment of the catalyst. In order to confirm this hypothesis, another catalyst was prepared by impregnation using palladium chloride and a calcination temperature of 700 °C. The performance of this catalyst was considerably increased, indicating that more chloride or possibly all chloride was removed with this high temperature treatment. In fact, the T_{50} was identical to that of $Pd(NO_3)_2$ with -19 °C. Interestingly, the performance of the catalyst at very low temperatures was significantly worse compared to the catalyst prepared by $Pd(NO_3)_2$, while the performance above -19 °C was higher. As determined by chemisorption measurements, the dispersion for the catalyst prepared by $PdCl_2$ with a calcination temperature of 700 °C exhibited much higher Pd dispersion (93%) than the catalyst prepared by $Pd(NO_3)_2$ (23%), despite the high calcination temperature. Higher Pd dispersions with palladium chloride over nitrate were also reported in the literature for silica supported Pd catalysts.[233] It is therefore plausible that without chloride residues, the catalyst prepared from $PdCl_2$ would actually lead to higher performance than Pd/Al_2O_3 prepared from $Pd(NO_3)_2$.

The rather low performance of the catalyst prepared from $Pd(acac)_2$ is surprising, as chemisorption measurements showed a very high Pd dispersion for this catalyst with 91%.

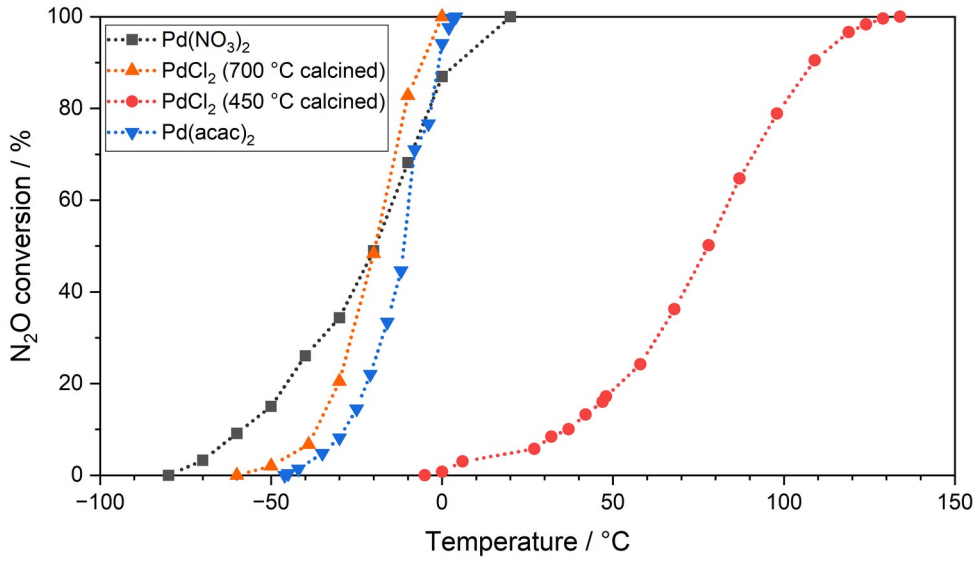

Figure 56: Temperature dependent conversion of N_2O over Pd/Al_2O_3 catalysts prepared by impregnation using $Pd(NO)_3$ (black), $PdCl_2$ (red) or $Pd(acac)_2$ (WHSV = 12 000 $mLg^{-1}h^{-1}$, 1100 ppm N_2O, 1500 ppm H_2, balance gas: N_2).

Figure 57 shows the temperature-conversion curves of the catalysts prepared by precipitation. Similar to the catalysts prepared by impregnation, palladium nitrate resulted in the highest catalytic performance among the three palladium precursors, with a T_{50} of -27 °C. However, the activity of the catalyst prepared with $PdCl_2$ with a T_{50} of -20 °C was much closer to that of palladium nitrate than for the case of the impregnated catalysts. This is due to a significant amount of chloride being removed from the catalysts due to washing of the products after precipitation, which is not possible for impregnation. According to chemisorption measurements, the dispersion obtained with $PdCl_2$ with 79% is higher than that obtained with $Pd(NO_3)_2$ (70%), which is contrary to their relative catalytic performance. This indicates that the sensitivity of the catalysts to chloride poisoning is extremely high in the H_2-reduction of N_2O, as it is likely that only traces of chloride residues could be present in the catalyst after washing and calcination.

Like in the case of impregnation, the performance of the catalyst prepared from palladium acetylacetonate is lower than that of Pd/Al_2O_3 prepared from $Pd(NO_3)_2$. In this case, however, the dispersion of the catalyst prepared from $Pd(acac)_2$ is slightly lower (64%) than that prepared from $Pd(NO_3)_2$.

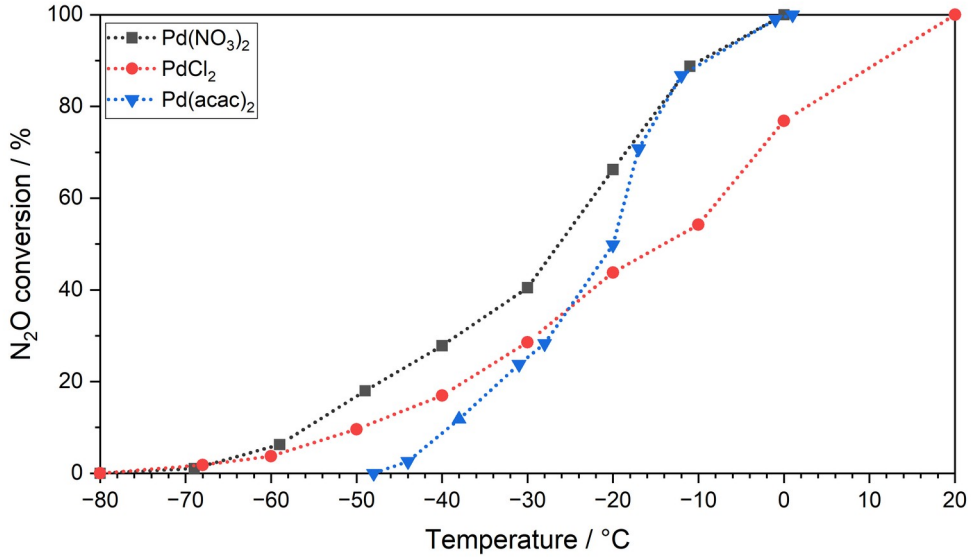

Figure 57: Temperature dependent conversion of N_2O over Pd/Al_2O_3 catalysts prepared by precipitation using $Pd(NO)_3$ (black), $PdCl_2$ (red) or $Pd(acac)_2$ (WHSV = 12 000 $mLg^{-1}h^{-1}$, 1100 ppm N_2O, 1500 ppm H_2, balance gas: N_2).

4.3.3 Influence of alkali metal promoters

In order to investigate the influence of alkali metal promoters, Pd/Al_2O_3 prepared by precipitation with $Pd(NO_3)_2$ was used as a starting point and modified by impregnation with sodium or potassium nitrate solutions. Figure 58 shows the temperature-conversion curves of the catalysts with 1 wt.-% Na, 1 wt.-% K and 2 wt.-% K as well as unpromoted Pd/Al_2O_3. A clearly beneficial effect of the alkali promoters on the catalytic performance was observed as the T_{50} was shifted more than 20 K lower. This effect is slightly stronger for K compared to Na, with a T_{50} of -48 °C for 1 wt.-% K compared to a T_{50} of -43 °C for 1 wt.-% Na. Moreover, an increase of the promoter loading appeared not to further enhance the performance, but in fact rather decreased it slightly, with a T_{50} of -43 °C for 2 wt.-% K.

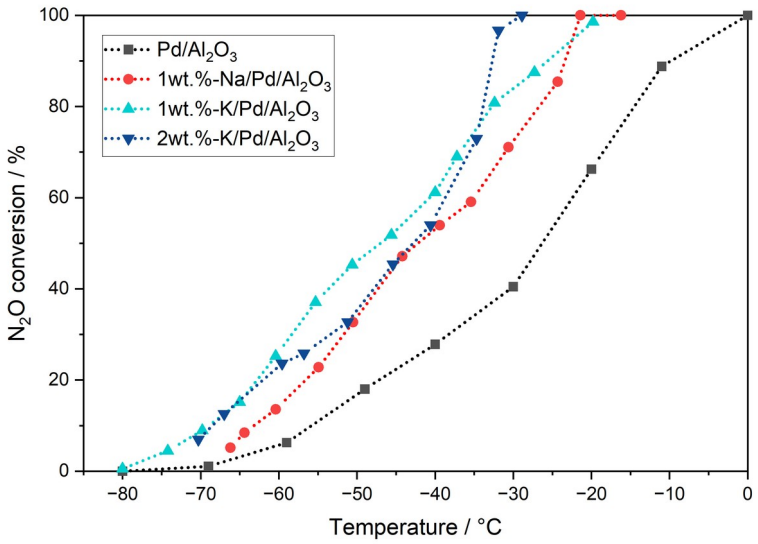

Figure 58: Conversion of N_2O over palladium catalysts with different promotors depending on the reaction temperature (WHSV = 12 000 $mLg^{-1}h^{-1}$, 1100 ppm N_2O, 1500 ppm H_2, balance gas: N_2

4.3.4 Influence of the catalyst support

In order to investigate the influence of the catalyst support, different types of materials were selected. This included SiO_2 as a rather neutral and inert support, Al_2O_3 as a support with acidic properties, sulfonated ZrO_2 with strong acidic properties, TiO_2 as a support with weak redox properties, and CeO_2 as a support with strong redox properties. Moreover, non-oxidic supports were studied. High surface area (about 60 m^2/g) AlF_3 was selected as a relevant support without oxygen in its lattice and with high intrinsic Lewis acidity.[216] ZnS was selected to investigate the influence of sulfide presence on catalyst performance. Moreover, SiC was tested as a catalyst support with high thermal conductivity (see also 4.3.6 and 4.5.1).[217] All catalysts were prepared by the same precipitation deposition protocol using palladium nitrate as a precursor. Figure 59 shows the temperature-conversion curves of the catalysts. It is notable that the catalysts with oxidic supports all perform rather similarly and convert N_2O below room temperature. In particular for Pd/CeO_2, Pd/ZrO_2, Pd/TiO_2 and Pd/Al_2O_3, the T_{50} are very close with -37 °C, -35 °C, -30 °C and -27 °C, respectively. High activities were also achieved with Pd/SiO_2, however, with a notably higher T_{50} of -15 °C than for the other oxidic supports, despite comparable Pd dispersion as determined by H_2 chemisorption.

Drastically lower catalytic performance was observed for Pd/SiC with a T_{50} of 116 °C, which indicates a substantial effect of the thermal conductivity of the support. The lowest activities were observed for Pd/AlF_3 and Pd/ZnS with T_{50} temperatures of 135 °C and 232 °C, which can probably be attributed to the detrimental effect of halides and sulfides on the catalytic performance. In addition, this may indicate a potential role of surface or lattice oxygen from the

support, with a more complex scenario in which support oxygen is involved in the catalytic process.[215],[234] Further in-depth studies are required to clarify this aspect.

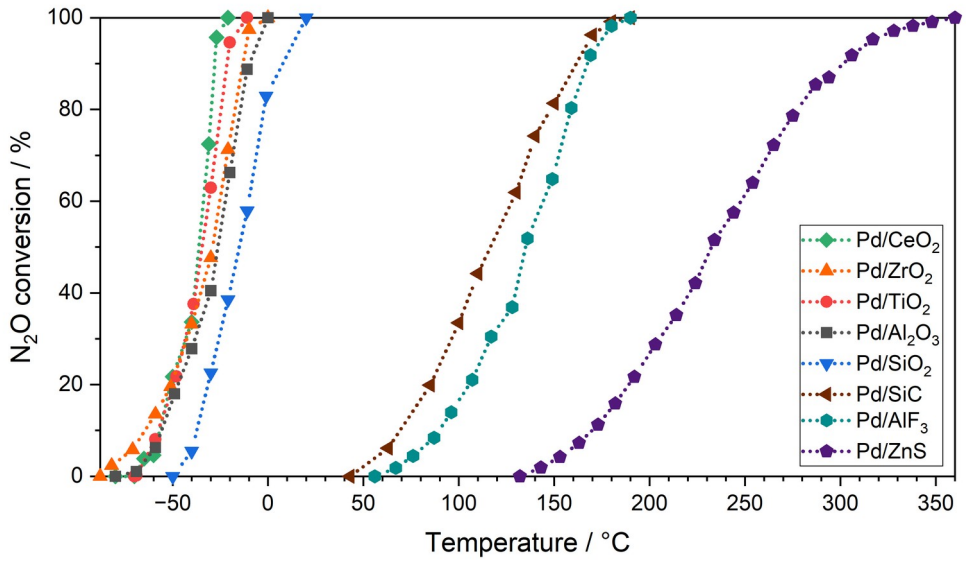

Figure 59: Conversion of N_2O over palladium catalysts on different supports depending on the reaction temperature (WHSV = 12 000 $mL g^{-1} h^{-1}$, 1100 ppm N_2O, 1500 ppm H_2, balance gas: N_2

4.3.5 Catalytic performance depending on the noble metal

The effectiveness of different noble metals in the H_2-SCR of N_2O is presented in Figure 60, with the temperature-conversion curves for Rh, Pd, and Ru on CeO_2 and Al_2O_3. A summary of the T_{50} values is presented in Table 12 and Figure 61. Conversion of N_2O was possible at exceptionally low temperatures, even at -80 °C over Rh/Al_2O_3. In addition, the temperature with 50% N_2O conversion (T_{50}) was -66°C for this catalyst, which is remarkably low for catalytic reactions in general. Rh/CeO_2 also demonstrated very high activity, however, with a T_{50} of -46 °C. Palladium supported on both Al_2O_3 and CeO_2 exhibited lower activity compared to rhodium; however, was still active at temperatures clearly below room temperature. The T_{50} values were -29 °C for Pd/Al_2O_3 and -37 °C for Pd/CeO_2. On the other hand, considerably lower performance was observed for Ru/CeO_2, with no N_2O conversion at sub-zero temperatures and a T_{50} of 49 °C. Even worse performance was obtained for Ru/Al_2O_3 with a T_{50} of 110 °C. Concerning the catalyst support, it was observed that CeO_2 led to enhancement of the catalytic performance at higher temperatures, which is evident for Ru with a difference of T_{50} of 61 K between CeO_2 and Al_2O_3. Lower temperatures were less favorable for CeO_2, with only a difference of 8 K in the case of Pd. Moreover, Al_2O_3 as support led to higher performance compared to CeO_2 in the case of Rh, allowing a 20 K lower T_{50}. CeO_2 is well known for its beneficial effects on the performance in catalytic $DeNO_x$ reactions, including N_2O decomposition and reduction.[235] This is attributed to its pronounced redox properties and

strong formation of oxygen vacancies, which can serve as adsorption sites for N_2O. It may be that this effect becomes less pronounced at lower temperatures due to the formation of oxygen vacancies being less favorable under sub-ambient conditions.

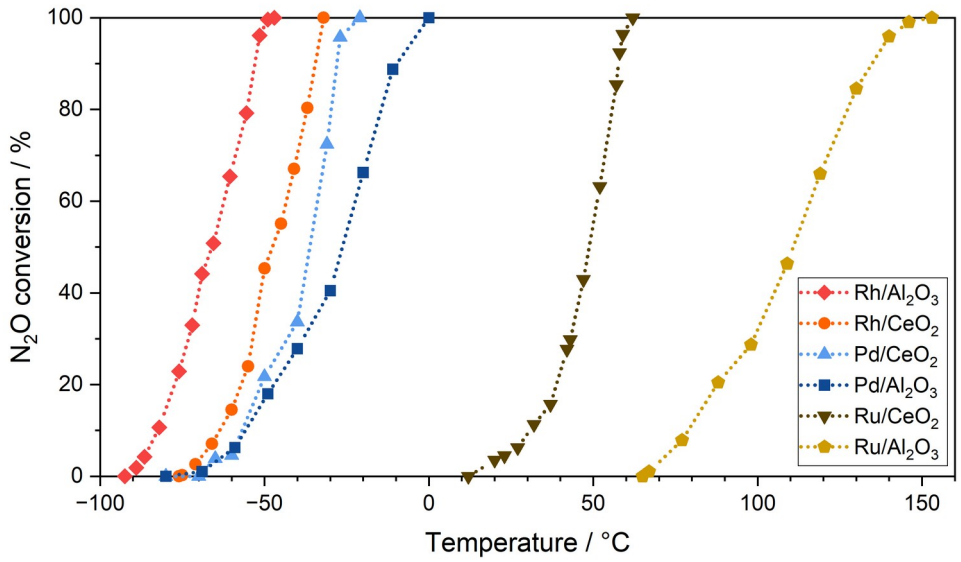

Figure 60: Conversion of N_2O over CeO_2 and Al_2O_3 based catalysts depending on the reaction temperature (WHSV = 12 000 $mLg^{-1}h^{-1}$, 1100 ppm N_2O, 1500 ppm H_2, balance gas: N_2).

Table 12: Summarized T_{50} of the catalysts.

Catalyst	T_{50} [°C]
Rh/Al_2O_3	-66
Pd/Al_2O_3	-29
Ru/Al_2O_3	110
Rh/CeO_2	-46
Pd/CeO_2	-37
Ru/CeO_2	49

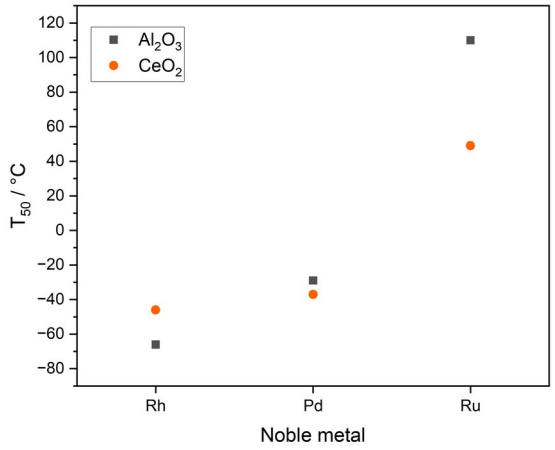

Figure 61: Comparison of the determined T_{50} for the investigated catalysts.

4.3.6 Investigation on the role of heat conduction of the catalyst support

In order to further investigate the effect of the thermal conductivity as described in 4.3.4, several catalysts with Rh on supports with high thermal conductivity, as well as pure, unsupported Rh, were investigated. Nanodiamond (ND) was selected as a support material with extremely high thermal conductivity, see also Table 13.

Table 13: Thermal conductivities and specific heat capacities of selected materials.[235],[236]

Material	Thermal conductivity ($W\ m^{-1}\ K^{-1}$)	Specific heat capacity ($J\ kg^{-1}\ K^{-1}$)
Al_2O_3	35.6–39	795-880
SiO_2	1.38	787
α-SiC	42.5	690
β-SiC	135	1205
Diamond	900 (type I), 2400 (type IIa)	-
Rhodium	150	242

Moreover, silicon carbide with varying BET surface areas (25 and 150 m²/g) was employed to investigate the potential influence of catalyst support primary particle size on heat transfer.
The catalysts supported on high thermal conductivity materials as well as unsupported Rh exhibited distinct behavior compared to those supported on materials with lower thermal conductivity. It was therefore not possible to perform temperature dependent conversion investigations, as the time for equilibrium was substantially longer than in the case of e.g. CeO_2 and Al_2O_3 as catalyst supports. Instead, the change in N_2O conversion at room temperature was monitored over time. All catalysts were first reduced under reaction conditions at 100 °C. After that, the catalysts were cooled down under flowing inert gas before introducing the gas mixture for H_2-N_2O SCR again. In all cases, there was an initiation period (around 40 min) at the start, when the catalysts became increasingly more active (Figure 62-Figure 65). This time period was significantly shorter in the case of unsupported Rh (ca. 20 min, Figure 64). After that, the conversion very slowly, but gradually declined again. This decline was much less pronounced for unsupported Rh, but still measurable. Rh/ND, on the other hand, showed a very similar decline in N_2O conversion at first (Figure 65). After continuing the catalytic reaction over night, the N_2O conversion increased drastically and reached almost full conversion. This different behavior might be due to incomplete reduction of Rh under the initial reduction, which was carried out at 50 °C instead of 100 °C in order to avoid potential destruction of the ND support. After a prolonged time on stream, the activity of Rh/ND increased significantly, likely due to full reduction of Rh. Notably, carbon supports have shown certain reactivity with nitrogen oxides in the literature.[238] However, no indication of any

stoichiometric reaction of the diamond support with N_2O was observed due to the absence of CO_2 bands in the FT-IR spectra of the product gas.

In any case, the catalytic behavior when using SiC or nanodiamond as support, as well as when using unsupported Rh, is strongly different than when using CeO_2 or Al_2O_3, suggesting that the heat transfer of the noble metal particles to the support may play an important role.

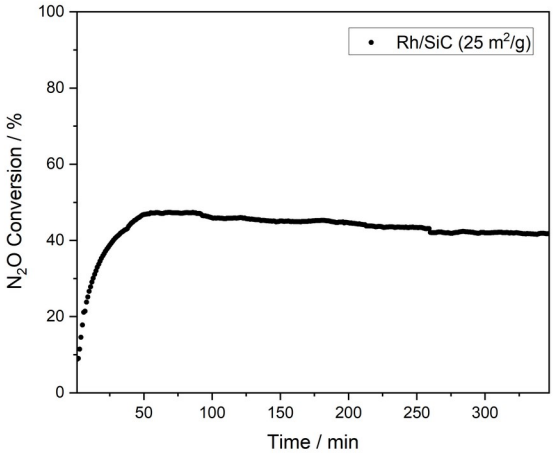

Figure 62: Conversion of N_2O over Rh/SiC (25 m^2/g specific surface area SiC) at room temperature (WHSV = 12 000 mL $g^{-1}h^{-1}$, 1100 ppm N_2O, 1500 ppm H_2, balance gas: N_2) after reduction at 100 °C.

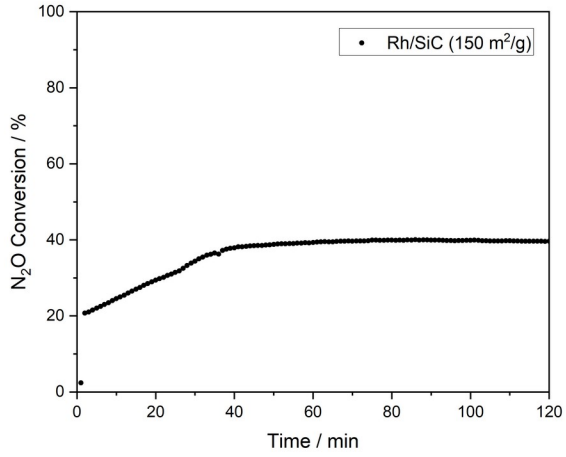

Figure 63: Conversion of N_2O over Rh/SiC (150 m^2/g specific surface area SiC) at room temperature (WHSV = 12 000 mL $g^{-1}h^{-1}$, 1100 ppm N_2O, 1500 ppm H_2, balance gas: N_2) after reduction at 100 °C.

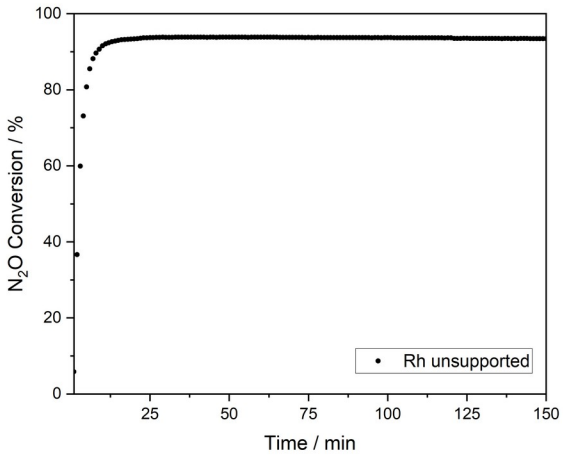

Figure 64: Conversion of N_2O over unsupported Rh (specific surface area about 20 m^2/g) at room temperature (WHSV = 12 000 mL $g^{-1}h^{-1}$, 1100 ppm N_2O, 1500 ppm H_2, balance gas: N_2) after reduction at 100 °C.

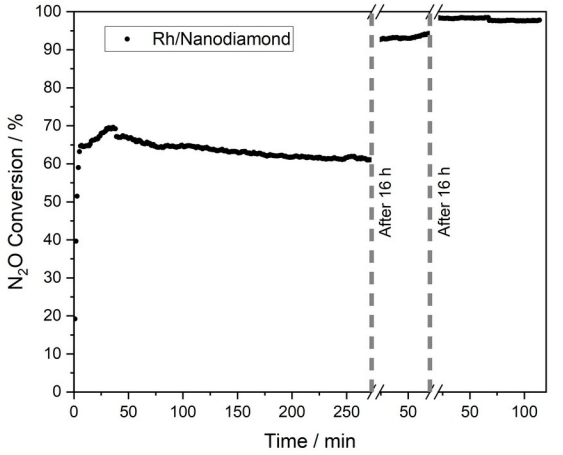

Figure 65: Conversion of N_2O over Rh/Nanodiamond at room temperature (WHSV = 12 000 mL $g^{-1}h^{-1}$, 1100 ppm N_2O, 1500 ppm H_2, balance gas: N_2) after reduction at 50 °C.

4.4 XPS investigations on the catalytic reduction of N_2O by H_2 [4]

For insight of the catalyst behavior during catalytic reduction of N_2O by H_2, quasi *in situ* XPS measurements were performed. Rh/Al_2O_3 and Rh/CeO_2 were selected as representative catalysts, as they exhibited the highest catalytic performance in the fixed-bed reactor. Due to the high experimental effort involved, the investigation was limited to these two catalysts, but it is plausible that the behavior is fundamentally similar for other catalyst systems. Varying the catalyst support enables comparison of the effect of support reducibility, with Al_2O_3 representing a non-reducible support and CeO_2 a reducible one.
XPS spectra of the catalysts were recorded after exposure to different conditions. The gases were dosed directly into the XPS chamber, with the catalysts mounted on a heatable sample holder.

4.4.1 XPS investigations on Rh/Al_2O_3

The change of the Rh 3d core levels of Rh/Al_2O_3 depending on the treatment conditions is shown in Figure 66. Directly after catalyst synthesis (marked as _0), only oxidized Rh was present, as shown by its Rh 3d core level spectra. After exposure to H_2 (50 mbar) at around 200 °C (_1), significant, but not complete, formation of metallic Rh was observed, with a calculated content of 56%. When increasing the reduction temperature to 300 °C, the fraction of Rh(0) to the total amount of Rh increased to 76%. This behavior matches the reduction profile of Rh/Al_2O_3 during TPR quite well, which also showed a very broad temperature range for Rh reduction on this catalyst (Figure 54). Oxidation of the catalyst was investigated by exposure to plasma (_7) as well as oxygen dosing at 375 °C (_9), leading to Rh contents of 41% and 13%, respectively. Concerning the total Rh(3d), a 10% decrease was observed after reduction at 300 °C (_4), which is likely caused by sintering effects. After this step, the total Rh(3d) intensities remained almost constant, indicating no further significant structural changes. The binding energies of oxidized Rh (blue curve) shifted between 309.5 eV (spectra _0, _7 to _10) and 310 eV (_1 to _5), with values of 308-310 eV typically reported in literature.[239],[240] The metallic Rh component was found at 307.1-307.5 eV, which is in good agreement with the literature reference value at 307.2 eV.[241]

[4] Disclaimer: This section (section 4.4) is based on XPS experiments which were performed by Tim Kratky and Sebastian Günther. See section 4.7 for more information.

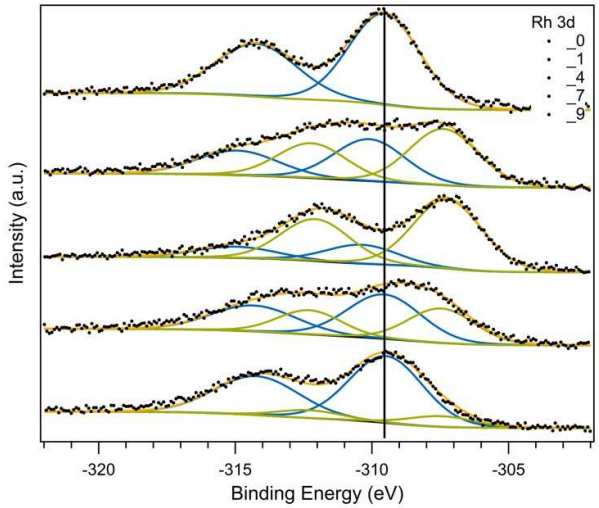

Figure 66: Rh 3d core levels of Rh/Al_2O_3 depending on the treatment conditions. Assignment: _0: as synthesized. _1: 50 mbar, H_2 200 °C. _4 50 mbar H_2, 300 °C. _7: plasma oxidation. _9: 50 mbar O_2, 375 °C.

Catalytic reduction of N_2O by H_2 was performed at room temperature after each pre-treatment by introduction of 1.5 mbar H_2, 1.0 mbar N_2O and 1.0 mbar Ar into the XPS chamber. XPS spectra were recorded after the SCR runs (Figure 67). After reduction at 200 °C (_1), the catalyst showed activity after a pronounced initiation period, as described in more detail below (_3). As shown in Figure 71 the metallic Rh content remained at 55% after catalysis. Moreover, the total Rh 3d intensity remained constant (within 5%), providing no indication of structural changes during catalysis.

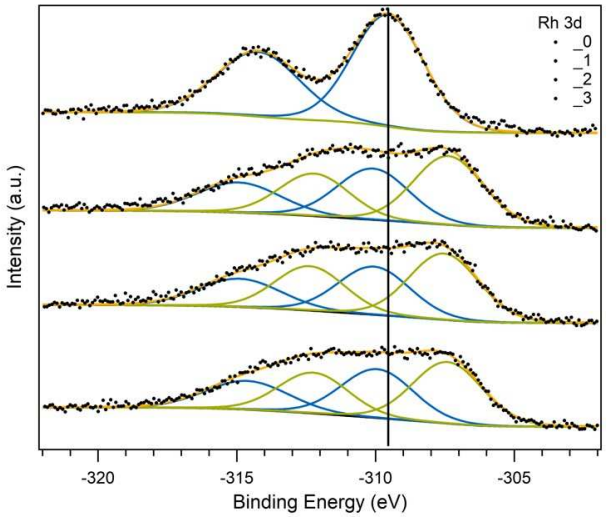

Figure 67: Rh 3d core levels of Rh/Al_2O_3 depending on the treatment conditions. Assignment: _0: as synthesized. _1: 50 mbar, H_2 200 °C. _2: SCR (1.5 mbar H_2, 1.0 mbar N_2O, 1.0 mbar Ar, room temperature). _3: SCR (1.5 mbar H_2, 1.0 mbar N_2O, 1.0 mbar Ar, room temperature).

Catalytic reduction of N_2O by H_2 was carried out after reduction at 300 °C (_4), showing high activity of the catalyst (see below). No changes in the metallic Rh content of 75% were observed when comparing the Rh 3d spectra before (_4) and after (_5) catalysis (Figure 68, Figure 71). The total Rh intensity also remained constant.

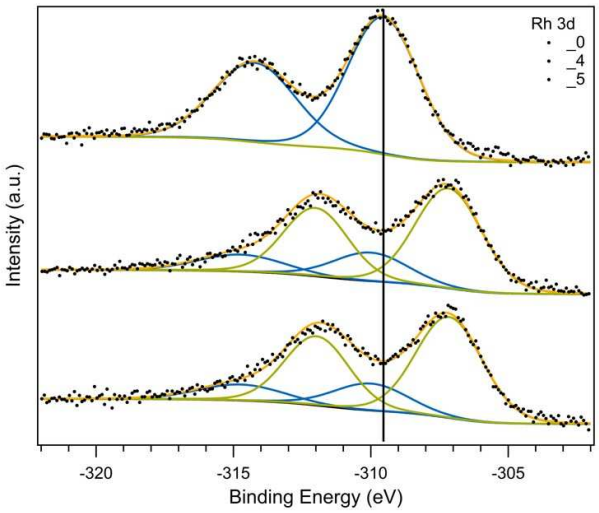

Figure 68: Rh 3d core levels of Rh/Al_2O_3 depending on the treatment conditions. Assignment: _0: as synthesized. _4: 50 mbar H_2, 300 °C. _5: SCR (1.5 mbar H_2, 1.0 mbar N_2O, 1.0 mbar Ar, room temperature).

Catalysis was also performed using the partially oxidized catalyst following plasma oxidation (_7). The proportion of Rh⁰ increased from 41% after plasma treatment to 57% during the catalytic run, see Figure 69 and Figure 71. The total Rh intensity remained constant with only a small increase (within 5%).

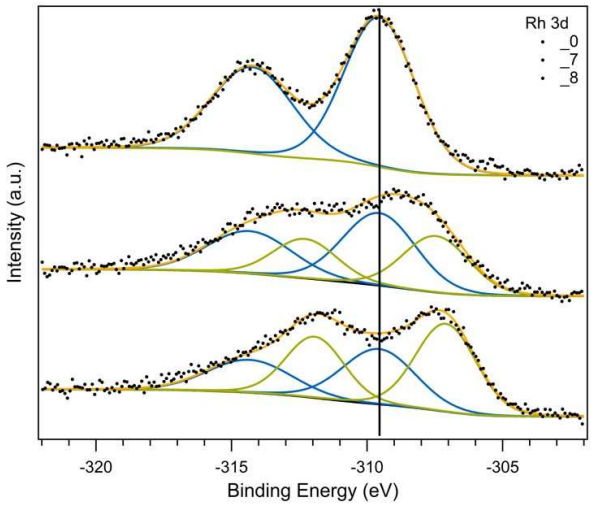

Figure 69: Rh 3d core levels of Rh/Al_2O_3 depending on the treatment conditions. Assignment: _0: as synthesized. _7: plasma oxidation. _8: SCR (1.5 mbar H_2, 1.0 mbar N_2O, 1.0 mbar Ar, room temperature).

After oxidation at 375 °C (_9), catalysis was carried out on the almost entirely oxidized catalyst, which resulted in moderate activity (see below). A significant increase of the metallic Rh fraction occurred during the catalytic run (Figure 70 and Figure 71) rising from 13% to 22%, while the total Rh intensity remained constant.

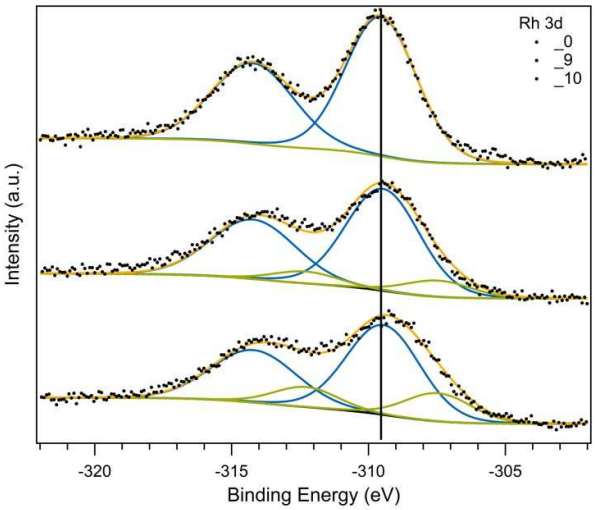

Figure 70: Rh 3d core levels of Rh/Al_2O_3 depending on the treatment conditions. Assignment: _0: as synthesized. _9: 50 mbar O_2, 375 °C. _10: SCR (1.5 mbar H_2, 1.0 mbar N_2O, 1.0 mbar Ar, room temperature).

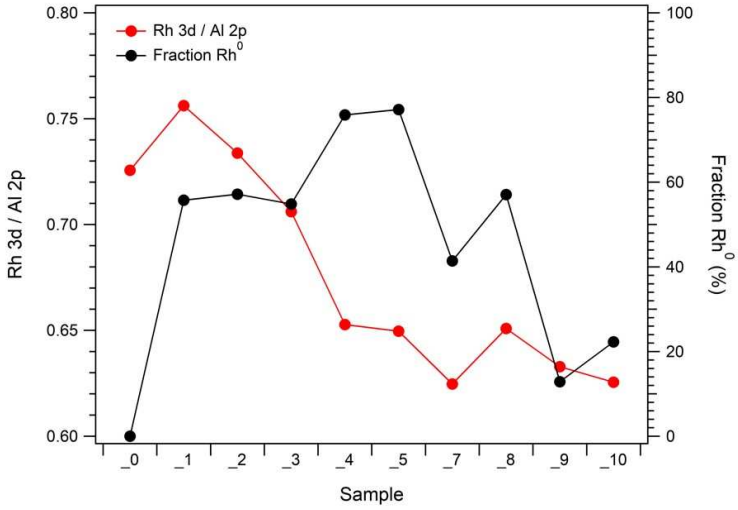

Figure 71: Fraction of Rh^0 and Rh 3d / Al 2p intensity ratios depending on the treatment conditions. Assignment: _0: as synthesized. _1: 50 mbar, H_2 200 °C. _2: SCR (1.5 mbar H_2, 1.0 mbar N_2O, 1.0 mbar Ar, room temperature). _3: SCR (1.5 mbar H_2, 1.0 mbar N_2O, 1.0 mbar Ar, room temperature). _4: 50 mbar H_2, 300 °C. _5: SCR (1.5 mbar H_2, 1.0 mbar N_2O, 1.0 mbar Ar, room temperature). _7: plasma oxidation. _8: SCR (1.5 mbar H_2, 1.0 mbar N_2O, 1.0 mbar Ar, room temperature). _9: 50 mbar O_2, 375 °C. _10: SCR (1.5 mbar H_2, 1.0 mbar N_2O, 1.0 mbar Ar, room temperature).

The evolution of the gas atmosphere in the XPS chamber during the individual catalysis runs was monitored by online mass spectrometry. The catalytic behavior of Rh/Al_2O_3 reduced at 200 °C (_3) and 300 °C (_5) is presented in Figure 72. There is a clear difference between the two samples in the response time until N_2 and H_2O formation take place. Sample _5 with a larger fraction of Rh^0 was active directly from the start, while sample _3 showed a delayed onset of product formation. In addition, the reactivity of sample _3 was clearly lower than that of sample_5, as the time until complete conversion was longer. Nonetheless, both catalysts were active at room temperature and eventually exhibited complete conversion of N_2O.

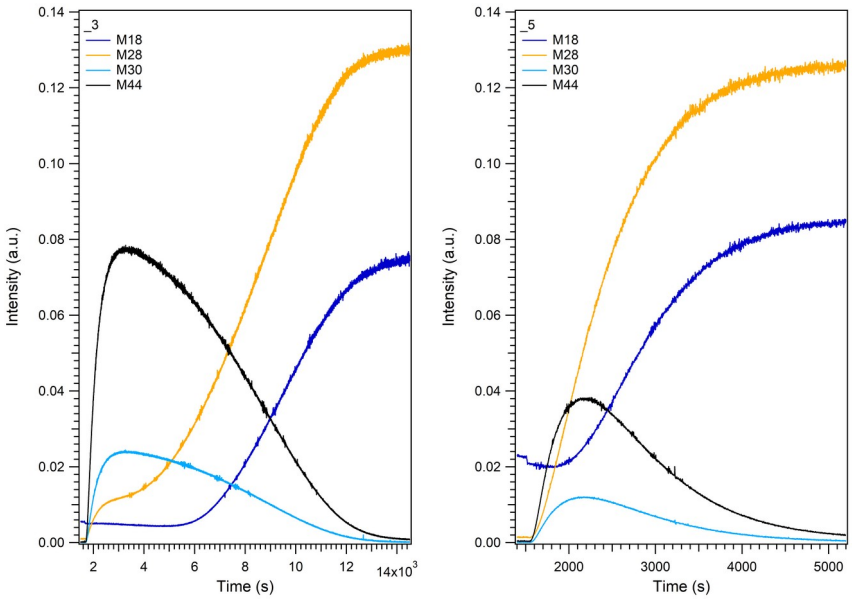

Figure 72: Evolution of the intensities of m/z 18, m/z 28, m/z 30 and m/z 44 during SCR (1.5 mbar H_2, 1.0 mbar N_2O, 1.0 mbar Ar, room temperature) over Rh/Al_2O_3 for different pretreatment as measured by a mass spectrometer connected to the XPS chamber. Left: SCR after 200 °C reduction. Right: SCR after 300 °C reduction.

An overview of all Rh/Al_2O_3 catalytic runs depending on the preconditioning is given in Figure 73. The catalytic performance of the samples can be compared using the maxima of the N_2O concentrations in the mass spectra. As a general trend, it was observed that a steeper slope in N_2 (M28) corresponded to an earlier and lower maximum in N_2O (M44). The highest catalytic activity was observed for sample _5, which also features the highest metallic Rh content. Performing a consequent second catalytic run (sample _6) resulted in slightly lower activity. Interestingly, the catalyst after plasma oxidation (_8) showed clearly lower performance than the catalyst after thermal oxidation (_10), despite a larger Rh^0 fraction. In addition, both oxidized samples showed higher catalytic performance than the catalyst reduced at 200 °C. This shows that the catalytic performance does not strictly correlate with the Rh^0 fraction.

It is likely that the reduction and subsequent re-oxidation of Rh lead to a higher reducibility compared to the oxidic Rh state in the as-synthesized catalyst. This improved reducibility may result from the modification or disruption of strong metal–support interactions of Rh/Al_2O_3 during re-oxidation, similar to the investigation of Anderson and Burch on Rh/TiO_2.[242] This may also explain why the Rh^0 fraction increased significantly upon catalysis for both oxidizing pretreatments, while it remained unchanged for both reductive pretreatments. Nonetheless, the results generally indicate that Rh^0 is the active species for catalytic N_2O reduction by H_2 over Rh catalysts.

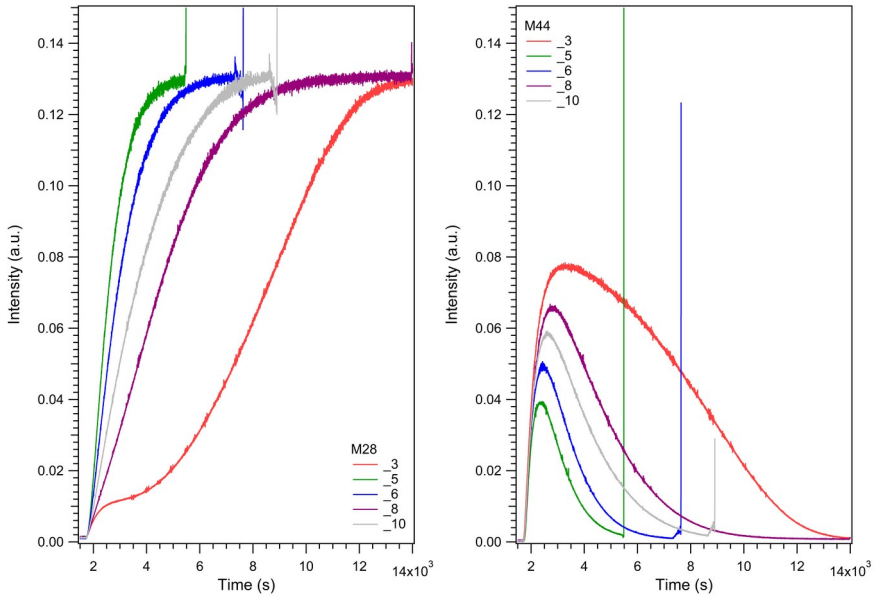

Figure 73: Comparison of the evolution of m/z 28 (left) and m/z 44 (right) during SCR (1.5 mbar H_2, 1.0 mbar N_2O, 1.0 mbar Ar, room temperature) over Rh/Al_2O_3 as measured by a mass spectrometer connected to the XPS chamber. Catalysis was performed after different pre-treatment conditions: _3 SCR after 200 °C reduction. _5: SCR after 300 °C reduction. _6: 2nd SCR after _5. _8: SCR after plasma oxidation. _10: SCR after thermal oxidation at 375 °C.

In order to further confirm the role of Rh^0 as the species responsible for the H_2-SCR of N_2O, another experiment series was conducted. For this purpose, significantly higher temperatures were used for both reducing and oxidizing pretreatment conditions.

Figure 74 presents the Rh 3d core level spectra of the Rh/Al_2O_3 catalyst as synthesized (_1), after H_2-SCR (_2), followed by oxygen treatment at 380 °C (_3) and another H_2-SCR thereafter (_4). All samples exhibited only oxidized Rh without any indication of Rh^0. Also, no catalytic activity was observed for these materials. In addition, no significant structural changes of the catalyst occurred during these treatment steps, as the Rh intensity remained identical (Figure 76). After hydrogen treatment of sample _4 at 370 °C (_5), 77% of Rh was present as Rh^0. This proportion did not change upon performing SCR on this sample (_6).

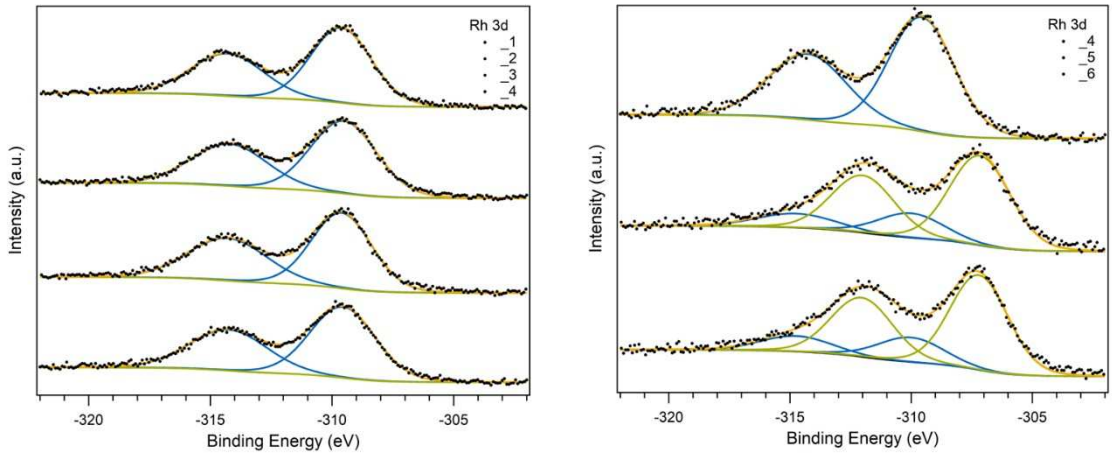

Figure 74: Rh 3d core levels of Rh/Al_2O_3 depending on the treatment conditions. Assignment: _1: as synthesized. _2: after SCR (1.5 mbar H_2, 1.0 mbar N_2O, 1.0 mbar Ar, room temperature). _3: After 50 mbar O_2, 380 °C. _4: After SCR (1.5 mbar H_2, 1.0 mbar N_2O, 1.0 mbar Ar, room temperature). _5: After 50 mbar H_2, 370 °C. _6: After SCR (1.5 mbar H_2, 1.0 mbar N_2O, 1.0 mbar Ar, room temperature).

Sample _6 was subsequently treated at 430 °C under an oxygen atmosphere (_7), leading to complete oxidation of Rh as shown in Figure 75. After performing a catalytic run on this material, the appearance of a shoulder at 307.2 eV indicates that the catalyst was partially reduced to metallic Rh during catalysis, resulting in a Rh^0 fraction of 23% Figure 76.

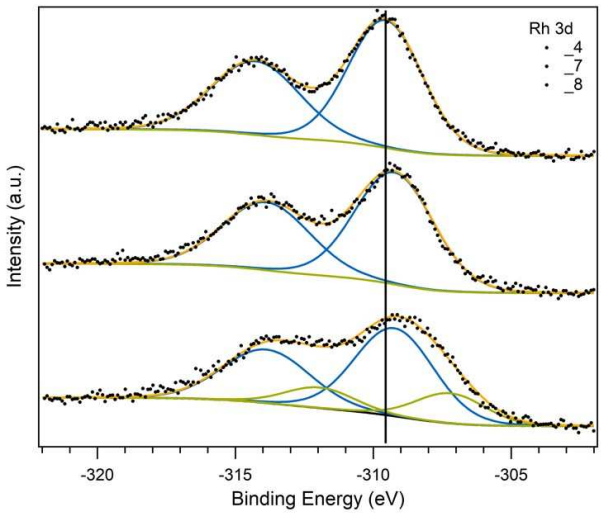

Figure 75: Rh 3d core levels of Rh/Al_2O_3 depending on the treatment conditions. Assignment: _4: After SCR (1.5 mbar H_2, 1.0 mbar N_2O, 1.0 mbar Ar, room temperature). _7: 50 mbar O_2, 430 °C. _8: After SCR (1.5 mbar H_2, 1.0 mbar N_2O, 1.0 mbar Ar, room temperature).

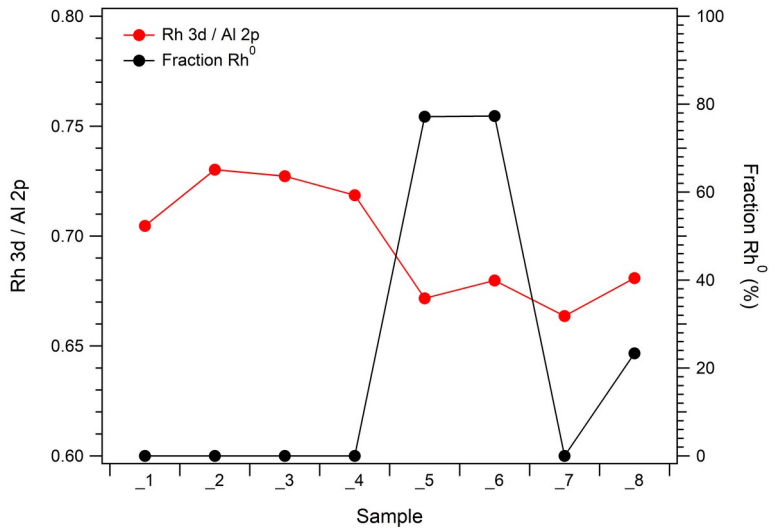

Figure 76: Fraction of Rh^0 and Rh 3d / Al 2p intensity ratios depending on the treatment conditions. Assignment: _1: as synthesized. _2: after SCR (1.5 mbar H_2, 1.0 mbar N_2O, 1.0 mbar Ar, room temperature). _3: After 50 mbar O_2, 380 °C. _4: After SCR (1.5 mbar H_2, 1.0 mbar N_2O, 1.0 mbar Ar, room temperature). _5: After 50 mbar H_2, 370 °C. _6: After SCR (1.5 mbar H_2, 1.0 mbar N_2O, 1.0 mbar Ar, room temperature). _7: 50 mbar O_2, 430 °C. _8: After SCR (1.5 mbar H_2, 1.0 mbar N_2O, 1.0 mbar Ar, room temperature).

Clear differences in the catalytic performance depending on the pretreatment conditions of the catalyst can be seen Figure 77. No catalytic activity was observed for the catalyst in its synthesized state (_2) and oxygen-treated state after this catalytic test (_4). The highest reactivity was observed for sample _6, which was tested after hydrogen treatment at 370 °C. Sample _8, referring to the sample after re-oxidation at 430 °C, showed catalytic activity in contrast to the other oxidized samples, albeit lower than the pre-reduced sample.

Summarizing all investigations, it can be stated that Rh/Al_2O_3 in its synthesized form does not show any catalytic activity. After reduction in H_2 at elevated temperatures, metallic Rh appears. The catalytic activity scales with the fraction of Rh^0 in most cases. Re-oxidized samples are catalytically active after a starting period. After reaction, a significantly increased fraction of metallic Rh is found, which clearly indicates that the presence of Rh^0 is required for any catalytic activity.

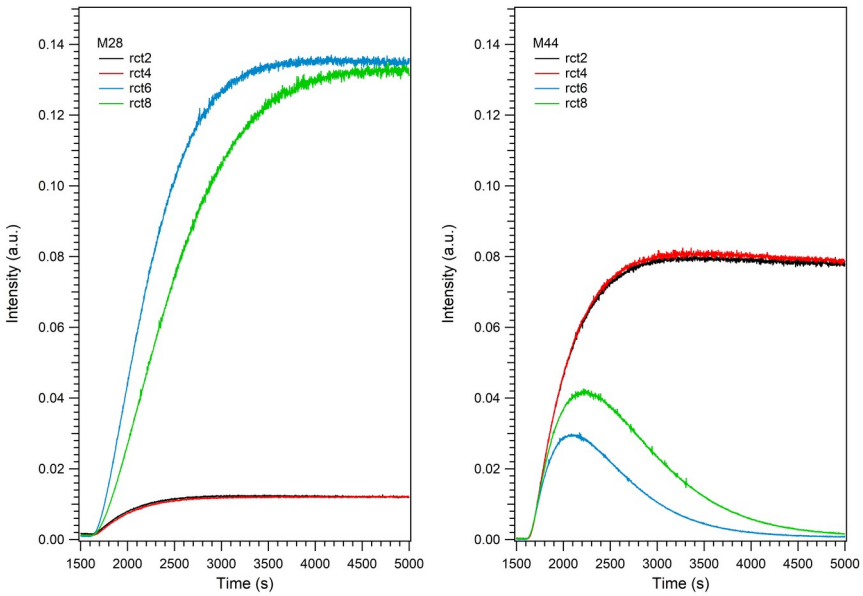

Figure 77: Comparison of the evolution of m/z 28 (left) and m/z 44 (right) during SCR (1.5 mbar H_2, 1.0 mbar N_2O, 1.0 mbar Ar, room temperature) over Rh/Al_2O_3 as measured by a mass spectrometer connected to the XPS chamber. Catalysis was performed after different pre-treatment conditions: Rct2: as synthesized. Rct4: After 50 mbar O_2, 380 °C. Rct. 6: After 50 mbar H_2, 370 °C. Rct. 8: After 50 mbar O_2, 430 °C.

4.4.2 XPS investigations on Rh/CeO_2

Further XPS investigations were conducted on Rh/CeO_2 in order to examine the effects of a reducible catalyst. CeO_2 is particularly relevant in this context, since its potential contribution as an active component is well-known in literature, with oxygen vacancies acting as N_2O adsorption sites.[243]

Interestingly, the catalyst was highly active in its synthesized state, which is in striking contrast to Rh/Al_2O_3. This can likely be attributed to the higher reducibility of Rh/CeO_2, which was also observed in the TPR measurements of the catalysts (Figure 54). Comparison of the Rh 3d core levels before and after the catalytic run indicated a shift to lower binding energies, corresponding to the formation of Rh^0 upon catalysis (Figure 78, left side). However, the data is rather noisy with low Rh 3d intensity, which impedes reliable interpretation. Fitting the Ce 3d spectra before and after catalysis (Figure 78, right side) revealed a clear increase of the Ce^{3+}/Ce^{4+} fraction from 18.8% to 23.4%, showing that the CeO_2 support is partially reduced during catalysis and potentially also participates in the catalytic reaction. Two catalytic runs were conducted at room temperature under different partial pressures of the reactive gases. The first run was performed with 1.5 mbar H_2, 1.0 mbar N_2O, and 1.0 mbar Ar (Figure 79, left side), while the second one was performed with 15 mbar H_2, 15 mbar N_2O, and 1 mbar Ar (Figure 79, right side). The catalyst was highly active in both cases, as shown by the immediate formation of N_2 and H_2O and the early maximum of the N_2O concentration (Figure 79).

In addition to the catalytic performance, the heat generated from the catalytic reaction was investigated exemplarily for Rh/CeO_2, as this catalyst was highly active at room temperature in the in situ XPS chamber. Significant increases of the sample holder temperature took place during the reaction (marked as red curve in Figure 79). For low partial pressures of the reactive gases, a temperature increase of 7 K was observed (Figure 79, left side), while the temperature of the sample holder even went up by 60 K under higher partial pressures (Figure 79, right side). This is due to the high reaction enthalpy of the reaction and shows that heat release is a highly relevant factor in this catalytic reaction.

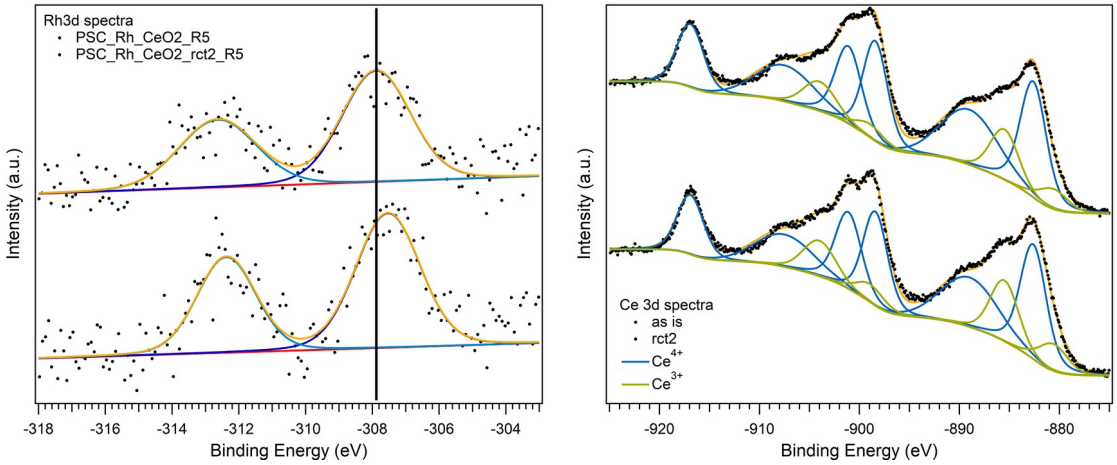

Figure 78: Left: Rh 3d core levels of Rh/CeO_2 as synthesized (Top) and after SCR (Bottom)(1.5 mbar H_2, 1.0 mbar N_2O, 1.0 mbar Ar, room temperature). Right: Ce 3d core levels of Rh/CeO_2 as synthesized (Top) and after SCR (Bottom)(1.5 mbar H_2, 1.0 mbar N_2O, 1.0 mbar Ar, room temperature).

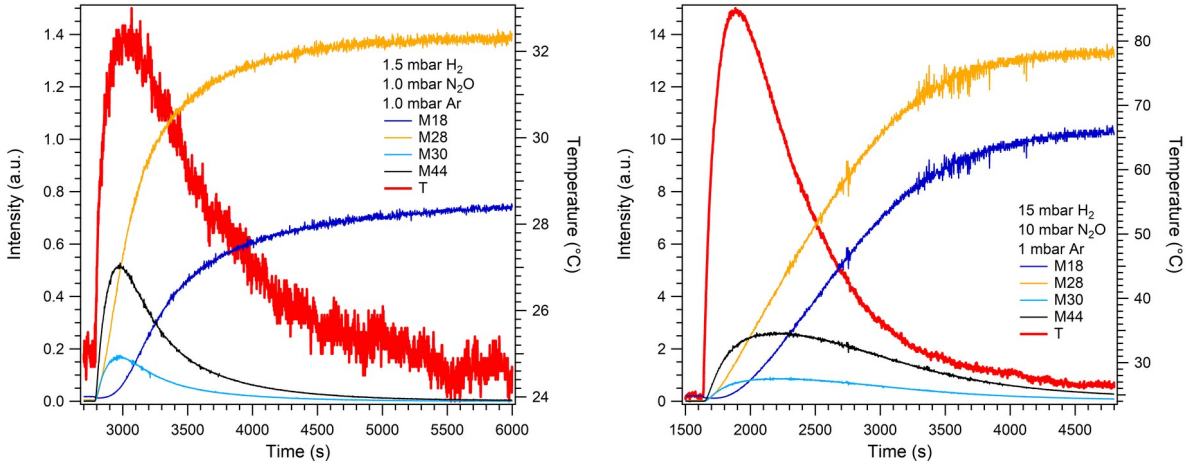

Figure 79: Evolution of the sample holder temperature (red) and the intensities of m/z 18, m/z 28, m/z 30 and m/z 44 over time during SCR over Rh/CeO_2 as measured by a mass spectrometer connected to the XPS chamber. Left: SCR with 1.5 mbar H_2, 1.0 mbar N_2O and 1.0 mbar Ar. Right: SCR with 15 mbar H_2, 10 mbar N_2O and 10 mbar Ar.

4.5 Discussion

4.5.1 Discussion on mechanistic aspects and heat dissipation in the catalytic reduction of N_2O by H_2

In contrast to the N_2O decomposition, the mechanism of N_2O reduction by H_2 is significantly less studied. However, it is generally agreed that it proceeds via a similar pathway. The decomposition of N_2O involves three elementary steps (Eq. 1, 2 and 3), with * representing a catalytically active site.[244],[245],[246],[247],[248],[249],[250]

$$N_2O + * \longrightarrow N_2 + O_{ads} \quad \text{(Eq. 1)}$$

$$2\ O_{ads} \rightleftharpoons O_2 + 2* \quad \text{(Eq. 2)}$$

$$N_2O + O_{ads} \longrightarrow N_2 + O_2 + * \quad \text{(Eq. 3)}$$

Scheme 19: General reaction mechanism for the catalytic decomposition of N_2O.[244],[245],[246],[247],[248],[249],[250]

The first elementary step (Eq. 1), the adsorption and dissociation of N_2O to N_2 and O_{ads}, also takes place in the reduction of N_2O by H_2, while the further steps are different. Instead of O_2, water is formed and desorbs from the active sites. As shown by mass spectrometry in the in situ XPS experiments (see 4.4) only H_2O and no O_2 was the product of reduction besides N_2.
Carabineiro and Nieuwenhuys investigated the reduction of N_2O by H_2 on the Ir(110) surface under ultra-high vacuum conditions and found oscillations in the reaction rate.[208] The concentration of N_2O oscillated in counterphase to that of N_2, and the peaks in H_2O production appeared with a delay relative to the peaks in N_2 formation. The authors attributed this relationship to differing rates of O_{ads} removal by reactive H_{ads} and the impact of the surface coverage with O_{ads} on the adsorption and dissociation of N_2O (Eq.1). A high surface coverage of O_{ads} results in a decline of the rate of dissociative adsorption of N_2O as the adsorption sites are blocked. When O_{ads} is released in the form of water, the rate of the dissociative adsorption of N_2O increases again, leading to constantly oscillating behavior. Based on these findings, Carabineiro and Nieuwenhuys proposed the following reaction mechanism (Scheme 20, Eq. 4 - 6):

$$H_2 + 2* \longrightarrow 2\ H_{ads} \quad \text{(Eq. 4)}$$

$$N_2O + * \longrightarrow N_2 + O_{ads} \quad \text{(Eq. 5)}$$

$$O_{ads} + 2\ H_{ads} \longrightarrow H_2O + 2* \quad \text{(Eq. 6)}$$

Scheme 20: Reaction mechanism for the catalytic reduction of N_2O by H_2 on the Ir(110) surface proposed by Carabineiro and Nieuwenhuys.[208]

As shown by the results of this chapter, the reduction of N_2O by H_2 can be performed at extraordinarily low temperatures, even clearly below room temperature. This is a striking difference to the catalytic N_2O decomposition. As a comparison, Pekridis *et al*. reported a T_{50} of around 350 °C at a GHSV of 35,000 h^{-1} for a Pd/Al_2O_3 catalyst (2 wt.-% Pd), and Richards *et al.* reported a T_{50} of even around 550 °C at a GHSV of 76,690 h^{-1} for different Pd/Al_2O_3 catalysts.[251],[252] In contrast, this study observed a T_{50} of -27 °C for Pd/Al_2O_3, demonstrating that the presence of H_2 is highly beneficial. There is strong evidence that this effect results from improved removal of adsorbed oxygen from the active sites. In fact, Haq and Hodgson reported rapid N_2O dissociation on the Pd(110) surface even at 85 K.[253] However, the adsorbed oxygen remained on the surface and caused a strong decrease in the dissociation probability with further N_2O uptake, leading to only molecular N_2O adsorption at some point. Similarly low temperatures for N_2O dissociation were also reported for other metal surfaces, such as Ru(001) and Cu(110).[254],[255],[256] It is generally agreed that after dissociation, N_2 desorbs readily while oxygen remains adsorbed on the metal surface. The addition of a reducing agent, therefore, helps to facilitate the removal of adsorbed oxygen. This effect has been documented for a variety of reducing agents, including carbon monoxide and hydrocarbons such as propane, as the N_2O conversion was substantially enhanced in their presence.[251],[252],[257],[258] The role of the reducing agent was typically understood as scavenging adsorbed oxygen and thereby increasing the accessibility for N_2O dissociation on the active sites.[251] This also indicates that the rate determining step in N_2O decomposition over metal catalysts is, in many cases, the recombination of adsorbed oxygen to form O_2 and its desorption.

Hydrogen as a reducing agent received significantly less attention, with only very few studies; however, it was shown to enable conversion of N_2O at temperatures far lower than with any other reducing agent. Gluhoi *et al.* reported high N_2O conversion over supported gold catalysts with the presence of H_2, reaching a T_{50} of 52 °C at a WHSV of 9000 mL h^{-1} g^{-1}.[259] Roy *et al.* also reported low temperature N_2O conversion by H_2 over precious metal substituted TiO_2 catalysts, with a T_{50} of 52 °C at a GHSV of 43,000 h^{-1} for a $Ti_{99}Pd_{0.01}O_{2-\delta}$ catalyst.[207]

The fact that stable N_2O conversion could be achieved even at only -70 °C in the present study raises the question, how the reaction and also water desorption can take place at such an extraordinarily low temperature. An important aspect concerning N_2O decomposition and, in particular, H_2-reduction of N_2O is the extremely high exothermicity of these reactions, with a ΔH of -82.1 kJ/mol (at 298 K) for N_2O decomposition and even -323.3 kJ/mol (at 298 K) for H_2-SCR. Upon splitting of the N_2-O bond on the palladium surface, a high amount of energy (about 2 eV) is released.[260] Conventionally, it is assumed that this energy is quasi-instantaneously dissipated away and will not affect the kinetics of the following reaction steps.[210],[212] However, a large amount of literature suggests a more complex situation. The concept of so-called “hot-adatoms” is frequently discussed, referring to thermally non-equilibrated surface species that result from an exothermic bond cleavage or formation.[210],[261],[262], For example, Wintterlin *et al.*

showed for the dissociative O_2 adsorption on Pt(111) that adsorbed oxygen after dissociation can travel a few lattice constants across the surface before reaching a fixed position, which provides evidence for “hot-oxygen”.[263] Theoretical investigations of energy dissipation on metal surfaces also predict the existence of “hot” adsorbates and question the prevalent assumption of instant thermalization of reaction enthalpies.[210],[211],[212]

The participation of hot-oxygen in the N_2O decomposition and N_2O reduction was also proposed in several studies. Horino *et al.* observed inclined N_2 and O_2 desorption from Pd(110) after N_2O dissociation, which they ascribed to interactions of hot-oxygen.[260] Nobukawa *et al.* investigated N_2O reduction by CH_4 over Fe-zeolite catalysts and proposed that reactive, nascent oxygen transients play an important role in the activation of CH_4.[264] Burch *et al.* investigated pulsing of N_2O and H_2 over Pt/SiO_2 and reported a clearly higher catalytic activity when N_2O and H_2 was present simultaneously compared to a sequential pulsing of N_2O and H_2.[209] This was attributed to the formation of hot-oxygen after N_2O dissociation, which could react directly with adsorbed hydrogen. It was assumed that when the hydrogen pulses were separated from the N_2O pulses, the excess energy of hot-oxygen was already dissipated into the system before hydrogen arrived on the active sites, leading to a lower reactivity of adsorbed oxygen with hydrogen and, in turn, less water formation and desorption.[209]

The effect of hot-ad-atoms on the kinetics of H_2-SCR of N_2O may also explain the extraordinarily low temperatures for conversion as observed in the present study. Another indication may be regarding the related catalytic reaction of H_2 with O_2, which is also referred to as the catalytic oxidation of hydrogen. It is likely that both reactions share a similar or even the same mechanism for the formation of water, as both reactions involve the presence of adsorbed hydrogen and adsorbed oxygen. In principle, the elementary reactions for water formation from adsorbed hydrogen (H_{ads}) and adsorbed oxygen (O_{ads}) can be described by the following equations (Scheme 21, Eq. 7 – 9):[265]

$$O_{ads} + H_{ads} \rightleftharpoons OH_{ads} \quad \text{(Eq. 7)}$$

$$OH_{ads} + H_{ads} \rightleftharpoons H_2O_{ads} \quad \text{(Eq. 8)}$$

$$2\ OH_{ads} \rightleftharpoons H_2O_{ads} + O_{ads} \quad \text{(Eq. 9)}$$

Scheme 21: Elementary reactions for the formation of water from adsorbed hydrogen (H_{ads}) and adsorbed oxygen (O_{ads}) in the catalytic reaction of H_2 with O_2.[265]

However, the topic of the precise contributions of water forming reaction steps is highly complex and, in fact, still poorly understood, see Borodin *et al.* for a detailed description.[265] In particular, it appears that the reaction mechanism can be influenced by factors such as the temperature and the surface coverage of H_{ads} and O_{ads}.[265] Investigations of the catalytic hydrogen oxidation under ultrahigh vacuum showed that this reaction could be performed at

temperatures far below room temperature.[266],[267],[268] Interestingly, below the water desorption temperature, which was about 170 K under these conditions, different kinetic behavior was observed than above that temperature. This was explained by the reaction of water with O_{ads}, leading to an autocatalytic process (Scheme 22, Eq.10).[266]

$$O_{ads} + H_2O_{ads} \longrightarrow 2\ OH_{ads} \qquad \text{(Eq. 10)}$$

Scheme 22: Reaction of adsorbed water with adsorbed oxygen.[266]

Remarkably, Borodin *et al*. found a drastic discrepancy between theoretical models and high temporal resolution measurements of water formation on Pt(111), with the experimentally observed rate exceeding DFT predictions by four orders of magnitude.[265] The authors concluded that there must be a significant lack of understanding of the fundamentals of the reaction mechanism.[265] While there are different possible effects that might be responsible, the role of hot-ad-atoms could potentially be a factor.

Somewhat simplified, the hypothetical effect of hot-ad-atoms can be illustratively described as the presence of atomic hot spots. In that sense, the actual temperature of the active sites of a catalyst may differ from the catalyst as a whole. Unrelated to this potential scenario, temperature differences may also be present on a slightly more macroscopic scale. This may be relevant in the case of supported catalysts, which in principle can be regarded as an active metal nanometer-scale crystallite with high thermal conductivity on the surface of a support particle with typically low thermal conductivity (see Table 13). It may be that the temperature of the metal nanoparticle is significantly higher than that of the adjacent support material due to this barrier of heat transfer. It is plausible that a support material with higher thermal conductivity can more effectively lower the temperature of the metal particles. Experimental observations of this study point in this direction. Only a very small temperature increase of the catalyst bed (<5 K) was observed under catalytic conditions as measured by a thermocouple in contact with the catalyst powder. However, there was a significant performance gap of the catalysts supported on oxides and on materials with higher thermal conductivity, i.e., SiC and nanodiamond. This would be in line with a higher extent of metal-support heat transfer, resulting in a lower effective temperature of the metal and lower N_2O conversion.

Further evidence for this role of heat transfer is provided by the very long time periods (up to several hours) required for the N_2O conversion to stabilize after a change in the cooling bath temperature.

4.5.2 Discussion on the influence of alkali metals and halides

The palladium catalysts were very sensitive to the presence of promoters. While the presence of alkali metals was shown to be beneficial, even the slightest presence of chloride, fluoride, and sulfide in the catalyst drastically impaired the performance of the catalysts. These observations for the H_2-reduction of N_2O were in good agreement with other similar catalytic reactions. Yentekakis *et al.* investigated the influence of chloride residues on Pt/Al_2O_3 catalysts in the reduction of NO by propane.[269] The authors reported significantly worse performance for catalysts prepared by impregnation using H_2PtCl_6 compared to catalysts prepared from a chlorine free precursor. Similarly, Yuzaki *et al*. also found a severe suppression of the catalytic activity of Rh/Al_2O_3 prepared from $RhCl_3$ in the decomposition of N_2O.[270]

On the other hand, the beneficial effect of alkali metal promotion was also reported in the literature for the catalytic N_2O decomposition. This was shown for a large variety of catalyst systems, including metal oxides[73],[271] and noble metals.[272],[273],[274] In addition, other electropositive promoters, such as alkaline earth, also resulted in an improvement of the catalytic activity.[235] The effectiveness of alkali metal promotion was typically influenced by factors such as the type of alkali metal, the promoter loading, the alkali metal precursor, the synthesis procedure, and others.[73],[275],[276],[277] Besides N_2O decomposition, positive effects of alkali metal promotion were also demonstrated for N_2O reduction. Pekridis *et al.* investigated N_2O reduction by C_3H_8 and reported a strong enhancement of the catalytic performance for K-promoted Pd/Al_2O_3 compared to un-promoted Pd/Al_2O_3.[278],[279]

Both the influence of halides and alkali metals on the catalytic activity can likely be attributed to electronic effects. The binding and activation of N_2O on metal centers, which leads to dissociation into N_2 and adsorbed oxygen as described earlier by Eq. 1, is well established in the literature. N_2O can be bound on the metal centers in different modes, which depend in principle on the type of metal and the surface characteristics.[280] Theoretical investigations calculated that adsorption of N_2O on the Pd(110) surface takes place via its terminal N-atom in a tilted end-on fashion or also in a horizontal fashion.[281],[282] It is generally assumed that N_2O dissociation then proceeds due to an electron transfer from the metal centers to the $3\pi^*$ antibonding orbitals of N_2O, resulting in the destabilization of the N-O bond and its rupture.[280],[281],[283] See Figure 80 for a visualization of the N_2O frontier orbitals and Figure 81 for a visualization of the bonding interactions between N_2O and a metal ion.

Modifying the electronic structure of the metal, in this case Pd, therefore strongly influences these electronic interactions. This can effectively be achieved by alkali metal promoters, which increase the electron density of Pd.[278] In turn, stronger electron transfer of Pd into the antibonding orbitals of N_2O is expected, leading to facilitated scission of N_2O. On the other hand, the introduction of electronegative species such as halides hinders the dissociation of N_2O on the Pd surface.

The addition of alkali promoters can therefore be considered a useful tool for optimizing the catalytic performance in the H_2-reduction of N_2O, even though this effect was rather small with only a -10 °C shift of the T_{50}. This is likely due to the unpromoted Pd/Al_2O_3 being extremely active already, which does not leave much room for improvement. Moreover, it appears that increasing the alkali metal content also leads to increased coverage of Pd surface sites by the promoter, which counteract the electronic effects. The Pd to alkali metal ratio, therefore, needs to be adjusted for optimum catalytic activity.

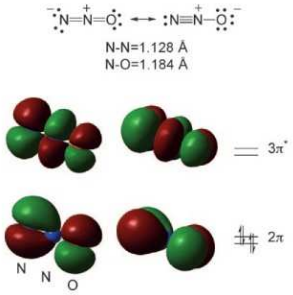

Figure 80: Top: The most relevant resonance structures of N_2O. Bottom: Visualization of the computed N_2O frontier orbitals. Figure published by Tolman (Figure 1, page 1019).[280]

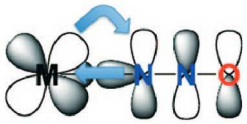

Figure 81: Visualization of the bonding interactions between N_2O and a metal ion (M). Figure published by Tolman (Figure 4, page 1020).[280]

4.6 Conclusion

The selective catalytic reduction of N_2O by hydrogen was shown to be an effective potential strategy for N_2O abatement. Quasi *in situ* XPS measurements demonstrated that the catalytically active sites are metallic and that reduction of the noble metals is required. The initial, as synthesized, state of Rh/Al_2O_3 required high temperatures for effective reduction of oxidic Rh. In the case of Rh/CeO_2, the catalyst was active even in its as-synthesized state, due to easier reducibility. The content of Ce^{3+} increased after catalysis, indicating that the CeO_2 support may also take part in the reaction as adsorption sites to some extent.

In the fixed-bed reactor, N_2O SCR by H_2 proceeded even at temperatures clearly below room temperature. Supported Rh and Pd catalysts proved to be significantly more effective than Ru catalysts. The effect of structural properties of the catalyst on the catalytic activity was investigated for supported Pd catalysts. Precipitation deposition as a synthesis method proved to be more effective than incipient wetness impregnation, due to significantly higher Pd dispersions. The choice of the Pd precursor used in the synthesis also played an important role, mostly due to dispersion effects and poisoning of active sites in the case of palladium chloride. The addition of Na and K as alkali metal promoters improved the catalytic performance of Pd/Al_2O_3. Moreover, the catalyst support strongly affected the catalytic activity by impacting the Pd dispersion and poisoning effects in the case of AlF_3 and ZnS. Furthermore, the involvement of oxygen from the support appears to play a role in the catalytic process; however, more in-depth investigations are necessary for improved clarification.

As an additional factor, the thermal conductivity of the support appears to play a role due to the strong exothermicity of the reaction. It may be that the actual temperature of the noble metal particles is significantly higher than that of the catalyst bed from a macroscopic perspective. In addition, literature studies suggest a high complexity of the reaction mechanism of H_2-SCR of N_2O and potentially a fundamental lack of understanding, possibly due to the involvement of thermally non-equilibrated species in the form of hot ad-atoms. This effect may be responsible for enabling the reaction at such extraordinarily low temperatures. However, more-in-depth experimental and theoretical research is required for improved insight and further validation of these hypotheses.

4.7 Disclaimer

Section 4.4 (XPS investigations on the catalytic reduction of N_2O by H_2) is based on XPS experiments conducted by Tim Kratky and Sebastian Günther. In addition to performing the XPS experiments, Tim Kratky and Sebastian Günther performed processing and visualization of the data, including creation of the figures of this section (Figure 66 – 79). Tim Kratky and Sebastian Günther have approved the use of these data and figures for inclusion in this dissertation.

5

Summary

As a promising measure to lower CO_2 emissions, the transition from fossil fuels to a more sustainable hydrogen economy is gaining increasing importance. This shift raises the need for efficient and low-cost catalyst materials for hydrogen activation and also can open avenues for novel processes due to increased hydrogen availability and infrastructure. In this context, the catalytic abatement of the potent greenhouse gas nitrous oxide using hydrogen presents a promising approach for improved efficiency. Accordingly, this dissertation pursues two main objectives: (i) the exploration of tungsten carbide catalysts as potential substitutes for platinum in hydrogenation reactions (Chapter 2 and Chapter 3), and (ii) the investigation of the selective catalytic reduction (SCR) of N_2O with hydrogen (Chapter 4).

Chapter 2 described the synthesis of bulk tungsten carbide catalysts from bulk tungsten oxide using a less-investigated two-step approach with separated reduction and carburization. Phase pure W_2C and WC bulk catalysts were obtained using this literature-based method, which was modified and optimized in this thesis. Higher hydrogenation activity was observed for W_2C compared to WC in the catalytic hydrogenation of butyraldehyde. This is in accordance with earlier theoretical investigations as reported in the literature.

Chapter 3 extended the synthesis approach of Chapter 2 to supported catalysts. It was observed that the synthesis conditions as well as the structure of the WO_3 based precursors influence the product characteristics of both reduction and carburization. Higher dispersion of W-species and lower temperature were found to benefit the formation of the metastable phases β-W and W_2C, which can become thermodynamically stable through surface energy contributions. A clear, although not simple, correlation of the W_2C content and the catalytic activity in hydrogenation reactions was found. In addition, higher tungsten carbide dispersion generally led to higher catalytic activity. However, it has to be considered that the tungsten carbide dispersion and W_2C content are also correlated, leading to a complex overlay of multiple effects that determine the activity of the catalysts.

Chapter 4 explored the utilization of hydrogen for the selective catalytic reduction of N_2O. Quasi *in situ* XPS measurements confirmed that the catalytically active sites are metallic and reduction of the active metals is required before N_2O conversion can take place. In the fixed-bed reactor, complete N_2O conversion by H_2-SCR using a WHSV of 12 000 $mL g^{-1} h^{-1}$ could be achieved even at temperatures far below room temperature. In the context of structure-activity relationships, a strong influence of various aspects was found. The beneficial effect of alkali metals and the detrimental effect of halides and sulfide can be explained by changes in the electronic properties of the noble metal, which influences the electronic interactions with N_2O. Uncertainties regarding the role of heat dissipation on catalyst surfaces were discussed. The extraordinarily low temperatures observed for N_2O conversion might be possible due to a certain temperature gradient within the catalyst, with “hot-ad-atoms” and/or “hot nanoparticles” exhibiting low-scale hotspots.

This thesis contributes to the advancement of catalytic materials for hydrogen activation, with tungsten carbide as an alternative to noble metals, in particular platinum. Improved understanding of the solid-state reactions in the synthesis of tungsten carbide and how they shape the catalytic behavior was achieved. The synthesis approach using decoupled reduction and carburization showed high potential for catalytic applications, as it allows high phase selectivity to W_2C. In addition, significantly lower synthesis temperatures can be achieved, which increases the applicability of tungsten carbide as catalyst, as in situ synthesis inside an industrial reactor may be possible. Moreover, lower temperatures can help to minimize sintering of secondary active metals such as nickel, which are frequently combined with tungsten carbide. Further research can be based on the results of this thesis and can further optimize the synthesis conditions for improved catalytic performance.

This thesis also contributes to the exploration of H_2 utilization in the context of N_2O abatement, which proved to be a highly effective way to achieve high N_2O conversion, even at temperatures clearly below room temperature. The observations of this thesis, in conjunction with literature reports, imply a lack of understanding of the role of heat transfer in highly exothermic reactions. The combination of more advanced experimental model systems and theoretical investigations is required for addressing these fundamental complexities.

6

Experimental

6.1 Materials

Chemicals were obtained from commercial suppliers and used without further purification. *Aerosil® 90* was obtained from *CSC JÄKLECHEMIE GmbH & Co. KG*. Gases were purchased from *Westfalen AG* (Germany) with the following purities: 99.2% for N_2O in He, 99.5 % for CH_4, 99.996 % for He, and 99.999 % for H_2, Ar, and N_2.

6.2 Synthesis of precursor and catalyst materials

6.2.1 Synthesis of bulk tungsten carbide catalysts

Bulk tungsten carbide catalysts were synthesized using a two-step approach. First, WO_3 was reduced to metallic tungsten, which was converted to tungsten carbide in a second step. step. A ceramic combustion boat with 65 mg of the tungsten oxide bulk precursor was introduced into the center of a horizontal tube furnace from the company *Gero*. Both the reduction of WO_3 and the carburization of tungsten metal were performed isothermally with heating to the reaction temperature under inert gas before introducing hydrogen or hydrogen/methane, respectively. The carburization was conducted immediately after the reduction, without exposure of the formed tungsten to air.

WO_3 was reduced at 550 °C, 700 °C, or 800 °C at ambient pressure under constant hydrogen flow of 100 mL/min (30 min for 700 °C and 800 °C, 60 min for 550 °C). The reaction progress was analyzed by mass spectrometry of the effluent gas stream with a *ThermoStar* (*Pfeiffer*). Carburization was performed using gas mixtures of methane and hydrogen (CH_4 to H_2 ratio of 2:1 for 550 °C, CH_4 to H_2 ratio of 1:4 for 700 °C and 800 °C). The carburization duration was 2.5 h for 550 °C and 4 h for 700 °C, and 800 °C. Directly after the synthesis, the furnace tube was flushed with inert gas for 15 min and then with hydrogen in order to remove excess carbon deposits from the product surface (100 mL/min). The hydrogen flow was continued until the CH_4 signal in the online mass spectrometry stabilized (see figure S1). Afterwards, the products were allowed to cool with constant Ar flow and subsequently moved into a glove box. Different aliquots of the tungsten sample created by reduction at 550 °C were carburized at 550 °C, 700 °C, or 800 °C. The sample reduced at 700 °C was carburized at 700 °C, and the sample reduced at 800 °C was carburized at 800 °C.

6.2.2 Synthesis of WO_3/SiO_2 precursors

SiO_2 supported WO_3 based precursors were synthesized by incipient-wetness impregnation. Pyrogenic silica powders of the type *Aerosil®* with different specific surface areas were used: *Aerosil® 90* with 90 m^2/g, *Aerosil® 200* with 200 m^2/g, and *Aerosil® 380* with 380 m^2/g. Prior to

impregnation, the silica powders were agglomerated. This was performed by suspension of the powders in water, followed by calcination of this suspension at 450 °C for 6h (5 K/min heating rate). The resulting materials were ground and sieved to a fraction of 100-300 µm, followed by calcination at 700 °C for 8h (10 K/min heating rate). Incipient-wetness impregnation was performed by stepwise addition of aqueous solutions of ammonium metatungstate to the silica powders, with vigorous mixing after each addition. The resulting products were then thermally treated for 2 h at 60 °C, for 6 h at 110 °C, and finally at 450 °C for 6 h.

6.2.3 Synthesis of supported tungsten carbide catalysts

Supported tungsten carbide based catalysts were prepared using a two-step approach. In the first step, the tungsten oxide based precursors (prepared by incipient-wetness impregnation, see 6.2.2) were reduced to metallic tungsten precursors, which were converted to tungsten carbide in a second step. For each WO_3 based precursor, a mass corresponding to 65 mg of pure WO_3 was added on a ceramic combustion boat and introduced into the center of a horizontal tube furnace from the company *Gero*. The reduction of WO_3 and the carburization of tungsten metal were both performed isothermally, with heating to the reaction temperature under an inert atmosphere prior to the introduction of hydrogen or hydrogen/methane, respectively. The carburization was carried out directly after the reduction, without exposure of the formed tungsten to air. The WO_3 precursors were reduced at 550 °C, 700 °C, or 800 °C at ambient pressure by applying a constant hydrogen flow of 100 mL/min (approximately 30 min for 700 °C and 800 °C, 60 min for 550 °C). The exhaust gas stream was analyzed using a *ThermoStar* (*Pfeiffer*) mass spectrometer to monitor the reaction progress. Complete reduction to metallic tungsten was considered complete when water formation was no longer detected. Carburization of the tungsten metal precursors was carried out using gas mixtures of methane and hydrogen (CH_4 to H_2 ratios of 2:1, 1.5:1, 1:1, and pure CH_4 for 550 °C, CH_4 to H_2 ratio of 1:4 for 700 °C and 800 °C). Directly following synthesis, the furnace tube was flushed with inert gas for 15 minutes, followed by hydrogen (100 mL/min) at the respective carburization temperature to remove excess carbon deposits from the product surface. Hydrogen flow was maintained until the CH_4 signal monitored by online mass spectrometry stabilized (see figure S1). Afterwards, the product materials were cooled down under continuous argon flow and subsequently transferred to a glove box.

The catalysts to be tested in the hydrogenation of toluene were prepared in a vertical stainless steel reactor (1/4 inch outer diameter). Constant amounts of the WO_3-SiO_2 precursor (50 mg) were layered between quartz wool. The sample was heated under 100 mL/min argon flow to 550 °C with a heating rate of 10 K/min. Subsequently, the WO_3-SiO_2 was reduced by a 100 mL/min hydrogen flow at 550 °C under isothermal conditions for 1 h, as monitored by a mass spectrometer (*Pfeiffer OMNIStar GSD 320 02)* connected to the exhaust gas stream. Directly

after the reduction, the carburization gas mixture was introduced into the reactor at 550 °C, and carburization was continued for 1 h. This was followed by three minutes of hydrogen purge (100 mL/min) at 550 °C in order to remove excess carbon from the catalyst surface. The product was allowed to cool down under a 50 mL/min argon flow and subsequently tested in the hydrogenation of toluene without prior exposure to air.

6.2.4 Synthesis of supported metal catalysts used in the H_2-SCR of N_2O

The supported metal catalysts used in the H_2-SCR of N_2O were synthesized by two methods: Incipient-wetness impregnation and precipitation deposition.

Incipient-wetness impregnation was performed by weighing a support powder in a vial and stepwise addition of defined volumes of solutions containing precursor metal salts with a concentration adjusted to obtain catalysts with active metal content of 1 wt.-%. The total volume of added liquid was intended to be equivalent to the pore volume of the catalyst supports. Between each addition step, proper mixing was performed.

Precipitation deposition was performed using a modified synthesis approach based on Pearlman.[213],[214] The precipitation was carried out using a *Metrohm 906* titrator with a pH-electrode (*AVS-Ecotrode*), which was calibrated before use. Solutions of the precursor salts were added to aqueous suspensions of the support materials and stirred vigorously for 1 h. The pH of the solution was then gradually increased to pH 10 by adding an aqueous 10% NaOH solution under continuous mixing. After reaching the end point of the titration, the mixture was left stirring for 1 h. The product was filtered off and washed with deionized water (3-5 times 100 mL).

Unless stated otherwise, the same thermal treatment in an oven was applied for both catalyst synthesis methods: 60 °C for 2 h, 120 °C for 6 h, and 450 °C for 6 h.

6.3 Characterization of the materials

6.3.1 Elemental analysis

The elemental analysis was performed by the CRC analytic core facility of TUM. The quantification of tungsten was performed using an *Agilent Cary 100 UV-Vis spectrophotometer* after alkaline digestion. The quantification of the noble metals was carried out using an *Agilent Cary 100 UV-Vis spectrophotometer* or *via* flame atomic absorption spectrometry on an *Agilent 280FS AA* after acidic digestion.

6.3.2 XRD measurements

XRD measurements of the products were carried out on a *Rigaku MiniFlex 600-C* with Cu Kα radiation. Data were collected in a range of 15-70°2θ applying a 2θ step size of 0.01° and a scanning rate of 3°/min. The Scherrer formula was used for selected reflections to calculate the size of crystalline domains from the XRD patterns. The quantification of the phase content was performed by Rietveld refinement using the software *Profex*.[284] The fit was optimized by refining the parameters *k1* (crystallite size), *k2* (micro-strain), *B1* (crystallite size), and *GEWICHT* (grain-size weighting).

6.3.3 BET measurements

BET physisorption measurements for the determination of specific surface areas were conducted on a *Quantachrome NovaTouch LX*^{4} with N_2 at a temperature of -196 °C. Before the measurement, the samples were degassed at 120 °C for 3 h under vacuum. He (99.999 %) and N_2 (99.999 %) were used as gases. Sample amounts of 50 to 200 mg, depending on the availability, were used for the analysis.

6.3.4 SEM measurements

Scanning electron microscopy (SEM) images were acquired using a *Hitachi TM-1000* tabletop microscope.

6.3.5 TEM measurements

Transmission electron microscopy (TEM) images of supported tungsten carbide catalysts were acquired using a JEOL JEM-1400 plus microscope operated at 120 kV, equipped with a field emission gun and a RUBY CCD camera. Transmission electron microscopy (TEM) images of supported tungsten carbide catalysts were acquired using a *JEOL JEM-F200microscope* operated at 200 kV, equipped with a cold-field emission gun and a Gatan Metro electron counting detector. Powder samples were ultrasonically dispersed in ethanol, and a drop of the suspension was added onto a carbon-coated copper grid. Particle size analysis of the TEM micrographs was performed using the software *DigitalMicrograph* from *Gatan*.

6.3.6 Chemisorption measurements

For tungsten carbide catalysts, chemisorption of CO was performed in pulse mode on an *Autochem II (Micromeritics)* after *in situ* carbide synthesis with parameters replicating the syntheses in the horizontal tube furnace with conditions as close as possible. Pure CO (99.997%) was introduced in pulses using a 10 µL injection loop maintained at 110 °C. The adsorption temperature was 40 °C as controlled by a thermocouple in the catalyst bed.
For supported metal catalysts, chemisorption of H_2 was performed in pulse mode on an *Autochem II (Micromeritics)* at an adsorption temperature of 35 °C.

6.4 (*Quasi*) *in situ* investigations

6.4.1 *In situ* XRD measurements

In situ XRD measurements were performed on an *Empyrean* X-ray diffractometer from the company *Malvern Panalytical* using Cu Kα radiation. Data were collected in a range of 15-70°2θ using a 2θ step size of 0.01° and a scanning rate of 5.5°/min. The samples were measured in Bragg-Brentano geometry with a 10 mm slit and a 2.5° Soller slit at the beam side and a 2.5° Soller slit with a Kβ filter, and a programmable antiscattering slit at the detector side. The measurements were performed using an *Anton Paar XRK 900* reaction chamber, which was connected to the XRD instrument. A sample amount of 45 mg of the tungsten oxide bulk precursor or 70 mg was loaded onto a stainless-steel sample holder and inserted into the reaction chamber. Heating to the reaction temperatures was performed under inert gas flow with a heating rate of 10 K/min. After reaching the target temperatures, the system was held for 10 min to ensure thermal stabilization before initiating the reactions. Reduction was performed with a hydrogen flow of 100 mL/min. Carburization was carried out with methane-hydrogen mixtures (CH_4/H_2 = 2:1 at 550 °C and CH_4/H_2 = 1:4 at 700 °C).

6.4.2 *(Quasi) in situ* XPS measurements

Quasi in situ XPS measurements were carried out using a *Leybold-Heraeus LHS 10* equipped with a non-monochromatized Mg Kα source photoelectron spectroscopy. The catalyst powders were pressed into the cavities of a sample holder. Spectra were collected at a constant pass energy of 100 *eV*, corresponding to an energy resolution of ~1.1 eV. All measurements were performed under ultra-high vacuum conditions at pressures below 5×10^{-8} mbar. Different treatment conditions were applied, including heating of the catalysts, plasma oxidation, and introduction of gases with various partial pressures.

6.5 Catalytic tests

6.5.1 Catalytic hydrogenation of butyraldehyde

Testing of the tungsten carbide catalysts in the hydrogenation of butyraldehyde was performed in a 300 mL *Parr* minireactor. The reaction was carried out with 5 mL butyraldehyde, 100 mL ethanol as solvent, and 1.5 mL *n*-dodecane, serving as an internal standard. An excess of butyraldehyde was employed to ensure an extended period of linear 1-butanol formation (zero-order kinetics). Before adding 0.04-0.09 g of catalyst under inert conditions, the liquid reaction mixture was flushed with argon. The autoclave reactor was sealed, pressurized with hydrogen to 65 bar at ambient temperature, and stirring was only started after heating to the reaction temperature (200 °C). Samples of the liquid phase during the reaction were collected via a dip tube at the start and at subsequent intervals, with a total run time typically around 6 hours. The samples were analyzed using gas chromatography on an *Agilent 6890-N* instrument equipped with an automated injector and FID. Separation of the components was achieved with an *HP-1 MS* column under helium flow, applying the following temperature program: First, 50 °C was maintained for 3 min, followed by heating to 140 °C with a heating rate of 20 K/min and a final heating ramp to 270 °C using 30 K/min. The assignment of peaks and their retention times was validated with an *Agilent GC 7890B* gas chromatograph coupled to a *5977A* mass spectrometer and automated liquid sampling. The results were evaluated using response factors relative to n-dodecane (internal standard), which were established through calibration with pure substances. The catalytic hydrogenation activity was determined based on the 1-butanol formation rate.

6.5.2 Catalytic hydrogenation of toluene

Catalytic hydrogenation of toluene was performed right after the carbide synthesis in the same reactor. Liquid toluene was introduced into the reactor head using a *Legato 011 SS* syringe pump at a feed rate of 0.15 mL/h. The catalysis was run at an over pressure of 20 bar with a hydrogen flow of 75 mL/min corresponding to a hydrogen to toluene molar ratio of 142:1, a weight hourly space velocity (WHSV) of 2.6 h^{-1}, and a gas hourly space velocity (GHSV) of 450,000 h^{-1}. The composition of the product gas stream was determined using a gas chromatograph (*Varian CP3800*). The toluene conversion was calculated by the ratio of the peak areas of toluene at the catalysis temperature to the peak areas of toluene at 160 °C, where no conversion of toluene took place. The reactor was then heated to 230 °C for the isothermal investigation of the toluene conversion.

6.5.3 Selective catalytic reduction of N_2O by H_2

The selective catalytic reduction of N_2O by H_2 was investigated using a continuous flow fixed-bed reactor. The educt gas mixture was prepared by combining pure nitrogen as the carrier gas with 1 % N_2O in helium and 5 vol.-% hydrogen in nitrogen. The individual gas flow rates were controlled using mass flow controllers to obtain final concentrations of 1100 ppm nitrous oxide and 1500 ppm hydrogen. The resulting feed gas was introduced into the reactor at a total flow rate of 100 mL/min, corresponding to a weight hourly space velocity (WHSV) of 12,000 $mL \cdot g^{-1} \cdot h^{-1}$. The catalyst powder (0.5 g, 100-300 µm sieve fraction) was placed on a small layer of quartz wool in a U-tube glass or quartz reactor. In some cases, the reactor was equipped with a thermocouple (*Greisinger GmbH*) to determine the temperature of the catalyst bed. The effluent gas stream was analyzed online using Fourier transform infrared spectroscopy (FTIR) with a *Varian 660* spectrometer equipped with a gas cell (*Axiom Analytical*). Before the catalytic investigations, the catalysts were treated with nitrogen at 50-200 °C until no more water was detected in the effluent stream, as monitored by FT-IR. Heating was performed using a vertical oven (*HTM Reetz*).

The reaction gas mixture (1100 ppm N_2O, 1500 ppm H_2, with N_2 as carrier gas) was first introduced at room temperature; although no N_2O conversion was detected under these initial conditions, as described also in section 4.3. The reactor temperature was then increased in steps until noticeable N_2O conversion started. At each temperature step, the conversion continued to rise over time. When full conversion was achieved, the activation temperature was maintained for an extended period to ensure complete catalyst activation. The catalyst performance was subsequently assessed by stepwise variation of the reactor temperature to obtain temperature-activity curves. Cooling of the reactor was performed by placing the reactor in a dewar with a cold mixture of acetone or ethanol and liquid nitrogen. The temperature was adjusted depending on the amount of liquid nitrogen added.

6.6 Disclaimer

The experimental descriptions of this chapter are partially based on a manuscript published in *The Journal of Physical Chemistry C*, titled “Synthesis of Phase-Pure W_2C and WC by Separation of Reduction and Carburization and their Differing Performance as Hydrogenation Catalysts” with the following citation: [82]

Patrick Schlachta, Rolf E. Jentoft, Friederike C. Jentoft, Klaus Köhler, *The Journal of Physical Chemistry C*, **2025**, *129***,** 47, 20907-20921.
DOI: 10.1021/acs.jpcc.5c05153

The author of this dissertation (Patrick Schlachta) is also the first author of the manuscript. The contributions of Patrick Schlachta to the manuscript in the sense of the CRediT author statement definitions include conceptualization, investigation, methodology, validation, formal analysis, visualization and writing (original draft and editing). The content has been edited and restructured to some extent, to align with the format and context of this dissertation. All co-authors, that is Rolf E. Jentoft, Friederike C. Jentoft and Klaus Köhler have approved the use of the manuscript in this dissertation. The article is intended to be published as open access and is reused here for the purpose of this dissertation in accordance with the Creative Commons Attribution 4.0 International License (CC BY, see https://creativecommons.org/licenses/by/4.0/), which allows unrestricted reuse of the work in any medium or format, as long as appropriate credit is given to the original work.

Moreover, certain experimental descriptions are associated with a manuscript not yet submitted, see section 3.7.

7

References

[1] L. Kemp, C. Xu, J. Depledge, K. L. Ebi, G. Gibbins, T. A. Kohler, J. Rockström, M. Scheffer, H. J. Schellnhuber, W. Steffen, T. M. Lenton, *Proceedings of the National Academy of Sciences* **2022**, *119*, e2108146119.

[2] A. M. Oliveira, R. R. Beswick, Y. Yan, *Current Opinion in Chemical Engineering* **2021**, *33*, 100701.

[3] M. T. Ahad, M. M. H. Bhuiyan, A. N. Sakib, A. Becerril Corral, Z. Siddique, *Materials* **2023**, *16*, 6680.

[4] J. O. M. Bockris, *Science* **1972**, *176*, 1323-1323.

[5] S. González-Poggini, *International Journal of Hydrogen Energy* **2024**, *59*, 30-42.

[6] S. Wang, A. Lu, C.-J. Zhong, *Nano Convergence* **2021**, *8*, 4.

[7] L. Fang, X. Dong, H. Wang, M. Gong, *International Journal of Hydrogen Energy* **2025**, *162*, 150725.

[8] D. Haeseldonckx, W. D'haeseleer, *International Journal of Hydrogen Energy* **2007**, *32*, 1381-1386.

[9] G. AlZohbi, A. Almoaikel, L. AlShuhail, *Energy Reports* **2023**, *9*, 28-34.

[10] M. R. Usman, *Renewable and Sustainable Energy Reviews* **2022**, *167*, 112743.

[11] M. Ji, J. Wang, *International Journal of Hydrogen Energy* **2021**, *46*, 38612-38635.

[12] D. J. Durbin, C. Malardier-Jugroot, *International Journal of Hydrogen Energy* **2013**, *38*, 14595-14617.

[13] P. Preuster, A. Alekseev, P. Wasserscheid, *Annual Review of Chemical and Biomolecular Engineering* **2017**, *8*, 445-471.

[14] P. M. Modisha, C. N. M. Ouma, R. Garidzirai, P. Wasserscheid, D. Bessarabov, *Energy & Fuels* **2019**, *33*, 2778-2796.

[15] Y. Okada, E. Sasaki, E. Watanabe, S. Hyodo, H. Nishijima, *International Journal of Hydrogen Energy* **2006**, *31*, 1348-1356.

[16] J.-Y. Cho, H. Kim, J.-E. Oh, B. Y. Park, *Catalysts* **2021**, *11*, 1497.

[17] M. Gonda, M. a. Ohshima, H. Kurokawa, H. Miura, *International Journal of Hydrogen Energy* **2014**, *39*, 16339-16346.

[18] X. Ren, Y. Wang, A. Liu, Z. Zhang, Q. Lv, B. Liu, *Journal of Materials Chemistry A* **2020** *8*, 24284-24306.

[19] H. Liu, *Chinese Journal of Catalysis* **2014**, *35*, 1619-1640.

[20] P. Schwiderowski, H. Ruland, M. Muhler, *Current Opinion in Green and Sustainable Chemistry* **2022**, *38*, 100688.

[21] P. Tian, Y. Wei, M. Ye, Z. Liu, *ACS Catalysis* **2015**, *5*, 1922-1938.

[22] I. Yarulina, A. D. Chowdhury, F. Meirer, B. M. Weckhuysen, J. Gascon, *Nature Catalysis* **2018**, *1*, 398-411.

[23] N. Badger, R. Boylu, V. Ilojianya, M. Erguvan, S. Amini, *Energy Advances* **2024**, *3*, 2311-2327.

[24] A. Klerke, C. H. Christensen, J. K. Nørskov, T. Vegge, *Journal of Materials Chemistry* **2008**, *18*, 2304-2310.

[25] T. B. S., R. Asapu, *ChemBioEng Reviews* **2024**, *11*, 543-554.

[26] F. Schüth, R. Palkovits, R. Schlögl, D. S. Su, *Energy & Environmental Science* **2012**, *5* 6278-6289.

[27] M. S. Herdem, M. Y. Sinaki, S. Farhad, F. Hamdullahpur, *International Journal of Energy Research* **2019**, *43*, 5076-5105.

[28] A. Y. Khodakov, W. Chu, P. Fongarland, *Chemical Reviews* **2007**, *107*, 1692-1744.

[29] M. Marchese, G. Buffo, M. Santarelli, A. Lanzini, *Journal of CO2 Utilization* **2021**, *46*, 101487.

[30] A. de Klerk, G. Chauhan, C. Halmenschlager, F. Link, N. Montoya Sánchez, B. Gartley, H. E. M. El-Sayed, R. Sehdev, R. Lehoux, *Energy Science & Engineering* **2024**, *12*, 394-409.

[31] F. Schüth, in *Catalytic Hydrogenation for Biomass Valorization* (Ed.: R. Rinaldi), The Royal Society of Chemistry, **2014**, p. 0.

[32] M. Besson, P. Gallezot, C. Pinel, *Chemical Reviews* **2014**, *114*, 1827-1870.

[33] A. Racha, C. Samanta, S. Sreekantan, B. Marimuthu, *Energy & Fuels* **2023**, *37*, 11475-11496.

[34] H.-U. Blaser, C. Malan, B. Pugin, F. Spindler, H. Steiner, M. Studer, *Advanced Synthesis & Catalysis* **2003**, *345*, 103-151.

[35] M. A. Stoffels, F. J. R. Klauck, T. Hamadi, F. Glorius, J. Leker, *Advanced Synthesis & Catalysis* **2020**, *362*, 1258-1274.

[36] J. Wang, Z. Yuan, R. Nie, Z. Hou, X. Zheng, *Industrial & Engineering Chemistry Research* **2010**, *49*, 4664-4669.

[37] A. Mary, N. Kanagathara, A. R. Baby Suganthi, *Materials Today: Proceedings* **2020**, *33*, 4751-4755.

[38] K. T. Møller, T. R. Jensen, E. Akiba, H.-w. Li, *Progress in Natural Science: Materials International* **2017**, *27*, 34-40.

[39] N. B. A. Jr, H. Kasai, W. A. Diño, H. Nakanishi, *Japanese Journal of Applied Physics* **2007**, *46*, 4233.

[40] C. D. Vurdu, *Advances in Condensed Matter Physics* **2018**, *2018*, 4186968.

[41] R. B. Levy, M. Boudart, *Science* **1973**, *181*, 547-549.

[42] L. Bennett, J. Cuthill, A. McAlister, N. Erickson, R. Watson, *Science* **1974**, *184*, 563-565.

[43] R. J. Colton, J.-T. J. Huang, J. W. Rabalais, *Chemical Physics Letters* **1975**, *34*, 337-339.

[44] P. N. Ross, P. Stonehart, *Journal of Catalysis* **1975**, *39*, 298-301.

[45] A.-M. Alexander, J. S. J. Hargreaves, *Chemical Society Reviews* **2010**, *39*, 4388-4401.

[46] U.S. Geological Survey, Mineral commodity summaries 2024, U.S. Geological Survey, Reston, VA, 2024, p. 190. https://pubs.usgs.gov/publication/mcs2024. DOI: 10.3133/mcs2024.

[47] M. Führer, T. van Haasterecht, J. H. Bitter, *Catalysis Science & Technology* **2020**, *10*, 6089-6097.

[48] F. H. Ribeiro, M. Boudart, R. A. Dalla Betta, E. Iglesia, *Journal of Catalysis* **1991**, *130*, 498-513.

[49] S. S. Pansare, W. Torres, J. G. Goodwin, *Catalysis Communications* **2007**, *8*, 649-654.

[50] N. Luo, W. Yang, L. Feng, S. Huang, P. Huang, M. Wei, *Molecular Catalysis* **2024**, *553* 113683.

[51] J. A. Schaidle, L. T. Thompson, *Journal of Catalysis* **2015**, *329*, 325-334.

[52] J. B. Claridge, A. P. E. York, A. J. Brungs, C. Marquez-Alvarez, J. Sloan, S. C. Tsang, M. L. H. Green, *Journal of Catalysis* **1998**, *180*, 85-100.

[53] J. Pang, J. Sun, M. Zheng, H. Li, Y. Wang, T. Zhang, *Applied Catalysis B: Environmental* **2019**, *254*, 510-522.

[54] S. A. W. Hollak, R. W. Gosselink, D. S. van Es, J. H. Bitter, *ACS Catalysis* **2013**, *3*, 2837-2844.

[55] R. W. Gosselink, D. R. Stellwagen, J. H. Bitter, *Angew Chem Int Ed Engl* **2013**, *52*, 5089-5092.

[56] H. Ren, Y. Chen, Y. Huang, W. Deng, D. G. Vlachos, J. G. Chen, *Green Chem.* **2014**, *16*, 761-769.

[57] N. Ji, T. Zhang, M. Zheng, A. Wang, H. Wang, X. Wang, J. G. Chen, *Angew Chem Int Ed Engl* **2008**, *47*, 8510-8513.

[58] Q. Qiang, H. Yang, W. Su, H. He, S. Tian, C. Li, T. Zhang, *Catalysis Today* **2024**, *442*, 114913.

[59] F. Wang, J. Jiang, K. Wang, Q. Zhai, H. Sun, P. Liu, J. Feng, H. Xia, J. Ye, Z. Li, F. Li, J. Xu, *Fuel* **2018**, *228*, 103-111.

[60] R. Ooms, M. Dusselier, J. A. Geboers, B. Op de Beeck, R. Verhaeven, E. Gobechiya, J. A. Martens, A. Redl, B. F. Sels, *Green Chem.* **2014**, *16*, 695-707.

[61] Y. B. Huang, M. Y. Chen, L. Yan, Q. X. Guo, Y. Fu, *ChemSusChem* **2014**, *7*, 1068-1072.

[62] P. Bretzler, M. Huber, S. Nickl, K. Kohler, *RSC Adv* **2020**, *10*, 27323-27330.

[63] S. Meyer, A. V. Nikiforov, I. M. Petrushina, K. Köhler, E. Christensen, J. O. Jensen, N. J. Bjerrum, *International Journal of Hydrogen Energy* **2015**, *40*, 2905-2911.

[64] P. Bretzler, K. Köhler, A. V. Nikiforov, E. Christensen, R. W. Berg, N. J. Bjerrum, *International Journal of Hydrogen Energy* **2020**, *45*, 21262-21272.

[65] P. Bretzler, M. Huber, A. A. Rane, R. E. Jentoft, K. Köhler, F. C. Jentoft, *Journal of Catalysis* **2022**, *405*, 60-73.

[66] F. Garin, *Catalysis Today* **2004**, *89*, 255-268.

[67] M. Wojciechowska, S. Lomnicki, *Clean Products and Processes* **1999**, *1*, 237-247.

[68] S. S. Taha, S. Idoudi, N. Alhamdan, R. H. Ibrahim, R. Surkatti, A. Amhamed, O. F. Alrebei, *Journal of Hazardous Materials Advances* **2025**, *19*, 100771.

[69] K. Skalska, J. S. Miller, S. Ledakowicz, *Science of The Total Environment* **2010**, *408*, 3976-3989.

[70] M. W. Jones, G. P. Peters, T. Gasser, R. M. Andrew, C. Schwingshackl, J. Gütschow, R. A. Houghton, P. Friedlingstein, J. Pongratz, C. Le Quéré, *Scientific Data* **2023**, *10*, 155.

[71] A. R. Ravishankara, J. S. Daniel, R. W. Portmann, *Science* **2009**, *326*, 123-125.

[72] N. Imanaka, T. Masui, *Applied Catalysis A: General* **2012**, *431-432*, 1-8.

[73] M. Konsolakis, *ACS Catalysis* **2015**, *5*, 6397-6421.

[74] F. Gholami, M. Tomas, Z. Gholami, M. Vakili, *Science of The Total Environment* **2020**, *714*, 136712.

[75] M. Börnhorst, O. Deutschmann, *Progress in Energy and Combustion Science* **2021**, *87* 100949.

[76] aK. Kamasamudram, A. Yezerets, X. chen, N. Currier, M. Castagnola, H.-Y. Chen, *SAE International Journal of Engines* **2011**, *4*, 1810-1821; bJ. Nockert, L. Nyborg, M. Norell, *Materials and Corrosion* **2012**, *63*, 388-395.

[77] A. Onorati, R. Payri, B. Vaglieco, A. Agarwal, C. Bae, G. Bruneaux, M. Canakci, M. Gavaises, M. Günthner, C. Hasse, S. Kokjohn, S.-C. Kong, Y. Moriyoshi, R. Novella, A. Pesyridis, R. Reitz, T. Ryan, R. Wagner, H. Zhao, *International Journal of Engine Research* **2022**, *23*, 529-540.

[78] Z. Stępień, *Energies* **2021**, *14*, 6504.

[79] C. Özyalcin, S. Sterlepper, S. Roiser, H. Eichlseder, S. Pischinger, *Applied Energy* **2024**, *353*, 122045.

[80] P. G. Savva, C. N. Costa, *Catalysis Reviews* **2011**, *53*, 91-151.

[81] Z. Hu, R. T. Yang, *Industrial & Engineering Chemistry Research* **2019**, *58*, 10140-10153.

[82] P. Schlachta, R. Jentoft, F. C. Jentoft, K. Köhler, *The Journal of Physical Chemistry C* **2025**, *129*, 20907-20921.

[83] S. T. Oyama, in *The Chemistry of Transition Metal Carbides and Nitrides* (Ed.: S. T. Oyama), Springer Netherlands, Dordrecht, **1996**, p. 2.

[84] H. J. Goldschmidt, in *Interstitial Alloys* (Ed.: H. J. Goldschmidt), Springer US, Boston, MA, **1967**, p. 1.

[85] H. J. Goldschmidt, in *Interstitial Alloys* (Ed.: H. J. Goldschmidt), Springer US, Boston, MA, **1967**, pp. 14-59.

[86] H. J. Goldschmidt, in *Interstitial Alloys* (Ed.: H. J. Goldschmidt), Springer US, Boston, MA, **1967**, pp. 88-213.

[87] S. T. Oyama, *Catalysis Today* **1992**, *15*, 179-200.

[88] D. H. Jack, in *Concise Encyclopedia of Advanced Ceramic Materials* (Ed.: R. J. Brook), Pergamon, Oxford, **1991**, pp. 391-394.

[89] V. Bonache, M. D. Salvador, D. Busquets, P. Burguete, E. Martínez, F. Sapiña, E. Sánchez, *International Journal of Refractory Metals and Hard Materials* **2011**, *29*, 78-84.

[90] L. J. Prakash, *International Journal of Refractory Metals and Hard Materials* **1995**, *13*, 257-264.

[91] A. Shemi, A. Magumise, S. Ndlovu, N. Sacks, *Minerals Engineering* **2018**, *122*, 195-205.

[92] A. Hirata, H. Zheng, M. Yoshikawa, *Diamond and Related Materials* **1998**, *7*, 1669-1674.

[93] K.-M. Tsai, C.-Y. Hsieh, H.-H. Lu, *Ceramics International* **2010**, *36*, 689-692.

[94] I. Konyashin, *International Journal of Refractory Metals and Hard Materials* **2023**, *111*, 106113.

[95] D. V. Suetin, I. R. Shein, A. L. Ivanovskii, *Russian Chemical Reviews* **2010**, *79*, 611-634.

[96] A. S. Kurlov, A. I. Gusev, *Inorganic Materials* **2006**, *42*, 121-127.

[97] D. V. Suetin, I. R. Shein, A. L. Ivanovskii, *Journal of Physics and Chemistry of Solids* **2009**, *70*, 64-71.

[98] N. Luo, Z. Hou, C. Lin, G.-L. Chai, *Crystal Growth & Design* **2023**, *23*, 5486-5497.

[99] A. S. Kurlov, A. I. Gusev, *Physical Review B* **2007**, *76*, 174115.

[100] E. Raekelboom, K. Abdelouahdi, C. Legrand-Buscema, *Thin Solid Films* **2009**, *517*, 1555-1558.

[101] J. Kim, J.-H. Jang, Y.-H. Lee, Y.-U. Kwon, *Journal of Power Sources* **2009**, *193*, 441-446.

[102] H. Moissan, *Compt. rend* **1893**, *116*, 1225-1227.

[103] R. Polini, A. Marcucci, C. D'Ottavi, P. Nunziante, P. De Filippis, G. Marcheselli, *ACS Sustainable Chemistry & Engineering* **2021**, *9*, 8458-8466.

[104] R. Koc, S. K. Kodambaka, *Journal of the European Ceramic Society* **2000**, *20*, 1859-1869.

[105] E. Lassner, W.-D. Schubert, *Tungsten: properties, chemistry, technology of the element, alloys, and chemical compounds*, Springer Science & Business Media, **2012**, p. 115.

[106] G. Mühlbauer, G. Kremser, A. Bock, J. Weidow, W.-D. Schubert, *International Journal of Refractory Metals and Hard Materials* **2018**, *72*, 141-148.

[107] L. V. McCarty, R. Donelson, R. f. Hehemann, *Metallurgical Transactions A* **1991**, *18*, 969-974.

[108] E. Iglesia, F. H. Ribeiro, M. Boudart, J. E. Baumgartner, *Catalysis Today* **1992**, *15*, 307-337.

[109] E. Madadian, Y. Ghaffari, Y. Zilberman, D. S. A. Simakov, *ChemNanoMat* **2025***, 0*, e202500260.

[110] G. Leclercq, M. Kamal, J. M. Giraudon, P. Devassine, L. Feigenbaum, L. Leclercq, A. Frennet, J. M. Bastin, A. Löfberg, S. Decker, *Journal of catalysis* **1996**, *158*, 142-169.

[111] A. E. Newkirk, I. Aliferis, *Journal of the American Chemical Society* **1957**, *79*, 4629-4631.

[112] M. Boudart, S. T. Oyama, L. Volpe, US Patent 4,515,763, **1985**.

[113] S. T. Oyama, J. C. Schlatter, J. E. Metcalfe III, J. M. Lambert Jr, *Industrial & engineering chemistry research* **1988**, *27*, 1639-1648.

[114] J. S. Lee, S. T. Oyama, M. Boudart, *Journal of Catalysis* **1987**, *106*, 125-133.

[115] F. Pan, J. Liu, Z. Du, Q. Zhu, M. Zhang, D. Yan, S. Li, *Industrial & Engineering Chemistry Research* **2021**, *60*, 162-172.

[116] J. Dang, Y. Wu, Z. Lv, X. Lv, *Journal of Alloys and Compounds* **2018**, *745*, 421-429.

[117] V. S. Palanker, D. V. Sokolsky, E. A. Mazulevsky, E. N. Baybatyrov, *Electrochimica Acta* **1977**, *22*, 661-667.

[118] F. Medeiros, S. De Oliveira, C. De Souza, A. Da Silva, U. Gomes, J. De Souza, *Materials Science and Engineering: A* **2001**, *315*, 58-62.

[119] A. Löfberg, A. Frennet, G. Leclercq, L. Leclercq, J. M. Giraudon, *Journal of Catalysis* **2000**, *189*, 170-183.

[120] J. B. Claridge, A. P. E. York, A. J. Brungs, M. L. H. Green, *Chemistry of Materials* **2000** *12*, 132-142.

[121] J. M. Giraudon, P. Devassine, J. F. Lamonier, L. Delannoy, L. Leclercq, G. Leclercq, *Journal of Solid State Chemistry* **2000**, *154*, 412-426.

[122] T. Xiao, A. Hanif, A. P. York, J. Sloan, M. L. Green, *Physical Chemistry Chemical Physics* **2002**, *4*, 3522-3529.

[123] S. Decker, A. Löfberg, J. M. Bastin, A. Frennet, *Catalysis Letters* **1997**, *44*, 229-239.

[124] L. Volpe, M. Boudart, *Journal of solid state chemistry* **1985**, *59*, 332-347.

[125] S. Meyer, H. Beyer, K. Köhler, A. H. Jensen, E. Christensen, N. J. Bjerrum, *Microporous and Mesoporous Materials* **2015**, *211*, 147-151.

[126] L. Volpe, M. Boudart, *Journal of Solid State Chemistry* **1985**, *59*, 348-356.

[127] S.-K. Sun, Y.-M. Kan, G.-J. Zhang, P.-L. Wang, *Journal of the American Ceramic Society* **2010**, *93*, 3565-3568.

[128] S. T. Oyama, in *Handbook of Heterogeneous Catalysis, Vol. 2* (Ed.: H. K. G. Ertl, F. Schüth and J. Weitkamp), **2008**, p. 346.

[129] S. Wanner, L. Hilaire, P. Wehrer, J. Hindermann, G. Maire, *Applied Catalysis A: General* **2000**, *203*, 55-70.

[130] J. M. Giraudon, P. Devassine, L. Leclercq, G. Leclercq, *Journal of Materials Science* **1998**, *33*, 1369-1377.

[131] I. Novoselova, S. Kuleshov, E. Fedoryshena, V. Bykov, *ECS Transactions* **2018**, *86*, 81.

[132] Y. Wang, L. Zhang, X. Xi, Z. Nie, *Ceramics International* **2025**, *51*, 40223-40233.

[133] I. A. Novoselova, S. V. Kuleshov, A. O. Omelchuk, V. N. Bykov, O. M. Fesenko, *Powder Metallurgy and Metal Ceramics* **2023**, *62*, 142-152.

[134] J. Ma, Y. Du, *Journal of Alloys and Compounds* **2008**, *448*, 215-218.

[135] R. F. André, F. D'Accriscio, A. P. Freitas, G. Crochet, C. Bouillet, M. Bahri, O. Ersen, C. Sanchez, S. Carenco, *Green Chemistry* **2021**, *23*, 6431-6448.

[136] L. Delannoy, J. M. Giraudon, P. Granger, L. Leclercq, G. Leclercq, *Catalysis Today* **2000**, *59*, 231-240.

[137] M. M. Sullivan, A. Bhan, *Journal of Catalysis* **2016**, *344*, 53-58.

[138] C. Li, M. Zheng, A. Wang, T. Zhang, *Energy Environ. Sci.* **2012**, *5*, 6383-6390.

[139] G. Singla, M. Mahajan, P. K. Jha, K. Singh, O. P. Pandey, *Applied Physics A* **2024**, *130* 648.

[140] H. Fang, J. Du, C. Tian, J. Zheng, X. Duan, L. Ye, Y. Yuan, *Chem Commun (Camb)* **2017**, *53*, 10295-10298.

[141] H. C. Fu, X. H. Wang, X. H. Chen, Q. Zhang, N. B. Li, H. Q. Luo, *Applied Catalysis B: Environmental* **2022**, *301*, 120818.

[142] B. Yang, C. G. Wei, X. H. Wang, H. C. Fu, X. H. Chen, Q. Zhang, Y. H. Luo, H. Q. Luo, N. B. Li, *Materials Today Nano* **2023**, *23*, 100350.

[143] Q. Gong, Y. Wang, Q. Hu, J. Zhou, R. Feng, P. N. Duchesne, P. Zhang, F. Chen, N. Han, Y. Li, C. Jin, Y. Li, S. T. Lee, *Nat Commun* **2016**, *7*, 13216.

[144] Z. Zhang, R.-H. Xie, X. Liang, F. Zhang, H. Yang, M.-K. Zou, L. Zhang, C. Shi, H.-M. Cheng, L. Zhang, C. Liu, *Nano Letters* **2025**, *25*, 8612-8618.

[145] M. Führer, T. van Haasterecht, J. H. Bitter, *Catalysis Today* **2023**, *418*, 114108.

[146] L. Souza Macedo, V. Teixeira da Silva, J. H. Bitter, *ChemEngineering* **2019**, *3*, 24.

[147] D. R. Stellwagen, J. H. Bitter, *Green Chemistry* **2015**, *17*, 582-593.

[148] M. G. Álvarez, R. J. Chimentão, D. Tichit, J. B. O. Santos, A. Dafinov, L. B. Modesto-López, J. Rosell-Llompart, E. J. Güell, F. Gispert-Guirado, J. Llorca, F. Medina, *Microporous and Mesoporous Materials* **2016**, *219*, 19-28.

[149] L. Hu, S. Ji, Z. Jiang, H. Song, P. Wu, Q. Liu, *The Journal of Physical Chemistry C* **2007** *111*, 15173-15184.

[150] L. Hu, S. Ji, T. Xiao, C. Guo, P. Wu, P. Nie, *The Journal of Physical Chemistry B* **2007** *111*, 3599-3608.

[151] M. Juneau, D. Yaffe, R. Liu, J. N. Agwara, M. D. Porosoff, *Nanoscale* **2022**, *14*, 16458-16466.

[152] Q. Lu, C.-J. Chen, W. Luc, J. G. Chen, A. Bhan, F. Jiao, *ACS Catalysis* **2016**, *6*, 3506-3514.

[153] L. Gao, B. Kear, *Nanostructured materials* **1995**, *5*, 555-569.

[154] P. N. Ross Jr, P. Stonehart, *Journal of catalysis* **1977**, *48*, 42-59.

[155] V. S. Palanker, D. V. Sokolsky, E. A. Mazulevsky, E. N. Baybatyrov, *Journal of Power Sources* **1976**, *1*, 169-176.

[156] D. Migas, V. Shaposhnikov, V. Rodin, V. Borisenko, *Journal of Applied Physics* **2010**, *108*, 093713.

[157] C. J. Howard, V. Luca, K. S. Knight, *Journal of Physics: Condensed Matter* **2001**, *14*, 377.

[158] S. Keilholz, R. Paul, L. Y. Dorsch, H. Kohlmann, *Chemistry* **2023**, *29*, e202203932.

[159] T. R. Wilken, W. R. Morcom, C. A. Wert, J. B. Woodhouse, *Metallurgical Transactions B* **1976**, *7*, 589-597.

[160] C. Ren, Z. Z. Fang, H. Zhang, M. Koopman, *International Journal of Refractory Metals and Hard Materials* **2016**, *61*, 273-278.

[161] M. Ostermann, V. Dalbauer, W.-D. Schubert, R. Haubner, *Tungsten* **2022**, *4*, 60-66.

[162] X.-w. Wu, J.-s. Luo, B.-z. Lu, C.-H. Xie, Z.-M. Pi, M.-Z. Hu, T. Xu, G.-G. Wu, Z.-M. Yu, D.-Q. Yi, *Transactions of Nonferrous Metals Society of China* **2009**, *19*, s785-s789.

[163] K. Chen, A. T. Bell, E. Iglesia, *The Journal of Physical Chemistry B* **2000**, *104*, 1292-1299.

[164] W. Morcom, W. Worrell, H. G. Sell, H. Kaplan, *Metallurgical and Materials Transactions B* **1974**, *5*, 155-161.

[165] M. Charlton, G. Davis, *Nature* **1955**, *175*, 131-132.

[166] A. Rukini, M. A. Rhamdhani, G. A. Brooks, A. Van den Bulck, *Journal of Sustainable Metallurgy* **2022**, *8*, 1-24.

[167] R. Haubner, W. Schubert, E. Lassner, M. Schreiner, B. Lux, *International journal of refractory & hard metals* **1983**, *2*, 108-115.

[168] M. I. Alymov, N. M. Rubtsov, B. S. Seplyarskii, V. A. Zelensky, A. B. Ankudinov, *Mendeleev Communications* **2019**, *29*, 355-357.

[169] A. Jain, S. P. Ong, G. Hautier, W. Chen, W. D. Richards, S. Dacek, S. Cholia, D. Gunter, D. Skinner, G. Ceder, K. A. Persson, *APL Materials* **2013**, *1*, 011002.

[170] S. Chen, J. Wang, R. Wu, Z. Wang, Y. Li, Y. Lu, W. Zhou, P. Hu, H. Li, *Journal of Materials Science & Technology* **2021**, *90*, 66-75.

[171] J. M. McHale, A. Auroux, A. J. Perrotta, A. Navrotsky, *Science* **1997**, *277*, 788-791.

[172] F. Ribeiro, R. Dalla Betta, G. Guskey, M. Boudart, *Chemistry of Materials* **1991**, *3*, 805-812.

[173] K. Schmid, J. Roth, *Journal of Nuclear Materials* **2002**, *302*, 96-103.

[174] A. Navrotsky, *Geochemical Transactions* **2003**, *4*, 34.

[175] A. Shrestha, X. Gao, J. C. Hicks, C. Paolucci, *Chemistry of Materials* **2021**, *33*, 4606-4620.

[176] M. P. Finnegan, H. Zhang, J. F. Banfield, *The Journal of Physical Chemistry C* **2007**, *111*, 1962-1968.

[177] J. Banfield, *Journal of Materials Chemistry* **1998**, *8*, 2073-2076.

[178] J. M. McHale, A. Navrotsky, A. J. Perrotta, *The Journal of Physical Chemistry B* **1997**, *101*, 603-613.

[179] M. K. Neylon, S. Choi, H. Kwon, K. E. Curry, L. T. Thompson, *Applied Catalysis A: General* **1999**, *183*, 253-263.

[180] H. Fang, A. Roldan, C. Tian, Y. Zheng, X. Duan, K. Chen, L. Ye, S. Leoni, Y. Yuan, *Journal of Catalysis* **2019**, *369*, 283-295.

[181] L.-N. Zhang, Y.-Y. Ma, Z.-L. Lang, Y.-H. Wang, S. U. Khan, G. Yan, H.-Q. Tan, H.-Y. Zang, Y.-g. Li, *Journal of Materials Chemistry A* **2018**, *6*, 15395-15403.

[182] D. V. Esposito, S. T. Hunt, Y. C. Kimmel, J. G. Chen, *J Am Chem Soc* **2012**, *134*, 3025-3033.

[183] F. Bannert, P. Schlachta, N. Shilpa, E. Christensen, R. W. Berg, K. Köhler, N. J. Bjerrum, *Journal of The Electrochemical Society* **2025**, *172*, 074506.

[184] X. Li, G. Zhang, F. Cheng, B. Guo, J. Chen, *Journal of The Electrochemical Society* **2006**, *153*, H133.

[185] A. K. Dutta, T. Ho, L. Zhang, P. Stroeve, *Chemistry of Materials* **2000**, *12*, 3236-3236.

[186] M. Daniel, B. Desbat, J. Lassegues, B. Gerand, M. Figlarz, *Journal of solid state chemistry* **1987**, *67*, 235-247.

[187] C. I. Vargas-Consuelos, K. Seo, M. Camacho-López, O. A. Graeve, *The Journal of Physical Chemistry C* **2014**, *118*, 9531-9537.

[188] G. Escalante, R. López, F. N. Demesa, G. Villa-Sánchez, V. H. Castrejón-Sánchez, I. Vivaldo de la Cruz, *AIP Advances* **2021**, *11*, 055103.

[189] D. C. Vermaire, P. C. van Berge, *Journal of catalysis* **1989**, *116*, 309-317.

[190] E. Ogata, Y. Kamiya, N. Ohta, *Journal of Catalysis* **1973**, *29*, 296-307.

[191] V. Brazhkin, *Journal of Physics: Condensed Matter* **2006**, *18*, 9643.

[192] A. Mehdad, R. E. Jentoft, F. C. Jentoft, *Journal of Catalysis* **2017**, *351*, 161-173.

[193] A. Mehdad, R. E. Jentoft, F. C. Jentoft, *Catalysis Today* **2019**, *323*, 112-122.

[194] L. Brewer, *Science* **1968**, *161*, 115-122.

[195] W. Hume-Rothery, *Progress in Materials Science* **1968**, *13*, 229-265.

[196] J. G. Chen, *Chemical reviews* **1996**, *96*, 1477-1498.

[197] A. I. Gusev, A. A. Rempel, A. J. Magerl, *Disorder and order in strongly nonstoichiometric compounds: transition metal carbides, nitrides and oxides, Vol. 47*, Springer Science & Business Media, **2013**, p. 43.

[198] A. Kurlov, A. Gusev, *Journal of Experimental and Theoretical Physics* **2007**, *105*, 710-721.

[199] E. A. Davidson, D. Kanter, *Environmental Research Letters* **2014**, *9*, 105012.

[200] R. Feng, Z. Li, *Environmental Pollution* **2023**, *338*, 122664.

[201] J. Pérez-Ramírez, F. Kapteijn, K. Schöffel, J. A. Moulijn, *Applied Catalysis B: Environmental* **2003**, *44*, 117-151.

[202] A. Shimizu, K. Tanaka, M. Fujimori, *Chemosphere - Global Change Science* **2000**, *2*, 425-434.

[203] S. He, Y. Han, X. Qin, *Journal of Environmental Sciences* **2025**, *157*, 615-632.

[204] F. Y. Al-Aboosi, M. M. El-Halwagi, M. Moore, R. B. Nielsen, *Current Opinion in Chemical Engineering* **2021**, *31*, 100670.

[205] S. Esquivel-Elizondo, B. Walkowiak, S. S. Sartzetakis, B. Buma, *Environmental Science & Technology* **2025**, *59*, 9037-9048.

[206] W. Ramsay, E. Fridell, M. Michan, *Journal of Marine Science and Application* **2023**, *22* 681-692.

[207] S. Roy, M. S. Hegde, S. Sharma, N. P. Lalla, A. Marimuthu, G. Madras, *Applied Catalysis B: Environmental* **2008**, *84*, 341-350.

[208] S. A. Carabineiro, B. E. Nieuwenhuys, *Surface Science* **2001**, *495*, 1-7.

[209] R. Burch, S. T. Daniells, J. P. Breen, P. Hu, *Catalysis Letters* **2004**, *94*, 103-108.

[210] J. Meyer, K. Reuter, *Angewandte Chemie International Edition* **2014**, *53*, 4721-4724.

[211] A. Groß, *Applied Surface Science Advances* **2022**, *9*, 100240.

[212] S. P. Rittmeyer, B. V. J., K. and Reuter, *Advances in Physics: X* **2018**, *3*, 1381574.

[213] W. M. Pearlman, *Tetrahedron Letters* **1967**, *8*, 1663-1664.

[214] C. Gnad, O. Dachwald, G. Raudaschl-Sieber, K. Köhler, *Journal of Catalysis* **2019**, *375*, 257-266.

[215] C. Haeßner, B. Müller, O. Storcheva, K. Köhler, *ChemCatChem* **2013**, *5*, 3260-3268.

[216] X. Zhang, J. Zheng, F. J. Boch, S. Nickl, K. Köhler, *ChemCatChem* **2024**, *16*, e202400347.

[217] G. Tuci, Y. Liu, A. Rossin, X. Guo, C. Pham, G. Giambastiani, C. Pham-Huu, *Chemical Reviews* **2021**, *121*, 10559-10665.

[218] M. C. Santos, R. T. S. Oliveira, E. C. Pereira, L. O. S. Bulhões, *Thin Solid Films* **2005**, *483*, 164-168.

[219] C. Amorim, M. A. Keane, *Journal of Colloid and Interface Science* **2008**, *322*, 196-208.

[220] J. Sá, G. D. Arteaga, R. A. Daley, J. Bernardi, J. A. Anderson, *The Journal of Physical Chemistry B* **2006**, *110*, 17090-17095.

[221] R. Prins, *Chemical Reviews* **2012**, *112*, 2714-2738.

[222] F. Drault, C. Comminges, F. Can, L. Pirault-Roy, F. Epron, A. Le Valant, *Materials* **2018**, *11*, 819.

[223] M. Montes, C. P. De Bosscheyde, B. Hodnett, F. Delannay, P. Grange, B. Delmon, *Applied catalysis* **1984**, *12*, 309-330.

[224] P. Burattin, M. Che, C. Louis, *The Journal of Physical Chemistry B* **1997**, *101*, 7060-7074.

[225] B. A. T. Mehrabadi, S. Eskandari, U. Khan, R. D. White, J. R. Regalbuto, **2017**, pp. 1-35.

[226] M.-F. Luo, Z.-Y. Hou, X.-X. Yuan, X.-M. Zheng, *Catalysis Letters* **1998**, *50*, 205-209.

[227] W.-J. Shen, Y. Ichihashi, H. Ando, Y. Matsumura, M. Okumura, M. Haruta, *Applied Catalysis A: General* **2001**, *217*, 231-239.

[228] P. Sangeetha, K. Shanthi, K. S. R. Rao, B. Viswanathan, P. Selvam, *Applied Catalysis A: General* **2009**, *353*, 160-165.

[229] A. Aznárez, A. Gil, S. Korili, *RSC Advances* **2015**, *5*, 82296-82309.

[230] K. Ebitani, H. Konno, T. Tanaka, H. Hattori, *Journal of Catalysis* **1992**, *135*, 60-67.

[231] C.-P. Hwang, C.-T. Yeh, Q. Zhu, *Catalysis Today* **1999**, *51*, 93-101.

[232] H. C. Yao, S. Japar, M. Shelef, *Journal of Catalysis* **1977**, *50*, 407-418.

[233] J. Panpranot, O. Tangjitwattakorn, P. Praserthdam, J. G. Goodwin Jr, *Applied Catalysis A: General* **2005**, *292*, 322-327.

[234] C. A. Klug, S. Kroeker, P. M. Aguiar, M. Zhou, D. F. Stec, I. E. Wachs, *Chemistry of Materials* **2009**, *21*, 4127-4134.

[235] S. Parres-Esclapez, F. E. López-Suárez, A. Bueno-López, M. J. Illán-Gómez, B. Ura, J. Trawczynski, *Topics in Catalysis* **2009**, *52*, 1832.

[236] W. Martienssen, in *Springer Handbook of Materials Data* (Eds.: H. Warlimont, W. Martienssen), Springer International Publishing, Cham, **2018**, pp. 41-43.

[237] H. Warlimont, in *Springer Handbook of Materials Data* (Eds.: H. Warlimont, W. Martienssen), Springer International Publishing, Cham, **2018**, pp. 445-488.

[238] H. Beyer, K. Köhler, *Applied Catalysis B: Environmental* **2010**, *96*, 110-116.

[239] H. Gysling, J. Monnier, G. Apai, *Journal of Catalysis* **1987**, *103*, 407-418.

[240] M. Y. Smirnov, A. V. Kalinkin, V. I. Bukhtiyarov, *Kinetics and Catalysis* **2019**, *60*, 823-831.

[241] J. F. Moulder, J. Chastain, *Handbook of X-ray Photoelectron Spectroscopy: A Reference Book of Standard Spectra for Identification and Interpretation of XPS Data*, Physical Electronics Division, Perkin-Elmer Corporation, **1992**, p. 116.

[242] J. B. F. Anderson, R. Burch, J. A. Cairns, *Applied Catalysis* **1986**, *25*, 173-180.

[243] S. Parres-Esclapez, I. Such-Basañez, M. J. Illán-Gómez, C. Salinas-Martínez de Lecea, A. Bueno-López, *Journal of Catalysis* **2010**, *276*, 390-401.

[244] H. Beyer, J. Emmerich, K. Chatziapostolou, K. Köhler, *Applied Catalysis A: General* **2011**, *391*, 411-416.

[245] E. R. S. Winter, *Journal of Catalysis* **1969**, *15*, 144-152.

[246] E. R. S. Winter, *Journal of Catalysis* **1970**, *19*, 32-40.

[247] E. R. S. Winter, *Journal of Catalysis* **1974**, *34*, 431-439.

[248] E. R. S. Winter, *Journal of Catalysis* **1974**, *34*, 440-444.

[249] C. M. Fu, V. N. Korchak, W. K. Hall, *Journal of Catalysis* **1981**, *68*, 166-171.

[250] J. Leglise, J. O. Petunchi, W. K. Hall, *Journal of Catalysis* **1984**, *86*, 392-399.

[251] G. Pekridis, C. Athanasiou, M. Konsolakis, I. V. Yentekakis, G. E. Marnellos, *Topics in Catalysis* **2009**, *52*, 1880.

[252] N. Richards, J. H. Carter, E. Nowicka, L. A. Parker, S. Pattisson, Q. He, N. F. Dummer, S. Golunski, G. J. Hutchings, *Applied Catalysis B: Environmental* **2020**, *264*, 118501.

[253] S. Haq, A. Hodgson, *Surface science* **2000**, *463*, 1-10.

[254] Y. Kim, J. A. Schreifels, J. M. White, *Surface Science* **1982**, *114*, 349-361.

[255] A. Spitzer, H. Lüth, *Physical Review B* **1984**, *30*, 3098-3102.

[256] A. V. Zeigarnik, *Kinetics and Catalysis* **2003**, *44*, 233-246.

[257] V. K. Tzitzios, V. Georgakilas, *Chemosphere* **2005**, *59*, 887-891.

[258] R. W. McCabe, C. Wong, *Journal of Catalysis* **1990**, *121*, 422-431.

[259] A. C. Gluhoi, M. A. P. Dekkers, B. E. Nieuwenhuys, *Journal of Catalysis* **2003**, *219*, 197-205.

[260] H. Horino, S. Liu, M. Sano, S. Wako, A. Hiratsuka, Y. Ohno, I. Kobal, T. Matsushima, *Topics in Catalysis* **2002**, *18*, 21-26.

[261] C.-T. Au, M. W. Roberts, *Journal of the Chemical Society, Faraday Transactions 1: Physical Chemistry in Condensed Phases* **1987**, *83*, 2047-2059.

[262] H. Brune, J. Wintterlin, R. Behm, G. Ertl, *Physical review letters* **1992**, *68*, 624.

[263] J. Wintterlin, R. Schuster, G. Ertl, *Physical review letters* **1996**, *77*, 123.

[264] T. Nobukawa, M. Yoshida, S. Kameoka, S.-i. Ito, K. Tomishige, K. Kunimori, *Catalysis Today* **2004**, *93-95*, 791-796.

[265] D. Borodin, M. Schwarzer, H. W. Hahn, J. Fingerhut, Y. Wang, D. J. Auerbach, H. Guo, J. Schroeder, T. N. Kitsopoulos, A. M. Wodtke, *Molecular Physics* **2021**, *119*, e1966533.

[266] S. Völkening, K. Bedürftig, K. Jacobi, J. Wintterlin, G. Ertl, *Physical Review Letters* **1999**, *83*, 2672-2675.

[267] K. Bedürftig, S. Völkening, Y. Wang, J. Wintterlin, K. Jacobi, G. Ertl, *The Journal of Chemical Physics* **1999**, *111*, 11147-11154.

[268] G. B. Fisher, J. L. Gland, S. J. Schmieg, *Journal of Vacuum Science and Technology* **1982**, *20*, 518-521.

[269] I. V. Yentekakis, R. M. Lambert, M. Konsolakis, N. Kallithrakas-Kontos, *Catalysis Letters* **2002**, *81*, 181-185.

[270] K. Yuzaki, T. Yarimizu, K. Aoyagi, S.-i. Ito, K. Kunimori, *Catalysis today* **1998**, *45*, 129-134.

[271] K. Asano, C. Ohnishi, S. Iwamoto, Y. Shioya, M. Inoue, *Applied Catalysis B: Environmental* **2008**, *78*, 242-249.

[272] E. Papista, E. Pachatouridou, M. A. Goula, G. E. Marnellos, E. Iliopoulou, M. Konsolakis, I. V. Yentekakis, *Topics in Catalysis* **2016**, *59*, 1020-1027.

[273] M. Konsolakis, F. Aligizou, G. Goula, I. V. Yentekakis, *Chemical Engineering Journal* **2013**, *230*, 286-295.

[274] J. Haber, M. Nattich, T. Machej, *Applied Catalysis B: Environmental* **2008**, *77*, 278-283.

[275] C. Ohnishi, K. Asano, S. Iwamoto, K. Chikama, M. Inoue, *Catalysis Today* **2007**, *120*, 145-150.

[276] L. Xue, C. Zhang, H. He, Y. Teraoka, *Catalysis Today* **2007**, *126*, 449-455.

[277] B. Bozorgi, J. Karimi-Sabet, P. Khadiv-Parsi, *Environmental Technology & Innovation* **2022**, *26*, 102344.

[278] G. Pekridis, N. Kaklidis, M. Konsolakis, E. F. Iliopoulou, I. V. Yentekakis, G. E. Marnellos, *Topics in Catalysis* **2011**, *54*, 1135.

[279] G. Pekridis, N. Kaklidis, M. Konsolakis, C. Athanasiou, I. V. Yentekakis, G. E. Marnellos, *Solid State Ionics* **2011**, *192*, 653-658.

[280] W. B. Tolman, *Angewandte Chemie International Edition* **2010**, *49*, 1018-1024.

[281] D.-B. Kang, *Bulletin of the Korean Chemical Society* **2007**, *28*, 2369-2376.

[282] A. Kokalj, I. Kobal, T. Matsushima, *The Journal of Physical Chemistry B* **2003**, *107*, 2741-2747.

[283] D. A. Hoffman, J. B. Hudson, *Surface Science* **1987**, *180*, 77-88.

[284] N. Doebelin, R. Kleeberg, *Journal of Applied Crystallography* **2015**, *48*, 1573-1580.

8

Appendix

8.1 List of publications

Publications directly associated with this dissertation

[1] Patrick Schlachta, Rolf E. Jentoft, Friederike C. Jentoft, Klaus Köhler, "Synthesis of Phase-Pure W_2C and WC by Separation of Reduction and Carburization and their Differing Performance as Hydrogenation Catalysts", *The Journal of Physical Chemistry C*, **2025,** *129***,** 20907-20921.

[2] Patrick Schlachta, Rolf E. Jentoft, Elena Willinger, Friederike C. Jentoft, Klaus Köhler, "The decisive role of the dispersion on the phase composition (W_2C and WC) of supported tungsten carbides as hydrogenation catalysts", **in preparation**

[3] Patrick Schlachta, Simon Nickl, Tim Kratky, Elena Willinger, Mark G. Willinger, Sebastian Günther, Klaus Köhler, "Structure-Activity Relationships of Palladium Catalysts in the low Temperature Reduction of N_2O by H_2", **in preparation**

Other publications

[4] Franz Bannert=, Patrick Schlachta=, Nagaraju Shilpa, Erik Christensen, Rolf W. Berg, Klaus Köhler, Niels J. Bjerrum, "Transition Metal Carbide Electrocatalysts (WC, W_2C, and Mo_2C) Compared to Platinum in a Solid Acid Electrolysis Cell", *Journal of The Electrochemical Society* **2025**, *172*, 074506. DOI: 10.1149/1945-7111/ade934

[5] Jinjin Tie, Patrick Schlachta, Chengrui Cui, Klaus Köhler, Erik Christensen, Niels J. Bjerrum, "Tungsten Carbides (W_2C, WC) as Electrocatalysts for Hydrogen Evolution Reactions at 200-230°C in Molten Phosphoric Acid", *Journal of Power Source*, **in peer review**.

[6] Jinjin Tie=, Chengrui Cui=, Patrick Schlachta, Klaus Köhler, Erik Christensen, Niels J. Bjerrum, "CO_2 Reduction Reaction in a Molten Phosphate Electrolyte at 280 °C", **in preparation**.

[7] Bikash Kumar Shaw, Lucia Corti, Joshua M. Tuffnell, Celia Castillo-Blas, Patrick Schlachta, Georgina P. Robertson, Lauren McHugh, Adam F. Sapnik, Sebastian A. Hallweger, Philip A. Chater, Gregor Kieslich, David A. Keen, Sian E. Dutton, Frédéric Blanc, Thomas D. Bennett, "$(RPh_3P)[Mn(dca)_3]$: A Family of Glass-Forming Hybrid Organic–Inorganic Materials", *Inorganic Chemistry* **2024**, *63*, 24812-24824. DOI: 10.1021/acs.inorgchem.4c04181

[8] Shruti Kirti, Patrick Schlachta, Sebastian Hallweger, Gregor Kieslich, Christoph Hartmann, Bikash Kumar Shaw, "Aerobic Melting and Glass Formation in 1-D $(PrPh_3P)_2[M(dca)_4]$ Hybrid Materials", Journal of Materials Chemistry A, **in peer review**.

[9] Heike Plendl, Patrick Schlachta, Tim Kratky, Kristína Krahulíková, Kai-Olaf Hinrichsen, Synthesis, "Synthesis, characterization and activity of CeO_2-doped coprecipitated NiAlOx catalysts for CO_2 methanation", *Applied Catalysis A* **2026,** *711***,** 120728**.**

= Equal Contribution

8.2 Conference contributions

- Increasing the Selectivity for Ring-Opening of Furfurylalcohol over Noble-Metal Free Tungsten Carbide Catalysts
  Patrick Schlachta, Klaus Köhler
  - 55. Jahrestreffen Deutscher Katalytiker, Weimar, Germany, 27 – 29 June 2022, Poster

- Below Room Temperature Catalytic Reduction of N_2O by H_2
  Patrick Schlachta, Simon Nickl, Max Hiller, Tim Kratky, Sebastian Günther, Klaus Köhler
  - 57. Jahrestreffen Deutscher Katalytiker, Weimar, Germany, 13 – 15 March 2024, Poster and Poster Workshop Presentation